

**MASTER THESIS**

**Cyclic axial behaviour of piles in sand:  
3D FE modelling using SANISAND-MS.**

By: *Wenjuan Hu*

Student number: 4665872

June 29, 2021



# **Cyclic axial behaviour of piles in sand: 3D FE modelling using SANISAND-MS.**

By: **Wenjuan Hu**

Student number: 4665872

in partial fulfilment of the requirements for the degree of  
**Master of Science**  
in Civil Engineering  
at the Delft University of Technology

*to be defended publicly on Tuesday June 29, 2021 at 11:00 AM.*

## **Thesis committee:**

Dr. F. (Federico) Pisanò,	TU Delft, Chairman
Prof. Dr. K. G. (Kenneth) Gavin,	TU Delft, Committee Member
Dr. A. (Amin) Askarinejad,	TU Delft, Committee Member
Dr. H. (Haoyuan) Liu,	Norwegian Geotechnical Institute, Supervisor



# Acknowledgements

This master thesis combines various research results from many people and institutions, to whom I express my sincere gratitude. I want to convey my gratitude to my chair supervisor Dr. Federico Pisanò, for introducing me to this interesting geotechnical thesis topic and for all the academic guidance, constant thorough supervising, and moral support that he has offered me so kindly throughout. It is so grateful that the thesis obtained approval from all the committee members involved. I am very thankful to my daily supervisor Dr. Haoyuan Liu, who has been continuously helping me with the thesis using his knowledge and experience, giving me instant feedbacks and patient guidance during and after every contact.

I am proud of being a student at Delft University of Technology (TU Delft), which has gained a reputation worldwide for its powerful academic contributions. During my three years stay in TU Delft, I studied in a multi-cultural environment that I had never experienced before. I am here to appreciate the school deeply, not only for the tremendous assistance in the academic field but also for thorough practical supports to me as an international student.

My family has always been supportive of my decision to study abroad and has always stood by my side. Thank my classmates and friends for their generous assistance during the thesis. Finally, I would like to congratulate myself for having the courage to choose such a challenging school and for never give up whenever a tough time comes during the whole master life.

Wenjuan Hu  
Delft, June 2021

# Abstract

Wind energy is now a popular competitor among other energy sources all around the world. The offshore wind industry has progressed in recent years, with larger wind turbines being installed in deeper oceans. The construction of such large-scale wind farms necessitates more modern foundation design technologies to increase operational safety while also lowering total structure set-up costs.

The environmental load applied to offshore piles are of great complexity. Currents, wind, waves, and even earthquakes are very common dynamic loads in an offshore loading environment. Of course, when a wind turbine is working normally, it also has significant operation loads. The design of offshore wind turbine support structures often involves some universal criteria, e.g., the pull-out capacity of jacket structures on piles. Wind turbine foundation capacity is determined by the qualities of the offshore soil as well as the properties of support structure configurations. Therefore, it is necessary to take account of the potential cyclic impacts of soil-structural interaction to guarantee dependable responses of the wind turbine structure.

This thesis aims at evaluating soil–structure interaction of offshore wind turbine foundations under cyclic loading, with emphasis on the tension capacity of axially loaded displacement piles, under different load conditions (cyclic-to-average ratios) on Fontainebleau NE34 sand in France. A newly developed constitutive soil model SANISAND-MS (2018) is applied to model sand stress-strain evolution. In this thesis, the soil is assumed a homogeneous linear elastoplastic material for the sake of simplicity. The SANISAND-MS constitutive model used in this thesis can capture sand ratcheting after considerable cyclic loading cycles. Furthermore, drained and undrained compression triaxial tests performed at DTU GEO–Lab were used to calibrate the model parameters of the constitutive model for Fontainebleau NE34 sand.

The finite element model adopted here is built in an open-sourced platform, the OpenSees. The Small-strain approach is adopted in the finite element modelling part. The pile is simplified as a wished-in place which does not include the installation effect and the time effect after the installation and before cyclic tests.

Finally, the modelling results are compared to the experiment results recorded by Tsuha et al. (2012). Clear stable, metastable, and unstable response types are recognized in the model results. However, the initial stress state of the sand at the soil-pile interface differs a lot compared to the experiment results. This is the consequence of not including the pile installation effects in the finite element modelling. Recommendations are given to use large-strain soil modelling techniques to include the pile installation process.

# List of Figures

<b>Figure 1-1:</b> Annual wind installations plan by 2050, volume in 2022-2024 and 2026-2029 are estimates. (World Energy Outlook, 2020).....	3
<b>Figure 1-2:</b> New installations of Offshore wind (GWEC Market Intelligence, March 2020).....	4
<b>Figure 1-3:</b> Total offshore wind installations by 2019 (Global Wind Energy Council, 2020).....	4
<b>Figure 1-4:</b> Typical foundation for bottom-mounted OWTs (modified after Kaynia, 2018).....	5
<b>Figure 1-5:</b> Global usage of installation capacity of offshore foundations (Walter Musial et al., 2020).....	5
<b>Figure 1-6:</b> Cyclic load transferred to OWT monopile and jacket foundations (Bhattacharya S et al., 2017). .....	6
<b>Figure 2-1:</b> Example of a 3-legged jacket structure on suction caissons (Jalbi S. et al., 2019). .....	9
<b>Figure 2-2:</b> Example of a 4-legged jacket structure on piles (Cheng-Yu Ku and Lien-Kwei Chien, 2016). .....	10
<b>Figure 2-3:</b> Sway-bending vibration mode of pile supported wind turbines (Bhattacharya S. et al., 2017). .....	11
<b>Figure 2-4:</b> Rocking vibration mode of caisson supported wind turbines (Bhattacharya S. et al., 2017). .....	11
<b>Figure 2-5:</b> Finite Element Model output of vibration modes; (a) Rocking mode for low $k_v$ values; (b) Sway-bending mode for high $k_v$ values (Jalbi S. et al., 2019). .....	12
<b>Figure 2-6:</b> Influence of aspect ratio on the system's vibration mode (Jalbi S. et al., 2019).....	13
<b>Figure 2-7:</b> Types of cyclic loading (Randolph and Gouvernec, 2011).....	14
<b>Figure 2-8:</b> Load-displacement curve from monotonic and cyclic model tests (Dyvik et al. 1989).....	14
<b>Figure 2-9:</b> Factors influence the sand cyclic behaviour: (a) density and mean pressure; (b) number of cycles; (c) stress amplitude; (d) average mean pressure. (Wichtmann T. et al., 2005).....	16
<b>Figure 2-10:</b> Stress paths in $e$ - $\ln p$ space for a state denser than critical (point a) and looser than critical (point b) (Manzari. 1997).....	18
<b>Figure 2-11:</b> Comparison of drained results by SANISANDo4 (left) and SANISAND-MS (right) (Liu, H. Y., 2020). .....	19
<b>Figure 2-12:</b> Comparison of undrained results by SANISANDo4 and SANISAND-MS (Liu et al., 2019). .....	20
<b>Figure 2-13:</b> Relevant surfaces in SANISAND-MS model (Liu et al., 2019). .....	20
<b>Figure 2-14:</b> Evolution of MS & YS in SANISAND-MS model (Liu et al., 2019). .....	21
<b>Figure 2-15:</b> Cyclic loading definitions (Tsuha et al. 2012). .....	22
<b>Figure 2-16:</b> Interaction diagram with different cyclic-to-average ratios and response types obtained from Mini-ICP tests (Tsuha et al. 2012). .....	22
<b>Figure 2-17:</b> Cumulative displacement from stable cycling (Tsuha et al. 2012).....	23
<b>Figure 2-18:</b> Effective stress path from stable cycling (Rimoy et al., 2012). .....	23
<b>Figure 2-19:</b> Tensile capacity gains in stable zone (Tsuha et al. 2012), $Q_T$ -static tension capacity. ....	23
<b>Figure 2-20:</b> Cumulative displacement from metastable cycling (Tsuha et al. 2012). .....	24
<b>Figure 2-22:</b> Cumulative displacement from unstable cycling (Tsuha et al. 2012).....	24

<b>Figure 2-23:</b> Effective stress path from unstable cycling (Rimoy et al., 2012).....	25
<b>Figure 2-24:</b> Pile capacity comparison with/without installation process. (N. Phuong et al. 2019). ..	26
<b>Figure 2-25:</b> Radial stress after 10D penetration from simulation (N. Phuong et al. 2019). .....	27
<b>Figure 2-26:</b> Density change after 10D penetration. MPM model results for a) medium dense sand (void ratio=0.68) and loose sand (void ratio=0.75) (N. Phuong et al. 2019). .....	27
<b>Figure 3-1:</b> The yield, memory, and bounding surface in normalized $\pi$ plane (Liu et al., 2019).....	31
<b>Figure 3-2:</b> Distance definition for dilatancy coefficient (Liu et al., 2019). .....	32
<b>Figure 3-3:</b> Evolution of the yield surface and the memory surface (Liu et al., 2019). .....	34
<b>Figure 3-4:</b> Gradation curve of Fontainebleau NE34 sand. ....	35
<b>Figure 3-5:</b> Calibration results of loose Fontainebleau sand against monotonic drained triaxial test, initial void ratio $e_i=0.702-0.718$ . .....	36
<b>Figure 3-6:</b> Calibration results of medium dense Fontainebleau sand against monotonic drained triaxial test, initial void ratio $e_i=0.637-0.638$ . .....	37
<b>Figure 3-7:</b> Calibration results of dense Fontainebleau sand against monotonic drained triaxial test, initial void ratio $e_i=0.573-0.579$ . .....	37
<b>Figure 3-8:</b> Model performances of loose Fontainebleau sand under symmetric undrained loading (TCS1), $q_{cyc} = 72kPa$ .....	39
<b>Figure 3-9:</b> Model performances of loose Fontainebleau sand under symmetric undrained loading (TCS2), $q_{cyc} = 48kPa$ .....	40
<b>Figure 3-10:</b> Model performances of loose Fontainebleau sand under symmetric undrained loading (TCS3), $q_{cyc} = 35kPa$ . .....	40
<b>Figure 3-11:</b> Model performances of medium dense Fontainebleau sand under symmetric undrained loading (TCS4), $q_{cyc} = 100kPa$ . .....	41
<b>Figure 3-12:</b> Model performances of medium dense Fontainebleau sand under symmetric undrained loading (TCS5), $q_{cyc} = 50kPa$ . .....	41
<b>Figure 3-13:</b> Model performances of medium dense Fontainebleau sand under symmetric undrained loading (TCS6), $q_{cyc} = 40kPa$ . .....	42
<b>Figure 3-14:</b> Model performances of loose Fontainebleau sand under various cyclic stress ratio $\eta^{amp}$ . Test conditions: $e_{in}=0.72$ , $p_c'=200kPa$ .....	43
<b>Figure 3-15:</b> Model performances of medium dense Fontainebleau sand under various cyclic stress ratio $\eta^{amp}$ . Test conditions: $e_{in}=0.64$ , $p_c'=200kPa$ . .....	43
<b>Figure 3-16:</b> Model performances of loose Fontainebleau sand under asymmetric undrained loading (TCA1), $q_c = 200kPa$ , $q_{cyc} = 50kPa$ . .....	44
<b>Figure 3-17:</b> Model performances of medium dense Fontainebleau sand under asymmetric undrained loading (TCA3), $q_c = 200kPa$ , $q_{cyc} = 80kPa$ . .....	44
<b>Figure 4-1:</b> General layout of the sand chamber used in Mini-ICP tests (Tsuha et al. 2012). .....	45
<b>Figure 4-2:</b> Typical Mini-ICP setting (Tsuha et al. 2012). .....	46
<b>Figure 4-3:</b> Geometrical settings of the Finite Element model. ....	47
<b>Figure 4-4:</b> Displacement increments after unstable cyclic loading. ....	48
<b>Figure 4-5:</b> Strain magnitude after unstable cyclic loading.....	48
<b>Figure 4-6:</b> Relative density $D_r$ after unstable cyclic loading. ....	48
<b>Figure 4-7:</b> Dense1 Meshing scheme .....	50
<b>Figure 4-8:</b> Dense2 Meshing scheme .....	50
<b>Figure 4-9:</b> Medium Meshing scheme.....	50
<b>Figure 4-10:</b> Loose Meshing scheme.....	50

<b>Figure 4-11:</b> Accumulated displacement curves of 4 meshing schemes. ....	51
<b>Figure 5-1:</b> Load-displacement curves of exemplar stable tests in the experiment (Tsuha et al. 2012)	54
<b>Figure 5-2:</b> Cumulative displacement curves of exemplar stable tests in the experiment (Tsuha et al. 2012) .....	54
<b>Figure 5-3:</b> Stress paths of exemplar stable tests in the experiment: a) ICP2-OW1, b) ICP4-OW1. (Tsuha et al. 2012).....	54
<b>Figure 5-4:</b> Model results for stable test ICP2-OW1.....	55
<b>Figure 5-5:</b> Model results for stable test ICP4-OW1.....	55
<b>Figure 5-6:</b> Load-displacement curves of exemplar metastable tests in the experiment: a) ICP2-OW3, b) ICP4-TW1 (Tsuha et al. 2012).....	56
<b>Figure 5-7:</b> Cumulative displacement curves of exemplar metastable tests in the experiment (Tsuha et al. 2012). ....	56
<b>Figure 5-8:</b> Stress paths of exemplar metastable tests in the experiment: a) ICP2-OW3, b) ICP4-TW1. (Tsuha et al. 2012).....	56
<b>Figure 5-9:</b> Model results for metastable tests ICP2-OW3. ....	57
<b>Figure 5-10:</b> Model results for metastable tests ICP4-TW1. ....	57
<b>Figure 5-11:</b> Load-displacement (left) and Cumulative displacement (right) curves of exemplar unstable tests in the experiment: b) ICP3-OW1, c) ICP3-TW2. (Tsuha et al. 2012).....	58
<b>Figure 5-12:</b> Stress paths of exemplar unstable tests in the experiment: b) ICP3-OW1, c) ICP3-TW2. (Tsuha et al. 2012).....	58
<b>Figure 5-13:</b> Model results for unstable tests ICP3-OW1. ....	59
<b>Figure 5-14:</b> Model results for unstable tests ICP3-TW2. ....	59
<b>Figure 5-15:</b> Stresses at the leading cell location from the FE model result.....	60
<b>Figure 5-16:</b> Stresses at the leading cell location from the experiment result (Tsuha et al. 2012). ....	60
<b>Figure 5-17:</b> Summary of model results with failure criterion.....	61
<b>Figure 5-18:</b> Displacement curves with varying $G_0$ values.....	62
<b>Figure 5-19:</b> Displacement curves with varying $\mu_0$ values. ....	63
<b>Figure 5-20:</b> Displacement curves with varying $\zeta$ values. ....	64
<b>Figure 5-21:</b> Displacement curves with varying $\beta$ values.....	64
<b>Figure A-1:</b> Model results for stable tests ICP1-OW1.....	73
<b>Figure A-2:</b> Model results for stable test ICP2-OW1. ....	73
<b>Figure A-3:</b> Model results for stable test ICP2-OW2.....	74
<b>Figure A-4:</b> Model results for stable test ICP4-OW1. ....	74
<b>Figure A-5:</b> Model results for metastable tests ICP2-OW3.....	75
<b>Figure A-6:</b> Model results for metastable tests ICP4-TW1.....	75
<b>Figure A-7:</b> Model results for unstable tests ICP3-OW1.....	76
<b>Figure A-8:</b> Model results for unstable tests ICP3-TW1.....	76
<b>Figure A-9:</b> Model results for unstable tests ICP3-TW2. ....	77
<b>Figure A-10:</b> Model results for unstable tests ICP3-TW3. ....	77

# List of Tables

<b>Table 3-1:</b> SANISAND-MS model parameters classification .....	34
<b>Table 3-2:</b> Mineralogy and index properties of Fontainebleau NE34 sand.....	35
<b>Table 3-3:</b> Monotonic model parameters.....	35
<b>Table 3-4:</b> Monotonic test scenarios.....	36
<b>Table 3-5:</b> Cyclic model parameters.....	38
<b>Table 3-6:</b> symmetric test scenarios.....	39
<b>Table 3-7:</b> Summary of results from symmetric test .....	42
<b>Table 3-8:</b> Asymmetric test scenarios .....	43
<b>Table 4-1:</b> Initial sand state properties .....	47
<b>Table 4-2:</b> Pile information.....	47
<b>Table 4-3:</b> Details of different mesh discretization schemes .....	49
<b>Table 5-1:</b> Cyclic loading scenarios .....	52

---

# Nomenclature

$G$ : soil shear modulus  
 $M$ : critical stress ratio (triaxial compression)  
 $p_{atm}$ : reference atmospheric pressure  
 $G_0$ : dimensionless shear modulus  
 $e$ : current void ratio  
 $e_0$ : initial void ratio  
 $\Psi$ : state parameter  
 $e_c$ : critical void ratio  
 $\lambda_c$ : CSL shape parameters  
 $\xi$ : CSL shape parameters  
 $p_c$ : critical state mean stress  
 $q_c$ : critical state deviatoric stress  
 $g$ : gravitational acceleration  
 $m$ : yield locus opening parameter  
 $\mathbf{e}^e$ : elastic strain tensor  
 $\mathbf{s}$ : deviatoric stress tensor  
 $\varepsilon_v^e$ : elastic volumetric strain  
 $p$ : mean stress  
 $K$ : bulk modulus  
 $\nu$ : Poisson ratio  
 $c$ : critical state parameter  
 $M_e$ : stress ratio in extension  
 $M_c$ : stress ratio in compression  
 $R'$ : tensor of deviatoric plastic flow direction  
 $L$ : plastic multiplier  
 $\varepsilon_v^p$ : plastic volumetric strain  
 $\mathbf{e}^p$ : plastic deviatoric strain tensor  
 $D$ : dilatancy coefficient  
 $n^{b,d}$ : void ratio dependent parameters  
 $b_{ref}$ : reference distance for normalization



## Table of Contents

<b>Abstract</b> .....	<b>ii</b>
<b>List of Figures</b> .....	<b>iii</b>
<b>List of Tables</b> .....	<b>iv</b>
<b>Nomenclature</b> .....	<b>v</b>
<b>Chapter 1</b> .....	<b>3</b>
<b>Introduction</b> .....	<b>3</b>
<b>1.1 Background</b> .....	<b>3</b>
1.1.1 Wind energy .....	3
1.1.2 Offshore piles and their loading conditions.....	5
<b>1.2 Motivation of the specific problem</b> .....	<b>6</b>
<b>1.3 Research questions</b> .....	<b>7</b>
<b>1.4 Research outline</b> .....	<b>8</b>
<b>Chapter 2</b> .....	<b>9</b>
<b>Literature study</b> .....	<b>9</b>
<b>2.1 Cyclic/dynamic design of offshore turbine on jackets</b> .....	<b>9</b>
<b>2.2 Drained cyclic behaviour of sand</b> .....	<b>13</b>
2.2.1 Cyclic loads and soil responses .....	13
2.2.2 Behaviour of sand under drained cyclic loading .....	14
<b>2.3 Constitutive modelling</b> .....	<b>16</b>
2.3.1 Constitutive model evolutions .....	17
2.3.2 SANISAND model family.....	17
<b>2.4 Piles' response under Axial Cyclic Loading</b> .....	<b>21</b>
2.4.1 Pile responses under varies cyclic axial loads .....	21
2.4.2 Installation effect on displacement piles.....	25
<b>2.5 Methodology</b> .....	<b>28</b>
<b>Chapter 3</b> .....	<b>30</b>
<b>Constitutive Model and Parameter calibration</b> .....	<b>30</b>
<b>3.1 Mathematical formulation of the model</b> .....	<b>30</b>
3.1.1 Soil elasticity .....	30
3.1.2 Yield surface .....	30
3.1.3 Critical state locus .....	31
3.1.4 Flow rule .....	32
3.1.2 Kinematic hardening and Bounding surface .....	32
3.1.3 Memory surface .....	33
<b>3.2 Calibration of model parameters</b> .....	<b>34</b>

---

3.2.1 Calibration of monotonic parameters .....	35
3.2.2 Calibration of cyclic parameters .....	38
<b>Chapter 4 .....</b>	<b>45</b>
<b>Finite Element Model .....</b>	<b>45</b>
4.1 Experiment configurations.....	45
4.2 Finite Element Model Dimension .....	46
4.2.1 General model dimension.....	46
4.2.2 Verification of the model size .....	47
4.3 Finite Element Mesh .....	49
<b>Chapter 5 .....</b>	<b>52</b>
<b>Analysis and Results .....</b>	<b>52</b>
5.1 Stable response .....	53
5.2 Metastable Tests .....	55
5.3 Unstable Tests .....	57
5.4 Comparison result summary and Interaction diagram.....	59
5.5 Parameter study .....	61
5.4.1 Influence of $G_0$ .....	62
5.4.2 Influence of $\mu_0$ .....	62
5.4.3 Influence of $\zeta$ .....	63
5.4.4 Influence of $\beta$ .....	64
<b>Chapter 6 .....</b>	<b>65</b>
<b>Conclusions and Recommendations .....</b>	<b>65</b>
6.1 Conclusions .....	65
6.2 Limitations .....	66
6.3 Recommendations .....	66
<b>Reference.....</b>	<b>67</b>
<b>Appendix.....</b>	<b>73</b>

# Chapter 1

## Introduction

### 1.1 Background

#### 1.1.1 Wind energy

Since the 21st century, climate change has been a key issue worldwide. Sustainable development is always demanding, which is aimed at building environment-friendly and resource-economical societies. High emissions of carbon dioxide and other global warming gases mostly come from the increasing number of industries and the growing number of world populations. This fact drives energy technologies to develop towards low-carbon and sustainable ends other than traditional environmental harmful fossil fuels or thermal powers. To a sustainable end, wind power is a good alternative in coastal areas and the contracting areas of the open continent where the wind resources could be easily taken good advantage of. Moreover, wind energy is competitive not only for its low carbon emission and less operation pollution but also for its low maintenance costs.

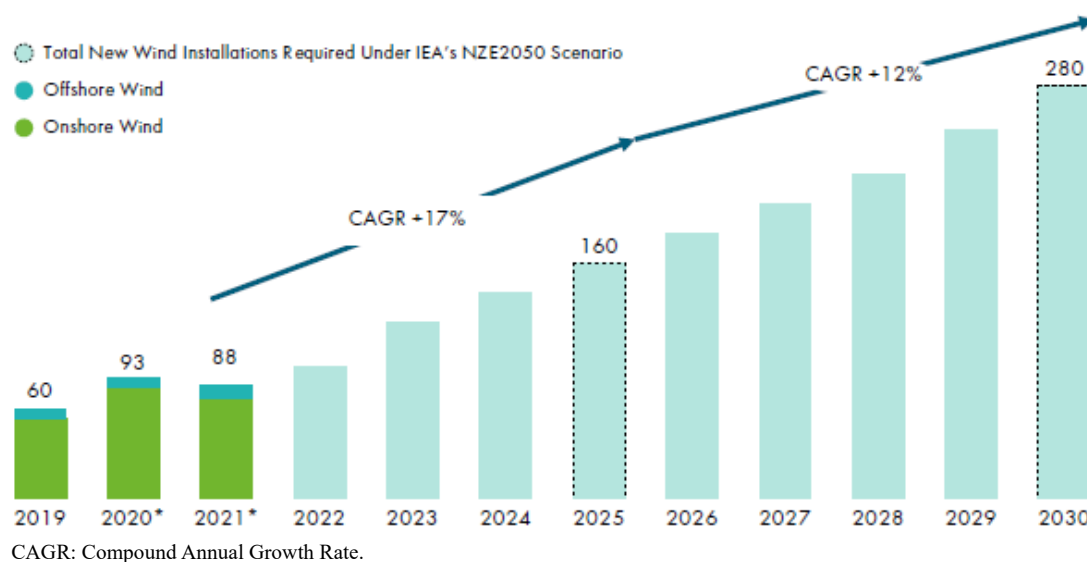


**Figure 1-1:** Annual wind installations plan by 2050, volume in 2022-2024 and 2026-2029 are estimates. (World Energy Outlook, 2020).

Based on the current Global Wind Energy Council (GWEC), global onshore and offshore wind power capacities totalled 743 gigawatts (GW) at the end of 2020 (Global Wind Energy Council, 2021). More than 1.1 billion tons of CO<sub>2</sub> globally would be avoided, approximately equal to Japan's yearly carbon emissions as the world's fifth-largest emitter. China is the top generator of wind energy

worldwide, with a total installed capacity of a little over 288 GW by the end of 2020. The United States is the second-largest wind power producer of roughly 122 GW of wind capacity installed. The major list of world wind farm installation countries also includes Germany (62.85 GW), India (38.63 GW), and Spain (27.24 GW) (IRENA, 2021). Wind markets will continue to increase in the future as the wind power industry matures and deployment costs decrease. Furthermore, a global net-zero aim by 2050 is driving the wind industry's explosive expansion (Global Wind Energy Council, 2021).

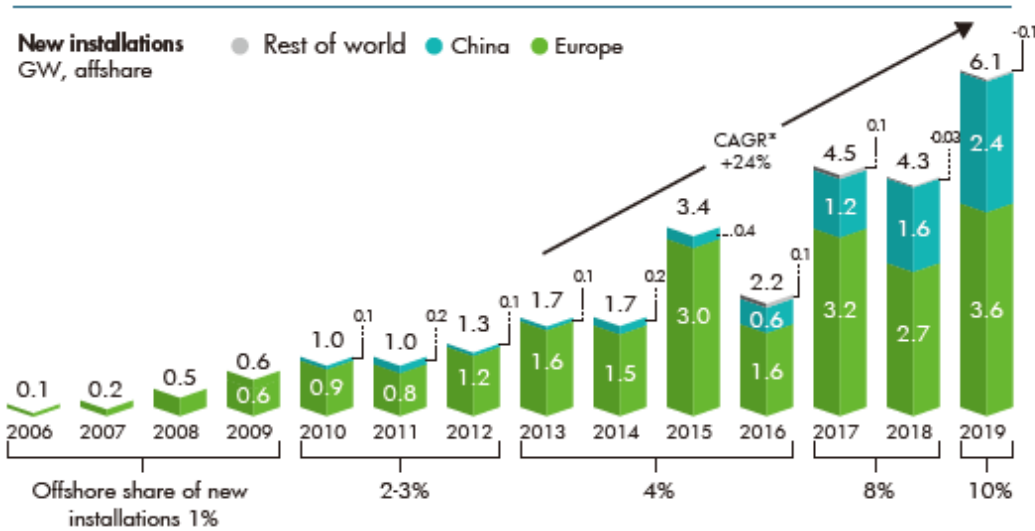


**Figure 1-2:** New installations of Offshore wind (GWEC Market Intelligence, March 2020).

In Europe, it is expected that wind energy will meet at least 21% of total electricity consumption (European Commission, 2013). In the United States, a similar aim has been established, with wind energy expected to provide 20% of the country's electricity by 2030. (S. Lindenberg et al., 2008). To present, onshore winds have provided the majority of wind power installations. Offshore winds, on the other hand, are typically stronger and more uniform than land winds, making them more efficient in generating wind energy. Offshore wind farms are becoming increasingly popular around the world. The United Kingdom has the world's greatest offshore wind installed capacity (Garrad Hassan GL et al., 2010), while Denmark has been using electricity coming from offshore wind for nearly two decades (Sawyer S et al., 2010).

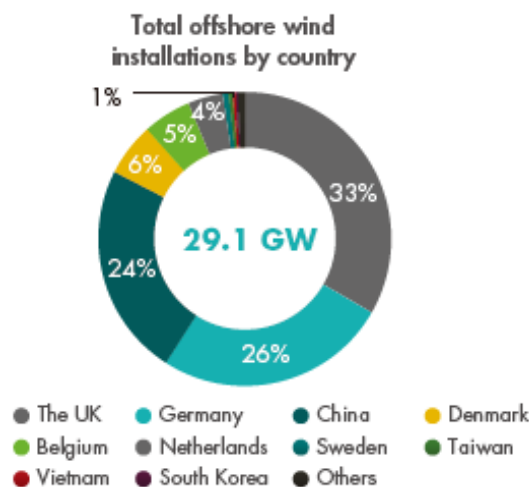


**Figure 1-3:** Total offshore wind installations by 2019 (Global Wind Energy Council, 2020).

Nonetheless, the growth of offshore wind farms was restricted by the high cost of the supporting foundations, which represents around a quarter of the total budget of an offshore wind farm. Therefore, to achieve cost-benefit, wind farms with higher capacity generators and in deeper waters, advanced offshore technologies are in great demand. The demanding new technologies or advanced models should be able to make deep offshore structures more efficient and reliable and significantly reduce the cost of constructing support structures.

### 1.1.2 Offshore piles and their loading conditions

The support structures of offshore wind turbine (OWTs) come in a variety of types and sizes. Conventional bottom-mounted (non-floating) support structures can be classified into five primary types: monopile structures, tripod structures, jacket structures and gravity structures. At the end of 2019, 75% of the total offshore wind power installed globally was on monopolies, and jacket structures take second place of offshore wind farm foundations (Walter Musial *et al.*, 2020).

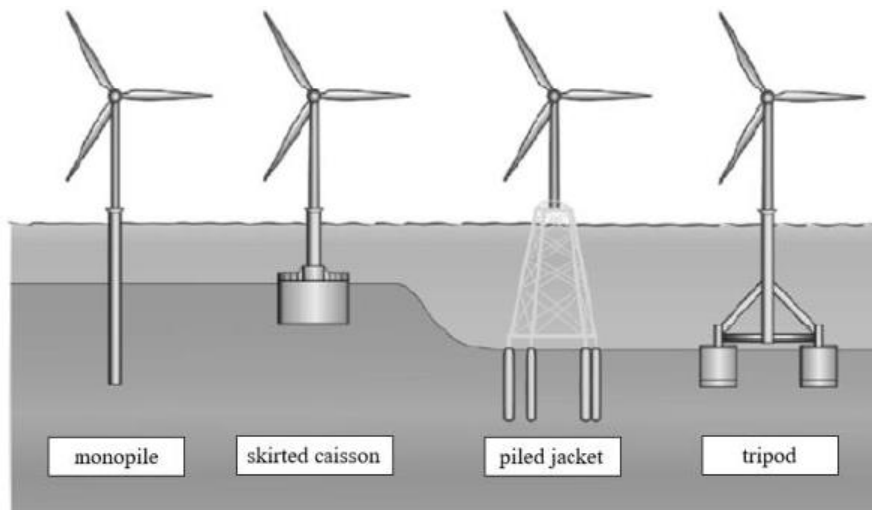


**Figure 1-4:** Typical foundation for bottom-mounted OWTs (modified after Kaynia, 2018)

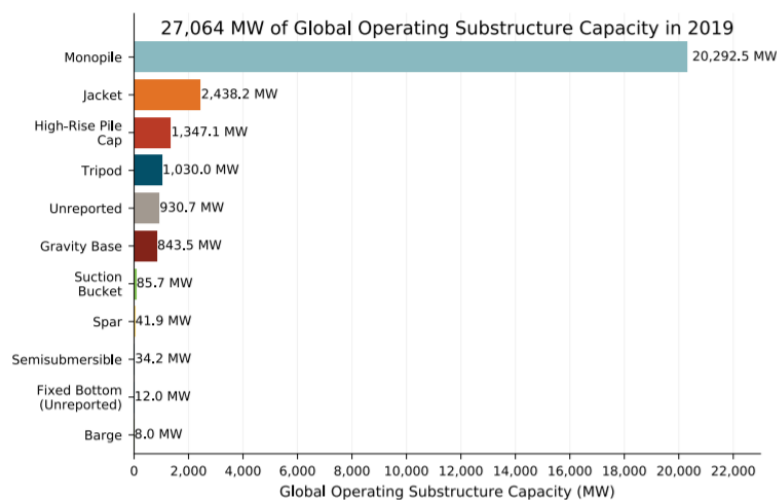


**Figure 1-5:** Global usage of installation capacity of offshore foundations (Walter Musial *et al.*, 2020).

When the water depth is less than 30 meters, monopiles and gravity-based structures are widely employed as OWT support structures in engineering practice (Gavin *et al.*, 2011). The dominant

concern on the cyclic response of OWTs is the lateral contact between monopiles and seabed soil (Lamo GM et al. (2018); Carswell W et al. (2016) and Guo Z et al. (2015)). Jacket foundations are more appealing for larger OWTs when the water depth surpasses 30 m. (e.g., Damiani R et al., 2016). The jacket foundation mostly overtakes axial loads transferred from the upper wind turbine, as seen in Figure 1-6. (Bhattacharya S et al., 2017).

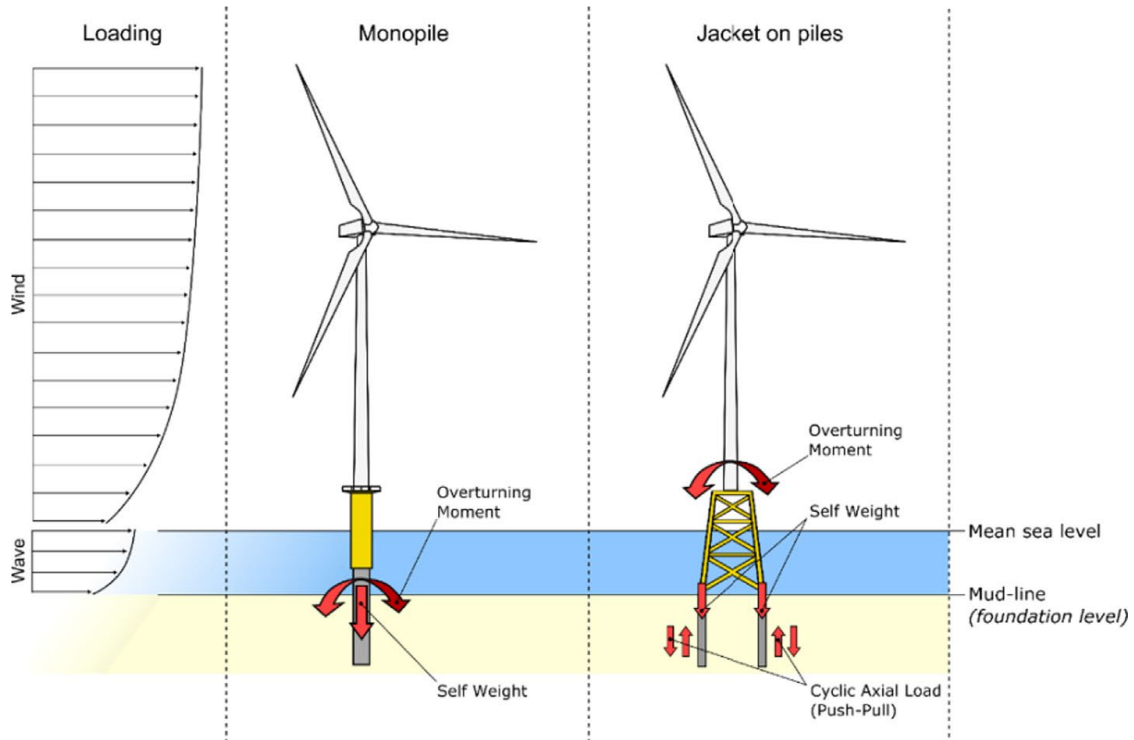


**Figure 1-6:** Cyclic load transferred to OWT monopile and jacket foundations (Bhattacharya S et al., 2017).

Because of the different loading types, magnitudes, and soil conditions, offshore piles are designed differently than onshore piles. In particular, axial loads on offshore piles are often an order of magnitude higher than onshore piles, and offshore piles are subjected to significant lateral stresses. And, of course, cyclic stresses account for a large amount of the axial and lateral loads on offshore piles. More advanced research techniques are appealing in the design of those multiple offshore piles to obtain precise, feasible and reliable offshore foundation structures. Optimizing offshore large wind farms also gives the benefit of saving budget and increase profit.

## 1.2 Motivation of the specific problem

OWTs are frequently loaded in diverse cyclic or dynamic conditions, which could be either lateral or axial loads or a combination of those two. It is very common that loads on offshore structures come from natural wind, currents or, in some extreme case, earthquakes. Apart from natural loads, the installation and normal operation of the offshore structures often impose large cyclic loads on the sub-piles. Unlike lateral capacity for monopile foundations, the design of piles under jacket structure in an offshore loading environment would require sufficient axial capacity. Pile design was traditionally based on empirical relations and then calibrated by load tests given different input

conditions. Jardine and Standing (2000) drew out a cycle shaft failure interaction diagram based on full-scale pile tests driven in Dunkerque, France. The response of piles under axial cyclic loads was divided into three types in the interaction diagram: a stable (S) response where no cyclic failure observed for loading cycles larger than 1000, a metastable (MS) response where failure occurs after 100 and within 1000 loading cycles, and an unstable (US) response when pile reaches failure in less than 100 loading cycles. The failure mode of axially loaded offshore piles may differ depending on the pile type and soil conditions. Jardine et al. (2012) and Merritt et al. (2012) developed further analytical methodologies for axial cyclic design, providing practical guidance for offshore wind farm foundations. Both papers summarized cyclic stability interaction diagrams, which can be used to aid in the evaluation of overall axial capacity degradation under cyclic loading conditions for driven piles, as proposed earlier by Karlsrud et al. (1986), Lehane et al. (2003), and Jardine and Standing (1988; 2000).

The general purpose of this study is to reproduce the behaviour of displacement piles under drained axial cyclic loading through finite element modelling. A newly developed soil constitutive model SANISAND-MS will be implemented in capturing high-cyclic soil stress evolutions. The loading conditions and the finite element model dimension will be the same as the experimental settings recorded in a paper from Tsuha et al. (2012). The simulation results will be discussed in 3 response types, and an interaction diagram will be summarized.

### **1.3 Research questions**

The scope of this thesis is to use advanced soil-structure modelling techniques to simulate the performances of displacement piles under drained axial cyclic loading, which is more common to happen on multiple offshore piles like piled jackets. Additionally, the simulation results will be compared to experimental results summarized by Tsuha *et al.* (2012).

The object of this thesis is trying to reproduce and analyze the following pile-soil interaction behaviours:

- How will the model react to different cyclic-to-average cyclic load ratios, and will they confirm the results recorded in paper Tsuha et al. (2012)?
- Whether the clear stable, metastable and unstable region will exist or not?
- What are the stress paths in each cyclic behaviour region, respectively?
- How will the constitutive model parameters influence the finite element model performance?

The basic purpose is to test the predictive capability of the 3D FE framework through the implementation of SANISAND-MS constitutive model for pile responses under axial cyclic loadings. However, limited by the finite element model used, the pile installation process will not be modelled in this thesis.

## 1.4 Research outline

A newly developed soil constitutive model named SANISAND-MS is adopted in this paper to capture the soil behaviour mathematically. The constitutive model constants are calibrated using the laboratory results from PROJET DE RECHERCHE SOLCYP (ANR + PN) (2008-2012), which has the same soil properties as the sand (Fontainebleau NE34) used in this work. After the calibration, the constitutive model parameters are implemented into the finite element scripts. The finite element model is built in the open-sourced platform OpenSees, with the mesh obtained from OpenSees PL.

After the introduction and the literature study parts, the main content of the study starts from chapter 3, where the detail of the constitutive model and the parameter calibration is illustrated. The properties of the sand used, the experimental data adapted to calibration and the final parameters selected are all interpreted in this chapter.

After that, chapter 4 comes to the establishment of the finite element model. In this part, the model dimension and the selection of the optimal mesh scheme will be detailly described.

In chapter 5, the modelling part starts as well as the analysis of the simulation results. In this chapter, all the loading scenarios will first be introduced, followed by model performances of each scenario.

Chapter 6 is the conclusion part, including the limitations and possible suggestions for future research.

Finally, all the finite element model results are concluded in the Appendix.

## Chapter 2

# Literature study

This chapter includes a literature study of corresponding theoretical background and past observation for this thesis. First, research findings that are nowadays available on jack-supported turbines under cyclic/dynamic loading conditions will be extended in this section. The evolution of constitutive soil models is followed, as well as the information of constitutive model used in later finite element modelling part. Then, sand behaviour in response to cyclic loading conditions is given. Finally, research on the behaviour of displacement piles under axial cyclic loads is presented mostly based on experiments recorded in the paper from Tsuha *et al.* (2012).

### 2.1 Cyclic/dynamic design of offshore turbine on jackets

Jacket structures on multiple foundations are commonly being used to support OWTs in water zone deeper than 30 meters and shallower than 60 meters. Jackets can be supported on either 3-legged shallow foundations (suction caissons) (Figure 2-1) or 4-legged deep foundations (piles) (Figure 2-2). Piled foundation installations require expensive equipment and are usually accompanied by noise pollution. Therefore, the eco-friendly nature of an alternative suction bucket foundation has been developed because it does not require large pilling equipment, and a shorter installation time can be expected for caisson installations.

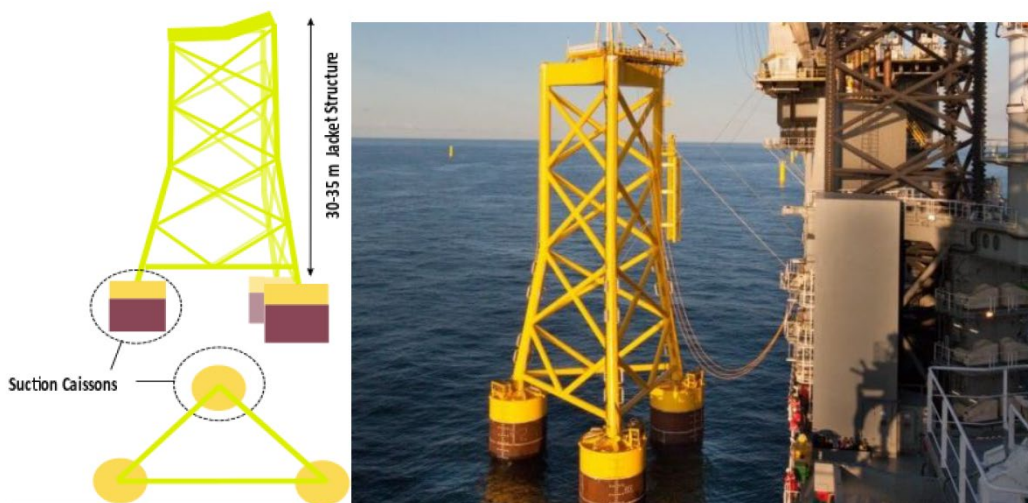


**Figure 2-1:** Example of a 3-legged jacket structure on suction caissons (Jalbi S. *et al.*, 2019).



**Figure 2-2:** Example of a 4-legged jacket structure on piles (Cheng-Yu Ku and Lien-Kwei Chien, 2016).

Offshore wind turbines are installed with increasing electricity generation capacity in deeper waters but are frequently exposed to cyclic/dynamic loading conditions. The natural rotor frequency of turbine operation can also cause the vibration of the soil-structure system, apart from cyclic/dynamic loads from the offshore environment. The vibration of the soil-structure system involves careful consideration of both the structure and its foundations' stiffness. The load is transmitted to the subsoil through moment force in a monopile supported wind turbine. The load transmission for a jacket supported wind turbine is mainly by axial pull-push (Figure 1-6). As a result, the axial capacity and axial stiffness of the supporting foundations should be assessed during the jacket design process. Vibration modes for jackets supported on multiple pile foundations differ from those for jackets supported on shallow suction caissons under dynamic loading conditions. When it comes to deep piling foundations for offshore wind turbines, they are sharing a sway-bending vibration mode (Figure 2-3) for the very high foundation stiffness. However, for jackets on suction caissons, there will be a rocking vibration mode (Figure 2-4) and is characterized by the foundation's vertical stiffness.

In Dynamics of Structures (2011), When the structure is loaded dynamically, the dynamic amplification factor (DAF) is described as a dimensionless number that defines how many times the deformations or stresses caused by the static loads should be amplified to the deformations or stresses generated by the dynamic load. In order to evaluate the DAF of a dynamic response, a good estimate of the wind turbine system's natural frequency is critical in the construction of jacket structures and their foundations. A jacket structure design includes the overall structure dimensions, structural components such as jacket legs and bracing, and the foundation type and its dimensions. The optimal design of the jacket dimensions, stiffness of jacket member and its foundations are desirable to make sure that the final configuration obtained can contribute to a smaller dynamic amplification factor.

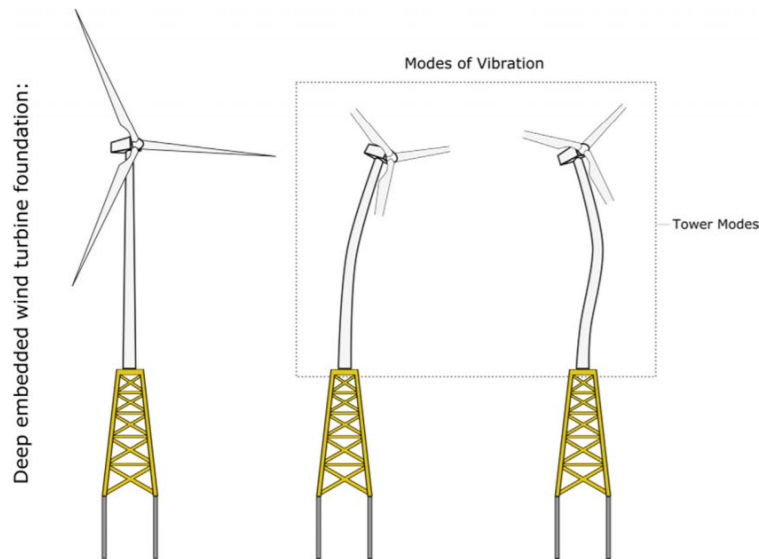


**Figure 2-3:** Sway-bending vibration mode of pile supported wind turbines (Bhattacharya S. et al., 2017).

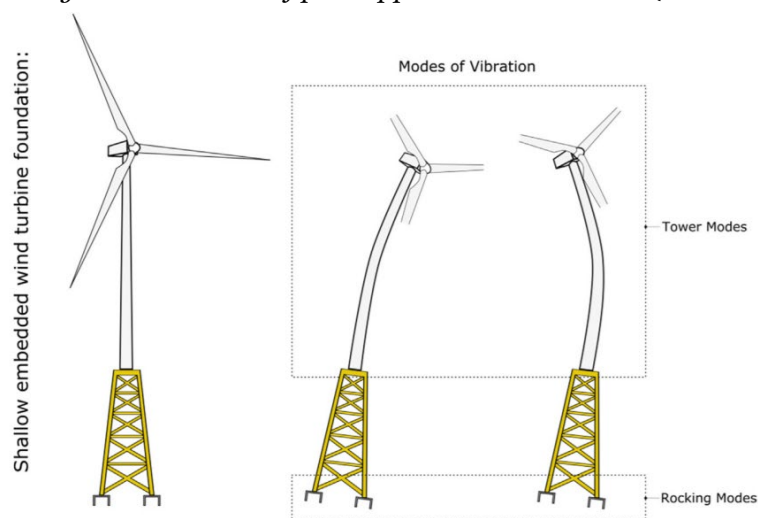


**Figure 2-4:** Rocking vibration mode of caisson supported wind turbines (Bhattacharya S. et al., 2017).

Many researchers have been studying the dynamic performance of jacket supported OWTs for a long time (Wei, K. et al., 2017; Abhinav, K.A. and Saha, N., 2018). Wei, K., and coworkers (2017) employed finite element analysis to examine the dynamic reactions of jackets under waves of various periods and energies by importing DAF. It illustrates that, depending on the wave amplitude and period, the DAF value will be substantial at 1.2-1.3. Dong, W. et al. examined the fatigue process of cyclic loads on OWT foundations, which is critical to long-term damages (2011). When examining the structural response, Abhinav, K.A., and Saha, N. (2015) performed numerical research on understanding the vibration mode of the soil-structure system. To simulate the Soil-Structure-Interaction (SSI) effect, springs were dispersed throughout the foundation shaft (2015). They also looked at the effect of ground non-linearity in the sand with different densities (loose, medium dense and dense) and found that the effect of SSI is stronger in looser sands (Abhinav, K.A. and Saha, N., 2018). SSI impacts could change the normal frequency and dynamic responses of the leg and bracing members, according to Shi, W. et al. (2015). When it came to studying the fatigue damage to offshore buildings, pile group effects were also a major factor. Saleh Jalbi and Subhamoy Bhattacharya (2018)

recently suggested a manual technique for estimating a jacket's natural frequency by including (SSI). The earth is assumed to be a collection of linear springs, and the jacket is idealized as an analogous beam.

To include the influence of dynamic loading in the design of OWTs supported on jacket foundations, Jalbi S. et al. (2019) introduced the rocking vibration mode and the approach to avoid it. Due to their low frequency, rocking vibration modes can become tuned to the rotor frequency, resulting in resonance effects. It is preferable for the jacket structures to have a sway-bending mode as the first mode of vibration. The frequency of the jackets is governed by two parameters: (a) the ratio of vertical foundation stiffness ( $k_v$ ) to superstructure stiffness ( $k_t$ ); and (b) the aspect ratio (ratio of base dimension to tower dimension) of the jacket-tower geometry. A sway-bending mode will be induced by the foundation's high vertical stiffness combined with a higher aspect ratio (wider base of the tower L), as seen in Figures 2-5 and 2-6.

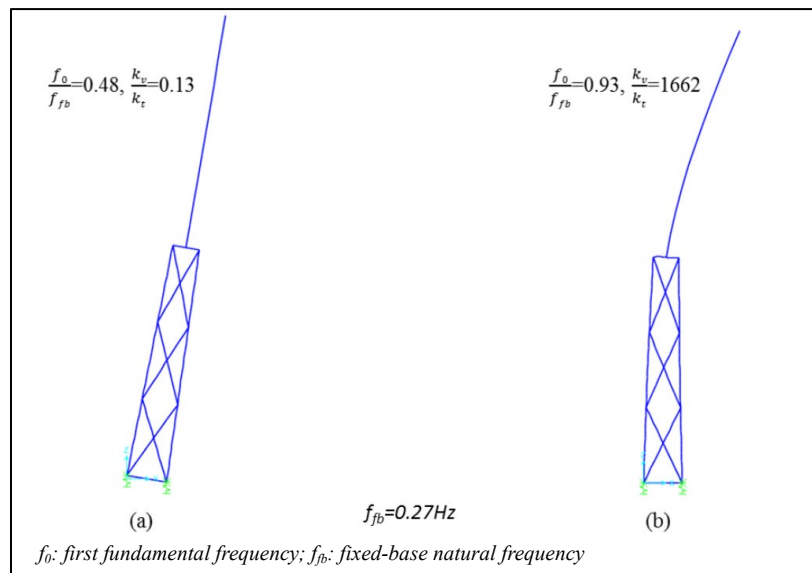


**Figure 2-5:** Finite Element Model output of vibration modes; (a) Rocking mode for low  $k_v$  values; (b) Sway-bending mode for high  $k_v$  values (Jalbi S. et al., 2019).

Because of the OWTs' cyclic/dynamic loading environment, the preliminary and comprehensive design of OWT support structures are multidisciplinary and often challenging processes. Van der Tempel J. (2010) presented a doctoral dissertation on an overall design procedure for the offshore wind farm, including the fatigue assessment in the frequency domain. Finding a better and more cost-effective design requires structural optimization. To this purpose, A computer-aided method can greatly aid in the discovery of an optimal structure design (Muskulus M. et al., 2014). Chen IW et al. (2016) used numerical analysis to conduct research on several types of jackets that support OWTs. Furthermore, Wei K. et al. (2017) investigated dynamic reactions under various types of wave loads by introducing DAFs for regular and irregular waves. Fatigue damage on OWT jackets was explored by Dong W. et al. (2011) and Seidel M et al. (2014). Saleh Jalbi and Subhamoy Bhattacharya (2020) provided a simplified design technique of the concept and tender design stages to give direction on assessing the financial viability, based on excellent work from the literature above and others. The

design process was summarized in a flowchart to visualize the multidisciplinary work. The required calculation procedures are workable either through a series of spreadsheets or simple hand calculations. The paper has shown that the system's strength and stiffness are significant in the overall structure's performance. The acquired results from an example problem utilizing this reduced design method revealed dimensions that were similar to those reported in a more complete design.

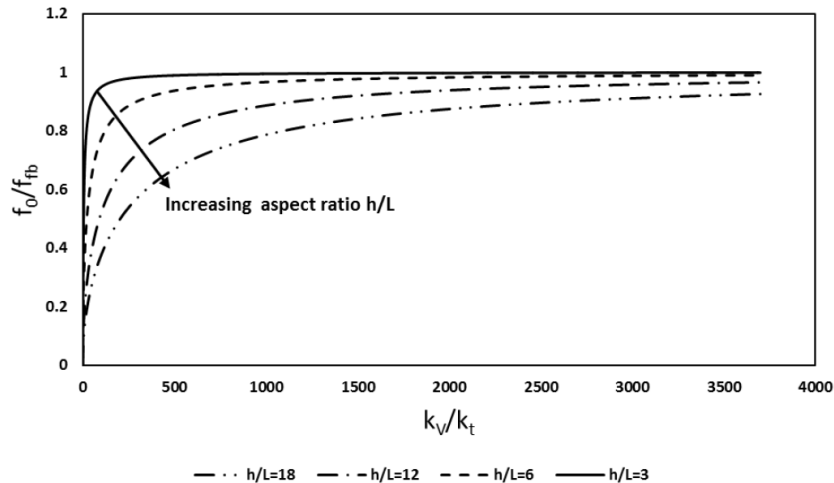


**Figure 2-6:** Influence of aspect ratio on the system's vibration mode (Jalbi S. et al., 2019).

## 2.2 Drained cyclic behaviour of sand

In an offshore environment, sands under offshore foundations are very common to expose to cyclic loading conditions, for instance, loads coming from waves, earthquakes, and winds. The sand behaviour under cyclic loadings can respond in different ways giving different initial drainage and boundary conditions. When the soil has high permeability (i.e., sand/gravel) or the loading rate is slow, and the water drainage is relatively quick, drained loading conditions are expected to occur. Significant accumulation of permanent deformations would occur in a drained cyclic loading condition after a certain number of loading cycles.

### 2.2.1 Cyclic loads and soil responses

Cyclic loading has different soil responses than monotonic loadings. The stress path, as well as the combination of average and cyclic shear stress, have a significant impact on the soil cyclic strength and failure mode under cyclic loading. Cyclic loading can be categorized into four types (Figure 2-7) based on the combination patterns of cyclic stresses:

- One-way loading: shear stress does not change in sign;
- Two-way loading: shear stress can be positive or negative;
- Symmetric loading: mean shear stress is zero in the case of two-way cyclic loading;
- Asymmetric loading: the mean shear stress is non-zero.

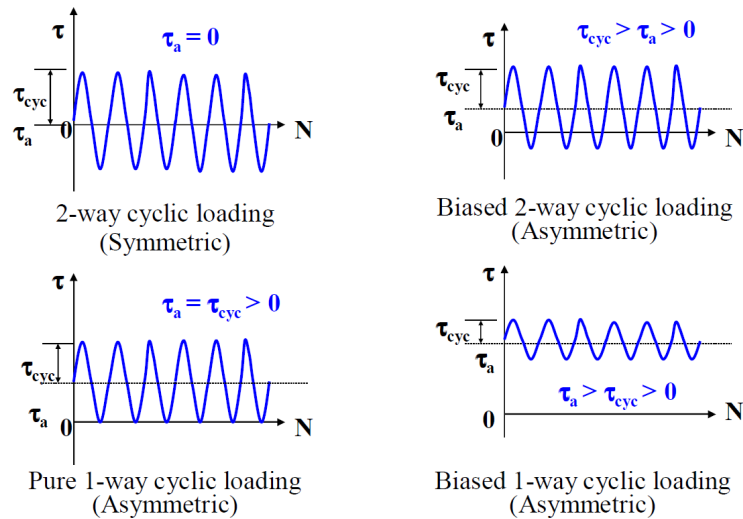


**Figure 2-7:** Types of cyclic loading (Randolph and Gouvernec, 2011).

Cyclic loading can cause soil capacity to be reduced to a level lower than that of monotonic loading. Under two-way loads, this drop in soil capacity is considerably more important. The load-displacement curves in Figure 2-8 illustrate this phenomenon. Because displacement accumulates during cyclic loading, the displacement of soil under cyclic loading is greater than the displacement of soil under monotonic loading at the same load, as seen in the diagram.

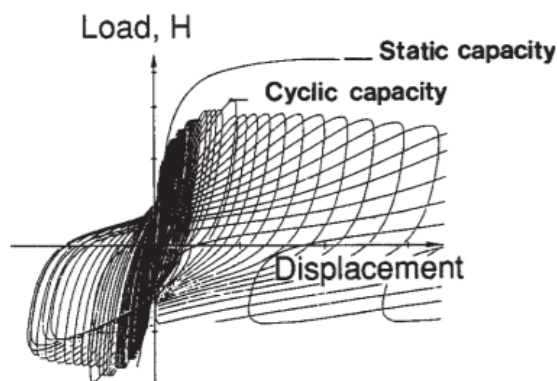


**Figure 2-8:** Load-displacement curve from monotonic and cyclic model tests (Dyvik et al. 1989).

During the drained cyclic loading, the load tends to change the soil fabric and volume. And that is why the displacement under cyclic loading is larger than that of monotonic loading. If the conditions change to undrained cyclic loading, the volume change will be restricted by the low permeability of the soil and the low compressibility of water. The normal stresses forced on soil consequently transmitted to the pore water, which gives rise to pore water pressure and reduces the effective stresses accordingly.

### 2.2.2 Behaviour of sand under drained cyclic loading

Sand behaviour has been researched extensively, both experimentally and numerically, all around the world. Experimental results provide an insight into sand behaviour trends and tendencies under a

variety of loading scenarios. The majority of the data formed the basis for Critical State Theory, which was developed by Roscoe et al. (1958) and Schofield and Wroth (1968) to accommodate and understand the basic behavioural characteristics of the soil. Although the critical state framework was originally created for the monotonic behaviour of clay, it has lately been extended to sands (Been & Jefferies, 1985; Coop & Lee, 1993; Jefferies & Been, 2000).

The behaviour of sand under cyclic loading has been extensively studied through laboratory tests under both drained and undrained conditions, for example, simple cyclic shear (Silver & Seed, 1971) and triaxial and resonant column tests (Khan, Z. et al., 2011). The amplitude of cyclic shear strain, the effective confining stress, the initial soil index properties (e.g., relative density  $D_r$ ), and the number of cycles applied are the major factors affecting cyclic behaviour and the accumulation of volumetric strains (densification) (e.g., Seed & Silver, 1972; Wichtmann T. et al., 2005). However, unlike monotonic situations, the cyclic behaviour of sand in drained condition has not firmly established by a critical state framework.

The strain accumulation of sand due to cyclic loading was investigated by Wichtmann T. et al. in 2005. They employed a high-cyclic constitutive model to estimate strain and/or stress accumulation under cyclic loading with the number of cycles reaching 103 to 106 and with small cyclic amplitudes. The density, grain size distribution on the direction, strain amplitude, average stress and cyclic preloading history are the primary parameters that determine the drained cyclic behaviour of sand, according to their research. Results of their work are concluded in Figure 2-9 below.

In Figure 2-9 (a), curves of identical accumulated strain  $\varepsilon^{\text{acc}} = \text{constant}$  are plotted in the  $e$ - $p$  plane for the same strain amplitude ( $\varepsilon^{\text{ampl}}$ ), average stress ( $\eta^{\text{av}}$ ) and the number of cycles ( $N$ ). The growing slope of the curves with  $\text{acc} = \text{constant}$  is visibly in opposition to the critical state line's (CSL in Figure 2-10) inclination. As a result, it verifies the previous conclusion that the accumulation rate cannot be simply characterized by the void ratio's distance  $e$ - $e_c$  from the CSL.

The accumulated strain  $\varepsilon^{\text{acc}} - N$  relations are shown in Figure 2-9 (b), in which  $\varepsilon^{\text{acc}}$  are normalized by  $f_{\text{ampl}}$ ,  $f_p$ ,  $f_Y$ ,  $f_e$  and  $f_\pi$  with  $f_\pi = 1$ . After  $N = 104$ , strain accumulation typically increases in proportion to the number of loading cycles, eventually reaching over-logarithmic accumulation.

The influence of strain amplitude on cyclic strain accumulation is depicted in Figure 2-9 (c), where  $\varepsilon^{\text{acc}} - N$  curves were plotted over nine different cyclic stress amplitudes with the same  $p^{\text{av}}$ ,  $\eta^{\text{av}}$  and relative density  $I_{D0}$ . Again, the strain accumulates as the number of cycles  $N$  increases, and higher  $q^{\text{ampl}}$  clearly results in larger strain accumulations.

In the discussion of the influence of average stress on the cyclic behaviour, the normalized  $\varepsilon^{\text{acc}}$  was plotted by average mean pressure ( $p^{\text{av}}$ ) given in Figure 2-9 (d). It can be recognized that accumulated strain  $\varepsilon^{\text{acc}}$  is decreasing with the increasing  $p^{\text{av}}$ . Apart from this, results also found that the rate of strain accumulation increases with the average stress ratio  $\eta^{\text{av}} = q^{\text{av}} / p^{\text{av}}$ . Accordingly, the direction of accumulation (cyclic flow rule) is completely determined by the  $\eta^{\text{av}}$  value.

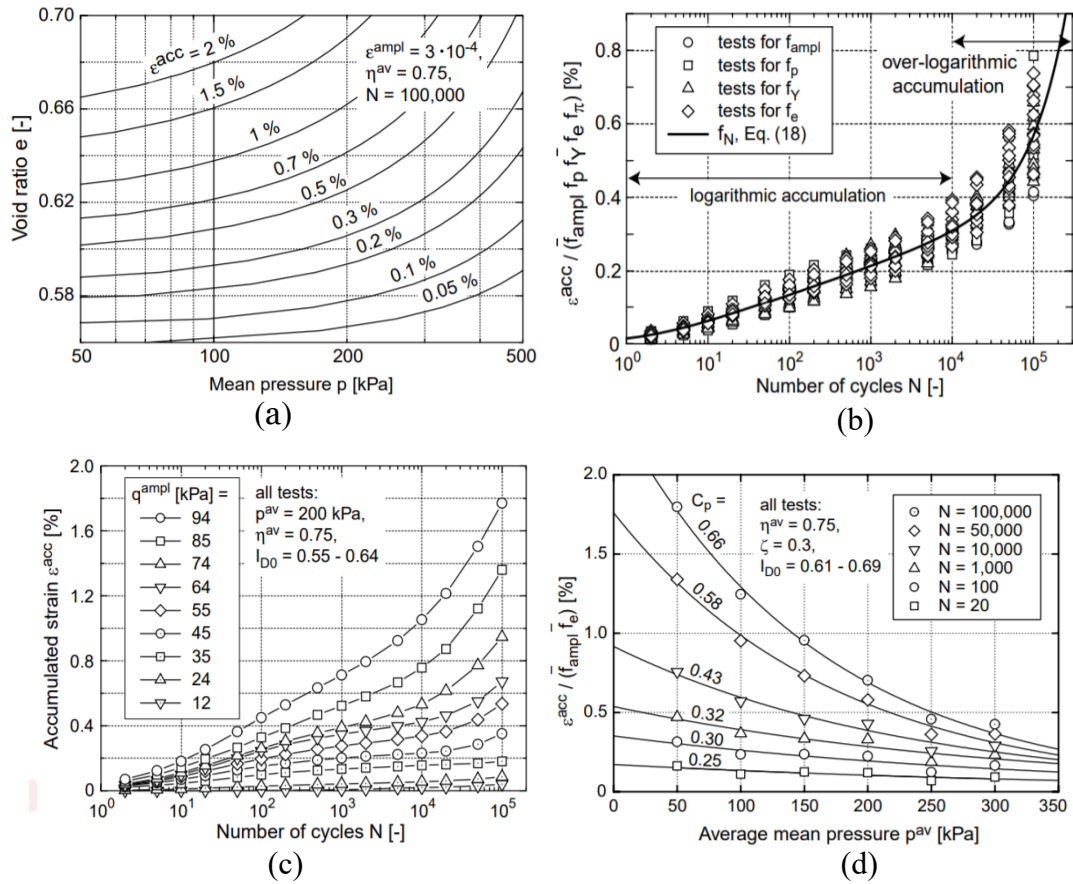


**Figure 2-9:** Factors influence the sand cyclic behaviour: (a) density and mean pressure; (b) number of cycles; (c) stress amplitude; (d) average mean pressure. (Wichtmann T. et al., 2005).

Aside from Wichtmann T.'s efforts, other findings showed that if the applied cyclic numbers  $N$  is high enough, depending on the test conditions, the cumulative strains will approach a constant value known as a "dynamic" critical state (Youd, 1972). However, the association between these "dynamic" equilibrium values and the critical state under monotonic loading remains unknown. According to studies by Wichtmann and Triantafyllidis (2004a; 2004b), using purely empirical methods, the cyclic/dynamic loading history will contribute to the final magnitude of densification in drained cyclic tests. Meanwhile, they used energy and/or fabric considerations to seek explanations for the impact of the sand's volumetric strain memory. More recently, more reliable laboratory tests with a variety of initial conditions and loading scenarios of fine sand provided repository to design and verify a constitutive model for numerical use (Wichtmann and Triantafyllidis, 2015; 2016).

## 2.3 Constitutive modelling

The constitutive model of soils is a set of equations describing stress ( $\sigma$ ) – strain ( $\epsilon$ ) relations in soils. The  $\sigma$ - $\epsilon$  relations in soil are of great complexity, including non-linearity and visco-elasto-plasticity. Meanwhile, the soil type and the stress history would all affect the soil constitutive behaviours. Numerous (implicit) soil constitutive models have been formulated to date, some of the famous constitutive models are introduced below, as well as the well-known SANISAND framework.

### 2.3.1 Constitutive model evolutions

The constitutive model of soils originates from Hooke's law which describes purely elastic stress-strain relations towards models involving soil plasticity, such as the Mohr-Coulomb model, named LEPP model (Linear Elastic Perfect-Plastic model). Later, a hyperbolic model developed, which gives a more reasonable stress-strain relationship for deviatoric stress paths. The hardening soil (HS) model (Hchanz *et al.*, 1999) and hardening soil small (HS-small) model (Benz, 2006.) extend the possibility of capturing the stress dependency stiffness and the memory of pre-consolidation stress. The HS-small model is an extended HS model which includes strain-dependent stiffness behaviour and makes it able to describe hysteresis and damping in cyclic loading. However, all those models still do not show any softening behaviours of soil.

For clay and soft soils, the Cam-Clay model was first built in 1963 by Roscoe and Schofield with the famous Critical State framework. Then in the literature Roscoe and Burland initially described the modified Cam-Clay model (1968). (Modified) Cam-Clay model takes loading history and stress(path)-dependent stiffness differences into account, which gives a reasonable model for primary loading of normally - consolidated clays and soft soils while less suitable for over-consolidated clay and sands. Other than the Cam-Clay model, soft soil model, soft soil creep model and S-Clay1S model came along successively. These models were updated and improved gradually by taking time-dependent behaviour (creep) and stress-induced anisotropy, bonding, and de-structuration (S-Clay1S) into considerations.

The UBCSAND model, PM4SAND model, and SANISAND model family are some of the most well-known sand models. Beaty and Byrne developed the UBCSAND model at the University of British Columbia (UBC) (1998). It's a sand model based on plasticity that may depict the cyclic accumulation of strains (drained) or pore water pressures (undrained). The UBCSAND model can also be used to observe liquefaction behavior, though it is not necessarily realistic. Boulanger and Ziotopoulou (2012, 2015, 2017) developed the PM4SAND model at the University of California, Davis. It's also an advanced model for sandy soils that are subjected to cyclic loads and exhibit densification or liquefaction. The fabric effect and densification are included in the PM4SAND model, although it is merely a 2D model and not suitable for static loading. The PM4SAND model is based on bounding surface plasticity (Dafalias & Manzari, 2004), which is essential for the SANISAND model and its future improvements. Since the constitutive model that will be employed in this thesis is named the Memory-Enhanced SANISAND model (SANISAND-MS model) (Liu *et al.*, 2019), which is also based on the bounding surface plasticity framework, the SANISAND model will be addressed in detail in the following contents.

### 2.3.2 SANISAND model family

For constitutive modelling of soil behaviours under cyclic loading (earthquake, offshore environment loads, etc.), it is desirable to have a model that can capture soil responses after a number ( $N$ ) of loading cycles. Explicit and implicit methods can be used to predict cyclic soil deformations over loading cycle number  $N$ . For the explicit method, accumulated strains are directly linked to the number of loading cycles  $N$ . In this case, extensive laboratory tests are commonly demanded,

explicit models. Nevertheless, in an implicit method, the stress-strain increments are calculated after each loading cycles, so the overall strain accumulations are obtained through time integration of all stress strains. And this is the way how constitutive model takes effect in an implicit model.

Critical state soil mechanics (CSSM) was able to represent the stress-strain behaviour of typically consolidated clays and, to a lesser extent, sands under monotonic loading when used in combination with elastoplasticity theory. When it is employed to represent sand behaviour under cyclic loading, however, the results are far from satisfactory. This implies that independent of CSSM, more emphasis should be placed on the classical hardening plasticity theory. In addition to monotonic loading conditions, sophisticated plasticity ideas such as kinematic hardening, multi-surface plasticity, and bounding surface plasticity were developed to describe cyclic loading circumstances. In 1978, Mroz et al. proposed an anisotropic hardening model for soils, and in 1980 and 1986, Dafalias & Herrmann presented the bounding surface plasticity soil model. Those are the first attempt at advanced plasticity models, which are still based on CSSM as premises.

### Critical state theory

The critical state theory, introduced by Roscoe et al. in 1958, was also a fundamental component of this model. Casagrande (1936;1938) was the first to propose the concept of critical void ratio  $e_c$ , followed by different methods for assessing this soil property. The critical void ratio, according to a widely accepted definition at present, is the void ratio when the sand volume in the shear zone does not change. This situation is equivalent to zero pore pressure and effective strains when saturated sand is loaded undrained. The sand state is defined by the distance between the present sand void ratio and the critical state void ratio, as defined by the state parameter (Been and Jefferies, 1985).

$$\Psi = e - e_c \quad (\text{Eq. 2-1})$$

The initial void ratio  $e_0$  for a sand state denser than critical (point a) is below the Critical State Line, as shown in Figure 2-10 (CSL). When a load is applied, it tends to consolidate at point  $a_d'$ , then dilate at point  $a_c'$  on the CSL, where  $e = e_c$  and failure occurs. A sand state looser than critical, as indicated by point b in Figure 2-10, will respond to drained compression. As the load is applied, the sand consolidates until it approaches the CSL (point  $b_c'$ ) and fails. For sand that is originally looser than critical, there is no dilative behaviour.

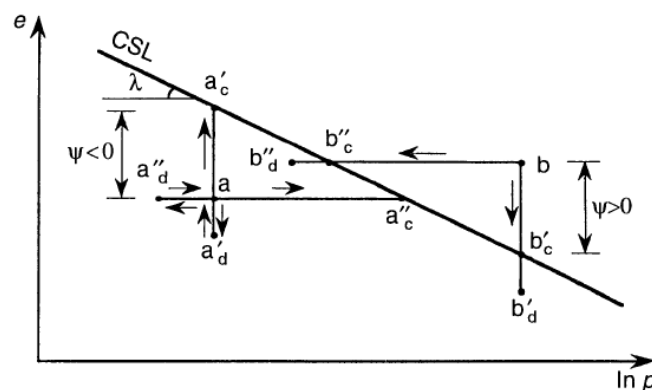


**Figure 2-10:** Stress paths in  $e$ - $\ln p$  space for a state denser than critical (point a) and looser than critical (point b) (Manzari, 1997).

## SANISAND MODELS

The word SANSAND is an acronym for 'Simple ANIsotropic SAND,' and it was originally used in Taiebat and Dafalias (2008). Manzari & Dafalias presented the first SANISAND model in 1997, which was a critical state two-surface model (yield surface and boundary surface). It is based on CSSM and focuses on the 'implicit' simulation of sand cyclic behaviour using bounding surface plasticity. The yield surface identifies stress states in which plastic strains are either insignificant or considerable. The bounding surface aims to 'bound' the yield surface inside and separates the pre-failure or admissible stress states from the ultimate stress states.

Due to some limitations in the original formulations, more SANISAND models within the SANISAND family were introduced over the decades. Among these expansions, improvements were dedicated on, for example, fabric and dilatancy effects (Papadimitriou *et al.*, 2001; Dafalias and Manzari, 2004; Petalas *et al.*, 2019 (SANISAND-F); Petalas *et al.*, 2020 (SANISAND-FN)), incremental non-linearity (SANISAND-Z) (Dafalias and Taiebat, 2016), etc. Specifically, SANISAND04 was introduced by Dafalias and Manzari (2004), which considers the impact of fabric variations during the dilatant phase of deformation on the subsequent contractive reaction when load increments are reversed. This refinement resulted in a more accurate reproduction of sand behaviour upon undrained cyclic loads.

### SANISAND04 and SANISAND-MS

Though improved in 2004 by introducing fabric change effects, the SANISAND04 model showed better performance in comparison with experimental data, it cannot reproduce ideal stress-strain relation and soil response under a large number of cyclic loads. Unrealistic strain accumulation and pore pressure increase was observed in the SANISAND04 model results. Instead, a newly developed SANISAND-MS (Liu *et al.*, 2019) model exhibited improved model performance, with better strain accumulation under cyclic drained triaxial loading and a more realistic number of loading cycles to liquefaction.

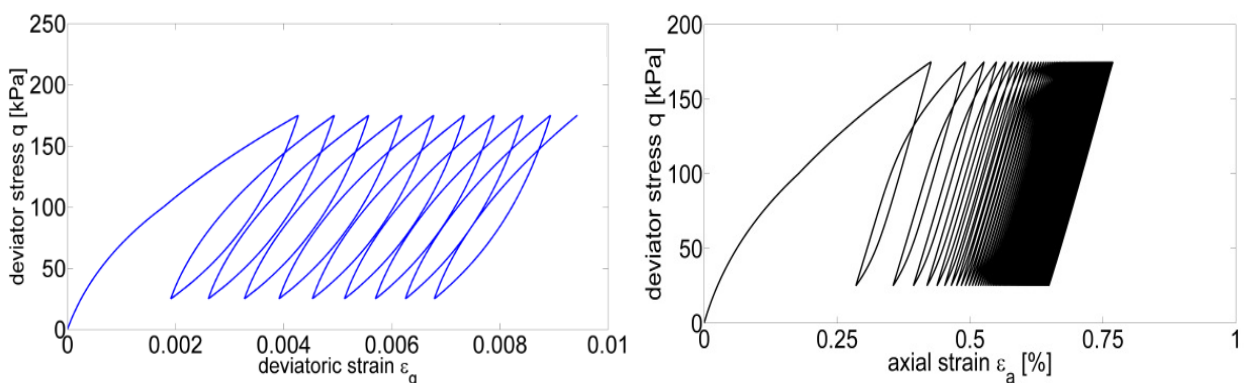


**Figure 2-11:** Comparison of drained results by SANISAND04 (left) and SANISAND-MS (right) (Liu, H. Y., 2020).

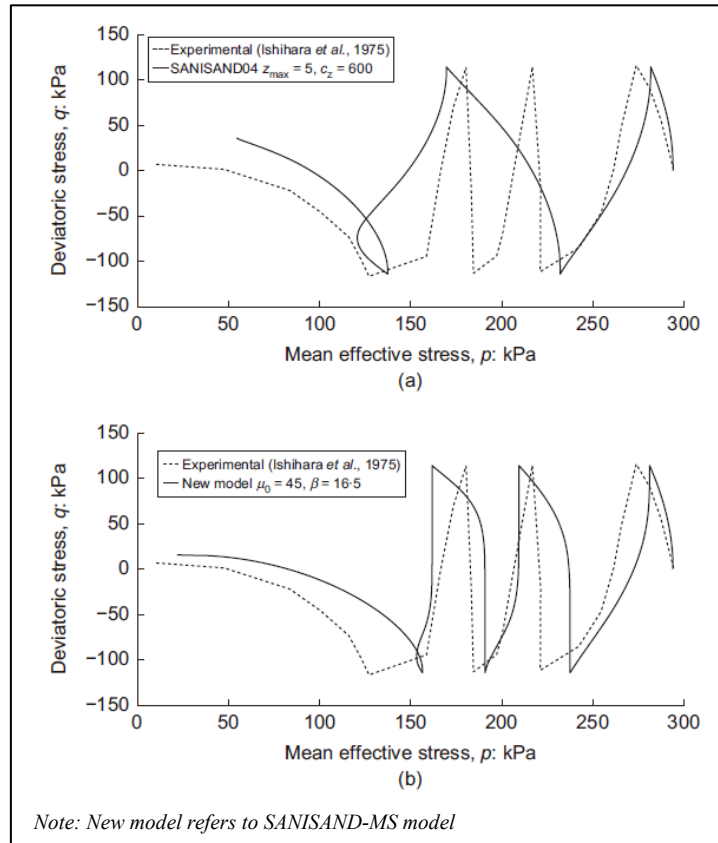


**Figure 2-12:** Comparison of undrained results by SANISAND04 and SANISAND-MS (Liu et al., 2019).

SANISAND-MS is a three-surface constitutive model that, by adding an extra memory surface (Figure 2-13) to the previous two-surface model SANISAND04, could well describe the phenomenon of cyclic ratcheting. The phenomenon ‘sand ratcheting’ indicates the gradual accumulation of plastic strains after a large number of loading cycles. Under high-cyclic loading, the extra memory surface MS is employed to track the induced fabric changes and permit variable stiffness or dilatancy. The expansion and translation of the memory surface capture the changes in soil fabric. Plastic strains are the only ones that cause changes in memory surface size.

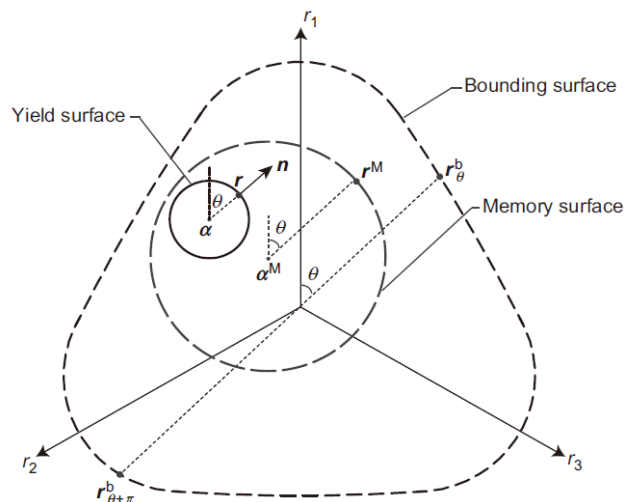


**Figure 2-13:** Relevant surfaces in SANISAND-MS model (Liu et al., 2019).

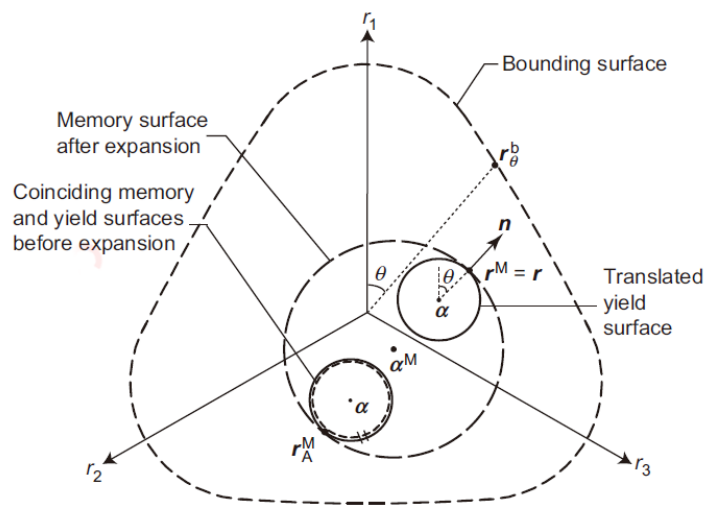


**Figure 2-14:** Evolution of MS & YS in SANISAND-MS model (Liu et al., 2019).

## 2.4 Piles' response under Axial Cyclic Loading

Interest in the behaviour of sand under cyclic loading grew in the 1980s since the first Tension Leg Platform installed in 1984, which continuously brought failure challenges to the safe operation of the structure. Larger and heavily loaded deeper fixed platforms like Cognac jacket set in 320m water also drew the safety concerns to those 'over-sized' offshore structures. The safe operation of offshore structures relies mostly on the capacity of their foundations which are quite often exposed to harsh wind loads, waves or even earthquakes in an offshore environment. Even though laboratory tests may be conducted to analyse site-specific cyclic soil behaviours, the influence of the installation process, the access to cyclic pile capacity and deformation from cyclic soil behaviour still raise concerns.

### 2.4.1 Pile responses under varies cyclic axial loads

Chan & Hanna (1980) illustrated in model tests that the cyclic response of displacement piles in the sand is affected by the number ( $N$ ) and the frequency ( $f$ ) of cycles, the mean shaft load ( $Q_{\text{mean}}$ , often referred to as  $Q_{\text{average}}$  or  $Q_{\text{ave}}$  or  $Q_{\text{av}}$ ) and the shaft cyclic amplitude ( $Q_{\text{cyclic}}$ , often referred to as  $Q_{\text{cyc}}$  or  $Q_{\text{cy}}$ ), as defined in Figure 2-15, the sand characteristics, the pile dimensions ( $L$ ) and the loading history. The type of cyclic loadings, two-way (TW) or only one-way (OW) tension cyclic loading, also influences the piles' behaviours.

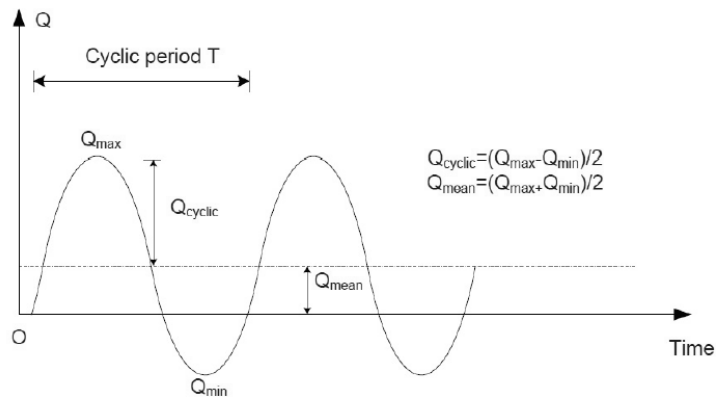


**Figure 2-15:** Cyclic loading definitions (Tsuha et al. 2012).

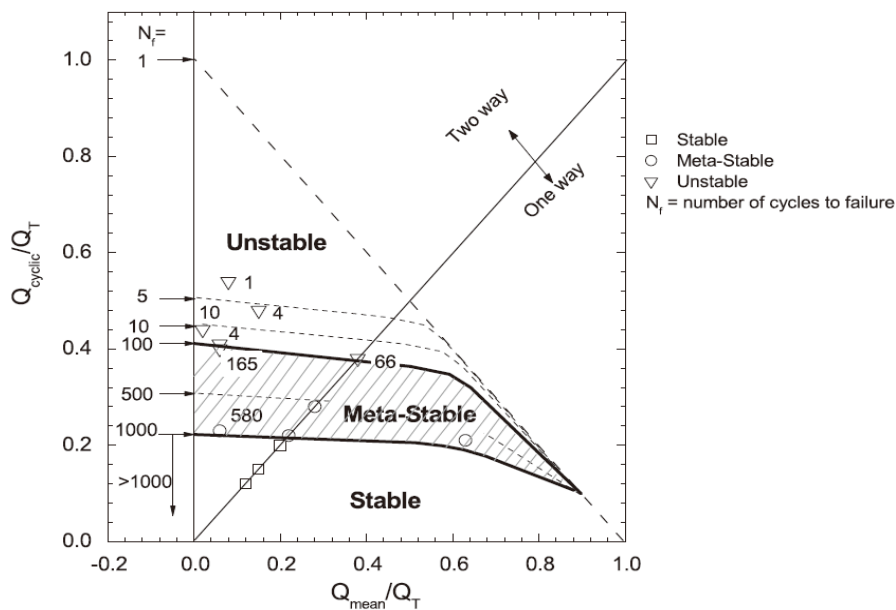


**Figure 2-16:** Interaction diagram with different cyclic-to-average ratios and response types obtained from Mini-ICP tests (Tsuha et al. 2012).

Jardine and Standing (2000) conducted multiple axial cyclic experiments on full-scale piles in Dunkerque, France, and found that piles driven into sand can respond to axial cyclic loading in one of three ways: stable, unstable, or metastable, depending on the combination of  $N$ ,  $Q_{mean}$ , and  $Q_{cyclic}$ . Figure 2-16 depicts a response pattern that may vary depending on soil conditions and pile dimensions. Tsuha et al. (2012) and Rimoy et al. (2012) gave further details regarding each response type of axially loaded piles driven in the sand:

- **Stable (S) Zone**

Under either TW or OW (in this example, tensile) stress, axial displacements stabilize or accumulate very slowly over hundreds of cycles (Figure 2-17). Minor reductions in local radial effective stresses (Figure 2-18) were observed, but axial capacity gains due to changes in dilatancy (Figure 2-19).

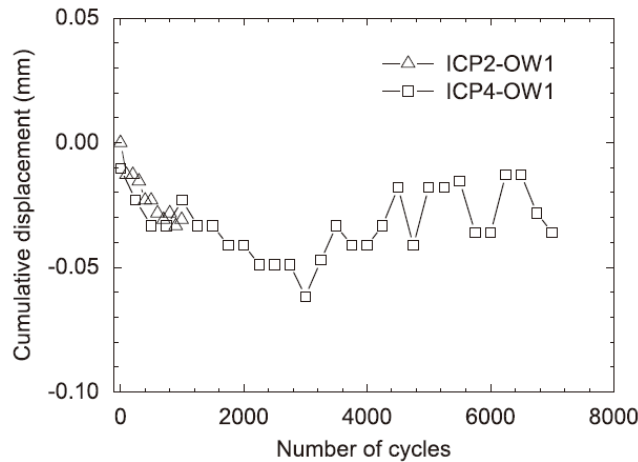


**Figure 2-17:** Cumulative displacement from stable cycling (Tsuha et al. 2012).

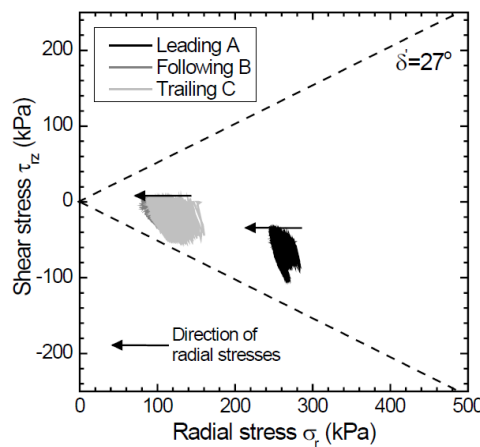


**Figure 2-18:** Effective stress path from stable cycling (Rimoy et al., 2012).

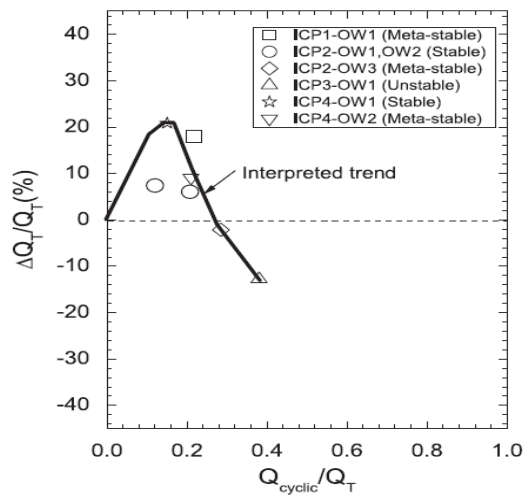


**Figure 2-19:** Tensile capacity gains in stable zone (Tsuha et al. 2012),  $Q_T$  -static tension capacity.

- **Metastable (MS) Zone**

Over tens of cycles, displacements increase at a modest rate without stabilizing. Cyclic failure (pile head displacement reaches 10% diameter, 3.6mm in this case; or sharp increase in slope of Displacement-Number of cycles curve.) develops with  $100 < N < 1000$ .

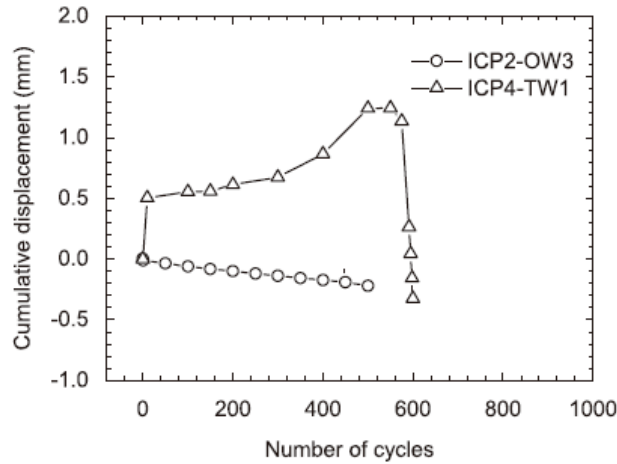


**Figure 2-20:** Cumulative displacement from metastable cycling (Tsuha et al. 2012).

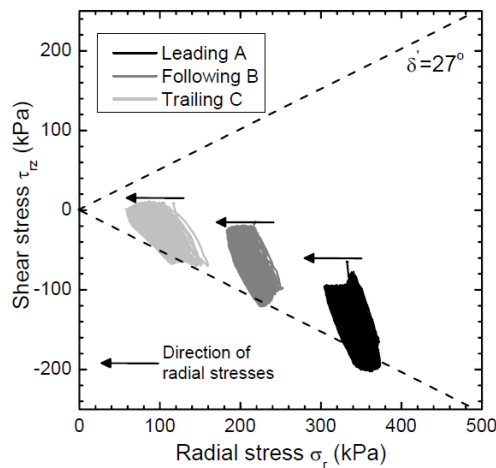


**Figure 2-21:** Effective stress path from metastable cycling (Rimoy et al., 2012).

- **Unstable (US) Zone**

Displacements accumulate rapidly under OW or TW cycling. Cyclic failure occurs in less than 100 number of loading cycles. A “butterfly-wing” stress path developed. Radial effective stress reduces sharply (Figure 2-23) and degrades shaft capacity substantially.

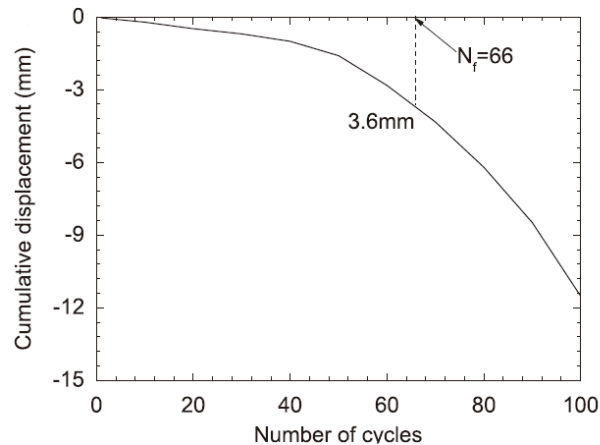


**Figure 2-22:** Cumulative displacement from unstable cycling (Tsuha et al. 2012).

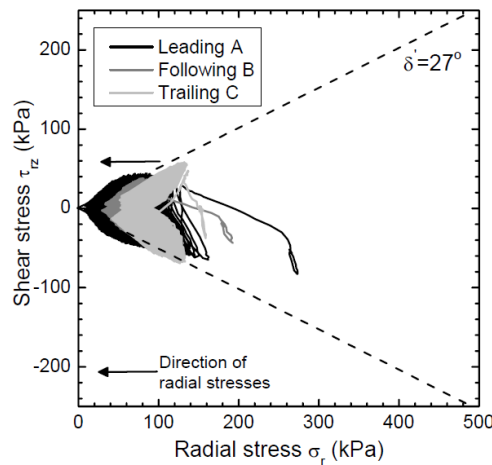


**Figure 2-23:** Effective stress path from unstable cycling (Rimoy *et al.*, 2012).

Limited field experiments performed at Labenne and Dunkerque in France (Lehane, 1992; Lehane *et al.*, 1993; Chow, 1997) verified the top-down process of progressive failure proposed by Jardine (1991; 1994). Together with laboratory tests of the ‘Imperial College Piles’ (ICPs) (Tsuha *et al.*, 2012; Jardine *et al.*, 2013a, 2013b) that offered accurate measurement of local shaft shear and normal stress, approaches to access the axial capacity and deformation of piles under cyclic loadings summarized following characteristics:

- The shaft capacities of piles are controlled by the evolution of local radial effective stresses,  $\sigma'_{rc}$ , which depends principally on the local cone resistance  $q_c$ , while less dependent on the free field vertical effective stress  $\sigma'_{v0}$ . The increasing relative pile tip depth  $h/R$  can sharply reduce  $\sigma'_{rc}$  developed against the pile shafts.
- Axial cyclic loads with similar frequency as offshore storms could lead to large pile head displacements and cyclic failures under the maximum cyclic loads lower than static pile capacities.
- The response depends critically on the loading conditions (OW or TW cyclic loadings). Two-way cyclic loading could cause more severe pile responses compared to one-way loadings. Extreme two-way conditions can even lead to pile failures within a small number of loading cycles.
- The installation and set-up process strongly affects the capacity of piles driven in the sand.
- A progressive top-down failure process was observed as piles can ‘unzip’ from the upper region downwards. This phenomenon can happen mostly on relatively long flexible piles.

#### 2.4.2 Installation effect on displacement piles

One thing to mention is that the mini-ICP piles were installed by jacked cycles which influenced most of the final pile capacities. The installation effects make the study of axially loaded displacement piles complicated because of the complex properties of the soil around the pile shaft. The soil around the displacement pile is severely distorted, according to laboratory investigations by Chong (1988), White (2002), and Dijkstra *et al.* (2008), among others. Among all kinds of pile installation methods, jacked driven piles are of most popularities which could give higher pile capacity while with less pollution.

In traditional engineering practice, the installation effects are unclear but accounted for in empirical design methods. To date, though of great interest, modelling pile installation is still a big challenge. The pile installation process involves large strain deformation, which could not be modelled using a small strain FEA code involving Lagrangian schemes. In contrast, the Eulerian and Arbitrary Lagrangian-Eulerian (ALE) schemes involve a large strain material point method (MPM) that successfully simulates the cone penetration tests. From the works of N. Phuong *et al.* (2014), the MPM with installation effect matched well with the result from the centrifuge test. In contrast, MPM without installation effect gave a head force around four times smaller than the experimental result (Figure 2-24). Apart from the load-displacement curves with comparison to the centrifuge test result, stress state change and the density change around the pile shaft during pile installation were also studied by N. Phuong *et al.* (2014) using MPM modelling.

### Load-displacement curve

The base bearing capacity obtained from the simulation with MPM matched well with the centrifuge test results, as shown in Figure 2-22. For both loose and medium dense sand, the capacity after a 0.1D penetration was matched well, adopting an MPM including the installation effect. However, the load-displacement curves of MPM simulation without installation effect differentiated significantly with the centrifuge results, both for loose and dense sand. The end bearing capacity without installation effect was around 2-4 times smaller than that with installation effects.

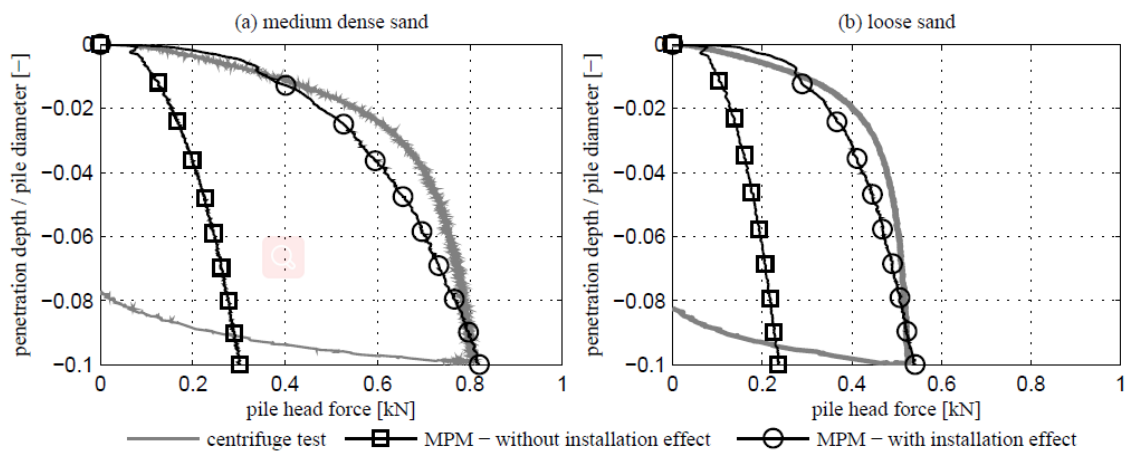


**Figure 2-24:** Pile capacity comparison with/without installation process. (N. Phuong *et al.* 2019).

### Stress state change

From the same simulation result, the radial stress distribution after 10D penetration was recorded, as depicted in Figure 2-25. The radial stress increased substantially both in horizontal and vertical directions, with a maximum near the pile tip.

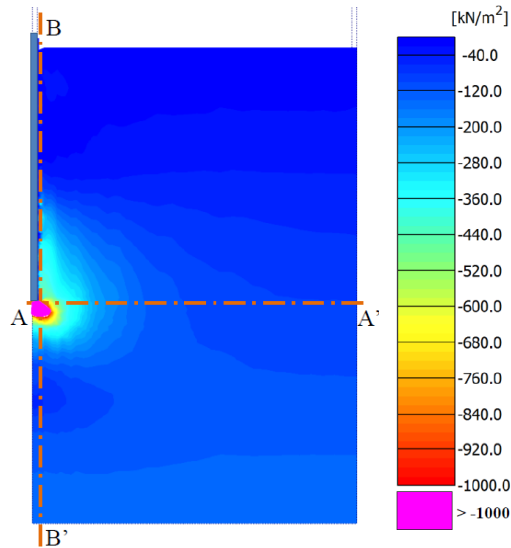


**Figure 2-25:** Radial stress after 10D penetration from simulation (N. Phuong et al. 2019).

### Void ratio change

Except for a small dilative region at the corner of the pile tip, it is obvious from Figure 2-26 that the soil around the pile was densified with a lower void ratio after pile penetration, both in medium dense sand and loose sand. The significant shear strains in the soil near the corner pile may explain the dilative zone. As a result, the shearing process superimposes compaction of the soil adjacent to the pile, while compaction dominates further away from the pile corner, which is aligned with other researchers' findings (e.g., K. Mahutka et al., 2006).

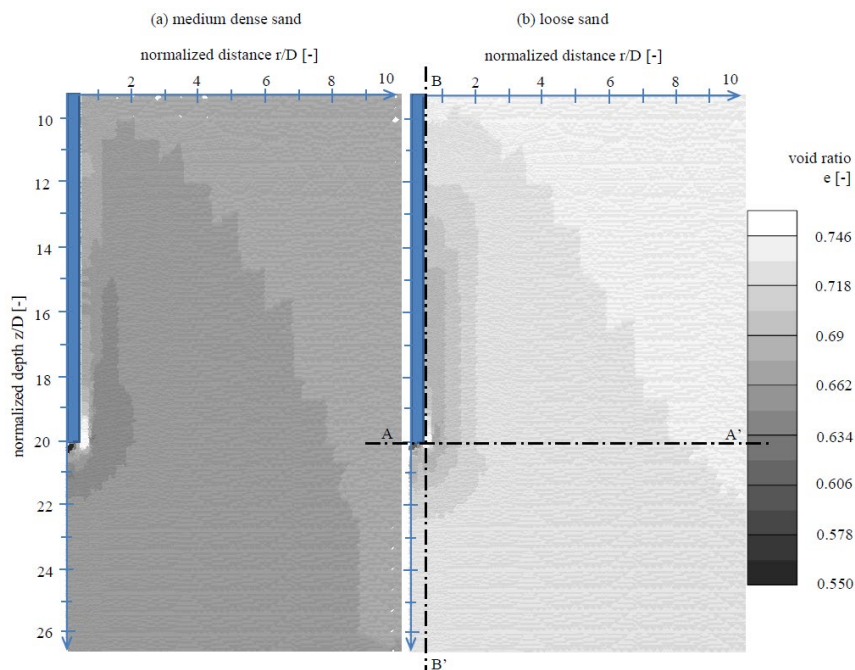


**Figure 2-26:** Density change after 10D penetration. MPM model results for a) medium dense sand (void ratio=0.68) and loose sand (void ratio=0.75) (N. Phuong et al. 2019).

## 2.5 Methodology

In geotechnical engineering, three main methods are used to explore soil response under various geotechnical conditions: field tests, laboratory tests and numerical modelling. Field tests are performed in-situ with the virgin soil conditions and surrounding environment. A field test could reproduce the most similar stress states, dimensions, loading conditions and boundary conditions like drainage conditions. However, it is usually very expensive and less feasible to proceed with such a full-scale test since the result relies strongly on in-situ conditions. An alternative down-scaled method was introduced aiming at testing soil behaviours in the lab, with less expensive input and higher possibilities of output. The drawback of downscale laboratory tests is the difficulty of recreating similar soil states and natural conditions as on-site, thus reducing the reliabilities of the test results.

More recently, physical modelling has gained great interests from researchers. Geotechnical centrifuge modelling was first proposed by Phillips in 1869 and was rediscovered around fifty years ago. One main purpose or advantage of physical modelling is that physical modelling can be performed as a full-scale test of a given prototype while on a reduced scale. This solves the problems coming from full-scale field tests as well as the limitations of down-scaled laboratory tests. Nevertheless, in addition to the non-cheap centrifuge equipment, scaling laws and similitude conditions are the main concerns in centrifuge modelling, which still lack studies so far. In physical modelling, it is hard to produce a model that covers all details the same as the prototype. Especially for soils such granular materials, it is impossible to scale the grain size effects in a centrifuge model since it will imply a different friction angle and cohesion if the grain size is scaled. But still, Hoadley et al. (1981) discovered from their test on the laterally loaded piles that the particle size effect is not significant if a “model diameter/ grain size diameter” ratio of 50 and above.

Another modern geotechnical method is numerical modelling using finite element analysis through the implementation of soil constitutive models. In addition to academic research, various modelling platform has been developed to simulate soil response, soil-structure interaction, and foundation design project across many application fields such as offshore engineering. Numerical modelling is relatively cheap, quick, and flexible once the simulation platform has been established. It is free to build different structures as required, and it is very convenient to model various boundary and loading conditions which is typically suitable for dynamic analysis. Even though numerical simulations do not require physical resources, the computational cost and time can become significant with the increasing complexity of the constitutive model. The uncertainties originated from model parameter calibration could also be another factor that influences the accuracy of the numerical modellings.

Among the numerical simulation platforms, Plaxis 2D/3D is one of the most popular geotechnical finite element analysis software to date. The start of Plaxis dated back to 1987 at the Delft University of Technology (TUD) and gradually released Plaxis 2D and Plaxis 2D across the decades. Plaxis has

been widely applied in many fields: geotechnical engineering, offshore structures analysis, bridge analysis, hydraulics, etc. Unfortunately, due to the high development expenses, Plaxis is none open-source, and users should purchase a high amount of money to get the license. Hence, it is more suitable for companies, while for individual users, it is not cost-friendly.

Apart from Plaxis, there is an open-source geotechnical engineering software called OpenSees (Open System for Earthquake Engineering Simulation), which was launched in 1999 with the goal of simulating the structural and geotechnical systems' response under the influence of nature disasters (mainly earthquakes). OpenSees provides broad capabilities for modeling and investigating the nonlinear response of systems by utilizing a diverse set of material models, elements, and solution methods. Parallel computing was incorporated into the software to enable extensive simulations on high-end computers or parameter investigations.

Every method has its own pros and cons, the selection of research method depends on the scale and the complexity of tests or projects which are going to be performed. In this thesis, the OpenSees finite element analysis software will be used as the simulation platform. The constitutive model is SANISAND-MS which has 16 model parameters in total, among which three are newly added in accordance with memory surface. The calibration of model parameters is based on experimental data of Fontainebleau NE34 sand from research project SOLCYP (France). The pile installation process will not be included in this thesis.

## Chapter 3

# Constitutive Model and Parameter calibration

The SANISAND-MS constitutive model is developed from SANISAND-04, which is known as the two-surface plasticity model formed by describing soil behaviour using yield surface and bounding surface. Here in the new model, another memory surface is added to capture the cyclic ratcheting phenomenon, called the three-surface plasticity model.

### 3.1 Mathematical formulation of the model

The constitutive model has three surfaces in multi-axial space: yield surface, bounding surface and memory surface. For brevity's sake, the formulation for each surface is only provided with simple conceptual discussions. Further information can be found in relevant publications of Manzari & Dafalias (2004) and the papers of Liu *et al.* (2019). Aside from surfaces in multi-axial space, there are two more surfaces describing soil critical state and dilatancy in the multidimensional  $e - \sigma$  space, formulating the soil contractive and dilative behaviour.

#### 3.1.1 Soil elasticity

The yield surface is a boundary of elastic and plastic straining. It is defined that inside the yield locus, soil behaviour is supposed to be (hypo)elastic, with constant shear modulus and Poisson ratio. In soil mechanics, the elastic stress-strain relation of soils is described as:

$$de^e = ds/2G \quad (\text{Eq. 3-1})$$

$$d\varepsilon_v^e = dp/K \quad (\text{Eq. 3-2})$$

In this constitutive model, the shear modulus  $G$  is given by:

$$G = G_0 p_{atm} [(2.97 - e)^2 / (1 + e)] \sqrt{p/p_{atm}} \quad (\text{Eq. 3-3})$$

And the corresponding bulk modulus  $K$  can be obtained from following equation:

$$K = \frac{2G(1+\nu)}{3(1-2\nu)} \quad (\text{Eq. 3-4})$$

#### 3.1.2 Yield surface

In this model, it is suggested that plastic strains are developed due to variations in stress ratio  $r$ , read

as  $\mathbf{r} = \mathbf{s}/p$ , so that all plastic loci and hardening mechanisms can be effectively described in the normalized  $\pi$  plane (Figure 3-1). The yield locus is formed by the equation  $f=0$ , which is an open conical locus governed by the evolution of back-stress ratio  $\alpha$  and the yield locus opening parameter  $m$ :

$$f = \sqrt{(\mathbf{s} - p\boldsymbol{\alpha}) : (\mathbf{s} - p\boldsymbol{\alpha})} - \sqrt{2/3}mp = 0 \quad (\text{Eq. 3-5})$$

For  $\mathbf{r}$  inside the wedge, the elasticity strain occurs when  $d\mathbf{r} \neq 0$ . While the presence of plastic strain only happens when  $\mathbf{r}$  is at the yield surface and  $d\mathbf{r}$  is pointing ‘outward’ of the conical yield locus.

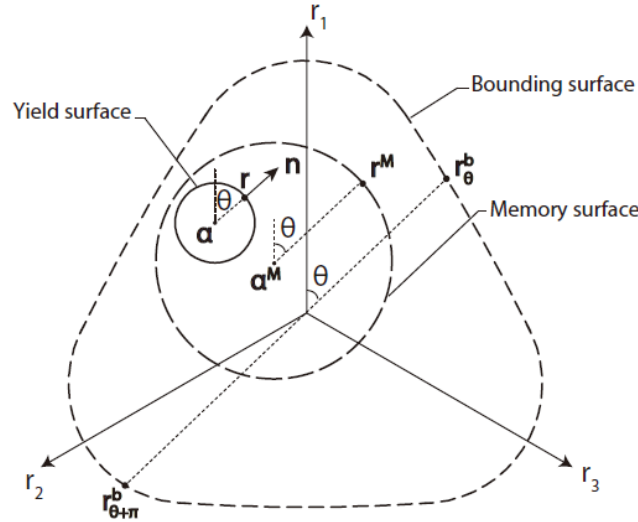


**Figure 3-1:** The yield, memory, and bounding surface in normalized  $\pi$  plane (Liu et al., 2019).

### 3.1.3 Critical state locus

As described in the literature review, the SANISAND constitutive model system is developed on the basis of the critical state framework. In this framework, critical stress ratio relation is given by  $M = q_c/p_c$ , at which stress state the soil reaches a critical point, the soil deforms continuously in shear at fixed stresses and zero volumetric strain rate. The critical state line on the  $e$ - $p$  plane is formulated as:

$$e_c = e_0 - \lambda_c(p_c/p_{atm})^\xi \quad (\text{Eq. 3-6})$$

Combined with the state parameter  $\Psi = e - e_c$  that gives the distance between current and critical void ratios, the sand behaviour at varying relative densities is realized in constitutive model. The projection of the critical state locus on the normalized  $\pi$  plane can be conveniently expressed as a deviatoric tensor,  $\mathbf{r}_\theta^c$ :

$$\mathbf{r}_\theta^c = \sqrt{2/3}g(\theta)M\mathbf{n} \quad (\text{Eq. 3-7})$$

In which the deviatoric tensor  $\mathbf{r}_\theta^c$  is the projection of critical state locus in the normalized  $\pi$  plane, with the superscript c refers to ‘critical’. The function  $g$  describes the Argyris-type shape of the critical locus depending on the ‘relative’ Lode angle  $\theta^1$ . Tensor  $\mathbf{n}$  is the unit tensor normal to the yield locus given by:

<sup>1</sup>  $\cos(3\theta) = \sqrt{6}tr\mathbf{n}^3$  (Manzari and Dafalias, 1997)

$$\mathbf{n} = (\mathbf{r} - \boldsymbol{\alpha}) / (\sqrt{2/3}m) \quad (\text{Eq. 3-8})$$

### 3.1.4 Flow rule

The flow rule describes the development of plastic strains. The plastic strain is classified in two parts: plastic volumetric strain and plastic deviatoric strain, for each of them the definition is read as:

$$d\varepsilon_v^p = \langle L \rangle D \quad (\text{Eq. 3-9})$$

$$d\mathbf{e}^p = \langle L \rangle \mathbf{R}' \quad (\text{Eq. 3-10})$$

For the dilatancy coefficient  $D$ , the mathematical expression in multi-axial space is given by:

$$D = A_0 \exp\left(\beta \frac{\langle \tilde{b}_d^M \rangle}{b_{ref}}\right) (\mathbf{r}_\theta^d - \mathbf{r}) : \mathbf{n} \quad (\text{Eq. 3-11})$$

Where  $\mathbf{r}_\theta^d$  is the projection of dilatancy locus in the normalized  $\pi$  plane:

$$\mathbf{r}_\theta^d = \sqrt{2/3}g(\theta)M \exp(n^d \Psi) \mathbf{n} \quad (\text{Eq. 3-12})$$

and  $(\mathbf{r}_\theta^d - \mathbf{r})$  is the distance between yield surface and dilatancy surface,  $\beta$  is a model constant and

$\tilde{b}_d^M$ , defined as  $\tilde{b}_d^M = (\tilde{\mathbf{r}}_\theta^d - \tilde{\mathbf{r}}^M) : \mathbf{n}$  is the distance between the memory and the dilatancy surface. In the definition of deviatoric plastic flow rule, the coefficient  $\mathbf{R}'$  is the tensor of deviatoric plastic flow, expressed as:

$$\mathbf{R}' = B\mathbf{n} - C \left[ \mathbf{n}^2 - \frac{I}{3} \right] \quad (\text{Eq. 3-13})$$

In which  $B$ ,  $C$  are functions of critical state parameter  $c$  and Lode angle  $\theta$ , parameter  $I$  is the second-order identity tensor.

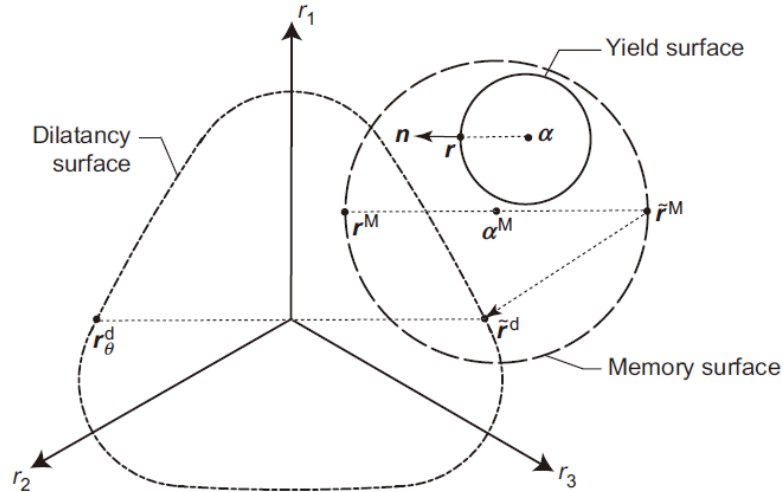


Figure 3-2: Distance definition for dilatancy coefficient (Liu et al., 2019).

### 3.1.2 Kinematic hardening and Bounding surface

The evolution of the yield surface only shows the surface translation to various locations, bounded by the bounding surface, but no changes in the surface's size (constant parameter  $m$ ). The mathematical expression is given by the changes in the back-stress ratio tensor:

$$d\boldsymbol{\alpha} = \frac{2}{3} \langle L \rangle h (\mathbf{r}_\theta^b - \mathbf{r}) \quad (\text{Eq. 3-14})$$

According to Eq.3-14, the center of the yield locus translates in the  $\pi$  plane along the  $(\mathbf{r}_\theta^b - \mathbf{r})$  direction. In the normalized  $\pi$  plane, the projection of bounding surface is expressed as a deviatoric tensor,  $\mathbf{r}_\theta^b$  (the super script represents bounding):

$$\mathbf{r}_\theta^b = \sqrt{2/3} g(\theta) M \exp(-n^b \Psi) \mathbf{n} \quad (\text{Eq. 3-15})$$

Parameter  $h$  in Eq.3-14 is the hardening factor which controls the magnitude of yield surface translation. Through adding the memory surface, the hardening parameter  $h$  is given by:

$$h = \frac{b_0}{(\mathbf{r} - \mathbf{r}_{in}) : \mathbf{n}} \exp \left( \mu_0 \left( \frac{p}{p_{atm}} \right)^{1/2} \left( \frac{b^M}{b_{ref}} \right)^2 \right) \quad (\text{Eq. 3-16})$$

$L$  is plastic multiplier which can be expressed in the following form:

$$L = \frac{1}{K_p} \frac{\partial f}{\partial \boldsymbol{\sigma}} : d\boldsymbol{\sigma} \quad (\text{Eq. 3-17})$$

The response of the sand is determined by the value of plastic modulus:

$$K_p = \frac{2}{3} p h (\mathbf{r}_\theta^b - \mathbf{r}) : \mathbf{n} \quad (\text{Eq. 3-18})$$

### 3.1.3 Memory surface

In the SANISAND-MS model, changes in soil granular fabric are distinguished by the memory surface. In multi-axial space, the memory locus  $f^M = 0$  is represented by another conical surface:

$$f^M = \sqrt{(\mathbf{s} - p\boldsymbol{\alpha}^M) : (\mathbf{s} - p\boldsymbol{\alpha}^M)} - \sqrt{2/3} m^M p = 0 \quad (\text{Eq. 3-19})$$

The changes of soil fabric are captured through the expansion and the translation of the memory surface.

#### Change of memory surface size

The expansion of memory surface is realized by increasing the value of parameter  $m^M$ . The increment of  $m^M$  is expressed as:

$$dm^M = \sqrt{\frac{3}{2}} d\boldsymbol{\alpha}^M : \mathbf{n} - \frac{m^M}{\zeta} f_{shr} \langle -d\varepsilon_{vol}^p \rangle \quad (\text{Eq. 3-20})$$

The increasing size (memory enhanced) of the memory surface is driven by an anisotropic hardening mechanism, which will lead to gradual fabric change and sand stiffening. However, when there is a dilative deformation in the sand, the void ratio will increase, and the sand will become softer, which results in a shrinkage of the memory surface. This is called a memory loss and is realized by adding another term (second term on the right-hand side of Eq.3-20), allowing the memory surface shrinkage only during the dilation stage (negative  $d\varepsilon_{vol}$ ).

#### Memory surface translation

As mentioned, the memory surface is changing loci size (varying parameter  $m^M$ ) as the soil stress

state develops. Similar to yield locus translation, the memory surface translation considers the memory back-stress ratio tensor  $d\alpha^M$ , but the center of the memory surface is assumed to translate along the direction of  $(\mathbf{r}^b - \mathbf{r}^M)$  :

$$d\alpha^M = \frac{2}{3} \langle L^M \rangle h^M (\mathbf{r}^b - \mathbf{r}^M) \quad (\text{Eq. 3-20})$$

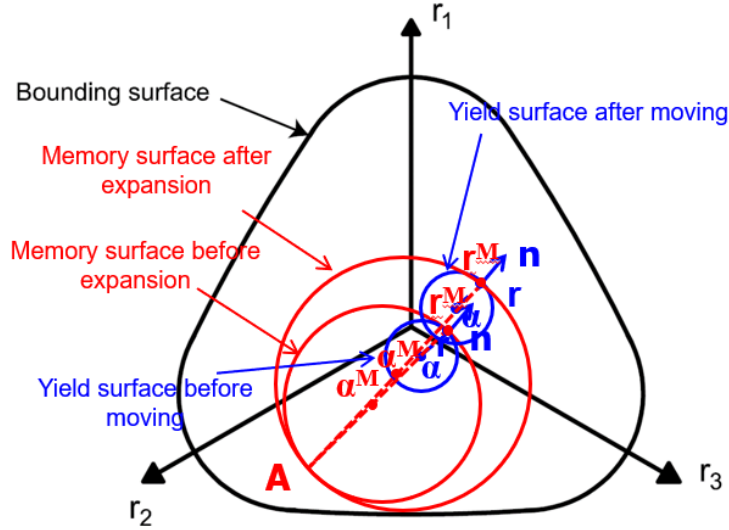


**Figure 3-3:** Evolution of the yield surface and the memory surface (Liu et al., 2019).

## 3.2 Calibration of model parameters

The new model has 16 model parameters in total, in which 3 of them are related to the added memory surface ( $\mu_0$ ,  $\zeta$  and  $\beta$ ). Other 13 parameters are coming from the original SANISAND model, representing soil elasticity, critical state, yield surface, plastic modulus, and soil dilatancy, respectively. In table 3-1, all the parameters are summarized:

**Table 3-1:** SANISAND-MS model parameters classification

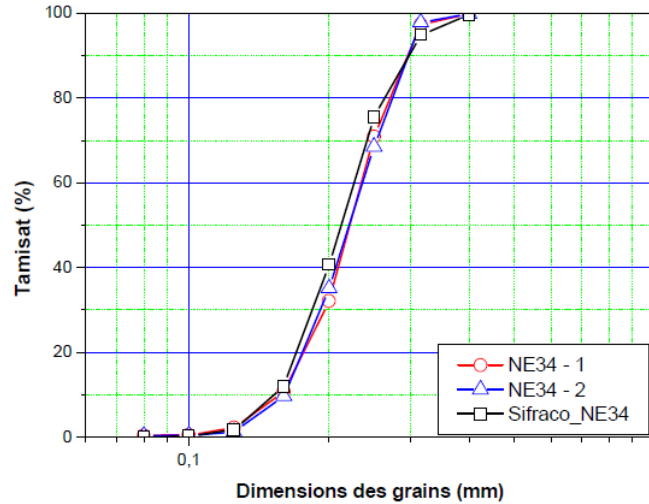
Elasticity		Critical state					Yield surface	Plastic modulus			Dilatancy		Memory surface		
$G_0$	$\nu$	$M$	$c$	$\lambda_c$	$e_0$	$\xi$	$m$	$h_0$	$c_h$	$n^b$	$A_0$	$n^d$	$\mu_0$	$\zeta$	$\beta$

The calibration is divided into two parts, considering the monotonic performance and the cyclic performance of the model separately. The sand used in this calibration is Fontainebleau NE34 Sand which, for the sake of consistency, has the same index properties as the Fontainebleau sand used in the paper Tsuha et al. (2012). Both of the two calibration parts are based on experimental results from PROJET DE RECHERCHE SOLCYP (ANR + PN) (July 2008-June 2012).

The sand of Fontainebleau NE34 is a poorly graded silica sand according to the LPC/UCS classification. The characteristics of this sand are summarized in Table 3-2. Its grain size distribution curve established according to the NFP94-056 standard and presented in Figure 3-4 shows that it is uniform fine sand.

**Table 3-2: Mineralogy and index properties of Fontainebleau NE34 sand**

Grain angularity	SiO <sub>2</sub> (%)	d <sub>10</sub> (mm)	d <sub>50</sub> (mm)	d <sub>60</sub> (mm)	ρ <sub>s</sub> (g/cm <sup>3</sup> )	Coefficient of Non-Uniformity C <sub>u</sub>	e <sub>min</sub>	e <sub>max</sub>
Sub-angular	99.7	0.15	0.21	0.23	2.65	1.49	0.510	0.882


**Figure 3-4: Gradation curve of Fontainebleau NE34 sand.**

### 3.2.1 Calibration of monotonic parameters

The calibration was based on drained triaxial compression tests done on loose, medium dense and dense Fontainebleau sand under three different confining pressures: 50kPa, 100kPa, 200kPa. After this calibration work, the set of parameters were chosen to be as stated in the below table.

**Table 3-3: Monotonic model parameters**

Categories	Parameter	Physical meaning	Value
Elasticity	G <sub>0</sub>	Dimensionless shear modulus	120
	ν	Poison ratio	0.05
Critical state	M	Critical stress ratio	1.2
	c	Compression-to-extension strength ratio	0.71
	λ <sub>c</sub>	Slope of the critical state line in e - p plane	0.059
	e <sub>0</sub>	Reference critical void ratio	0.83
	ξ	Exponent of the critical state line in e - p plane	0.2
Yield surface	m	Yield locus opening parameter	0.01
Plastic modulus	h <sub>0</sub>	Hardening parameter	5.95
	c <sub>h</sub>	Hardening parameter	1.05
	n <sup>b</sup>	Void ratio dependence parameter	2.1
Dilatancy	A <sub>0</sub>	'intrinsic' dilatancy parameter	0.37
	n <sup>d</sup>	Void ratio dependence parameter	3.8

The critical state ratio M was estimated through final friction angle  $\varphi'$  (Eq. 24). The reference critical void ratio was set within the range ( $e_{\max} \pm 10\%$ ), i.e. (0.7938, 0.9702). In SANISAND

framework, Poisson ratio should not be too large to get better performance in drained conditions. Other parameters were determined by fitting strength and volumetric strain trends at ultimate conditions for various void ratios and stress levels.

$$\sin\phi' = \frac{3M}{6+M} \quad (\text{Eq. 3-21})$$

Calibration results were reported below.

### 3.2.1.1 Monotonic model performance

#### 3.2.1.1.1 Testing conditions

**Table 3-4:** Monotonic test scenarios

	Test code	$e_i$	$\rho_d$ (g/cm <sup>3</sup> )	$I_d$	$P_{in}'$ (kPa)
loose	TM1	0.718	1.537	0.44	50
	TM2	0.712	1.542	0.46	100
	TM3	0.702	1.551	0.48	200
Medium dense	TM4	0.637	1.613	0.66	50
	TM5	0.637	1.613	0.66	100
	TM6	0.638	1.612	0.66	200
dense	TM7	0.573	1.679	0.83	50
	TM8	0.579	1.672	0.81	100
	TM9	0.573	1.679	0.83	200

#### 3.2.1.1.2 Calibration results

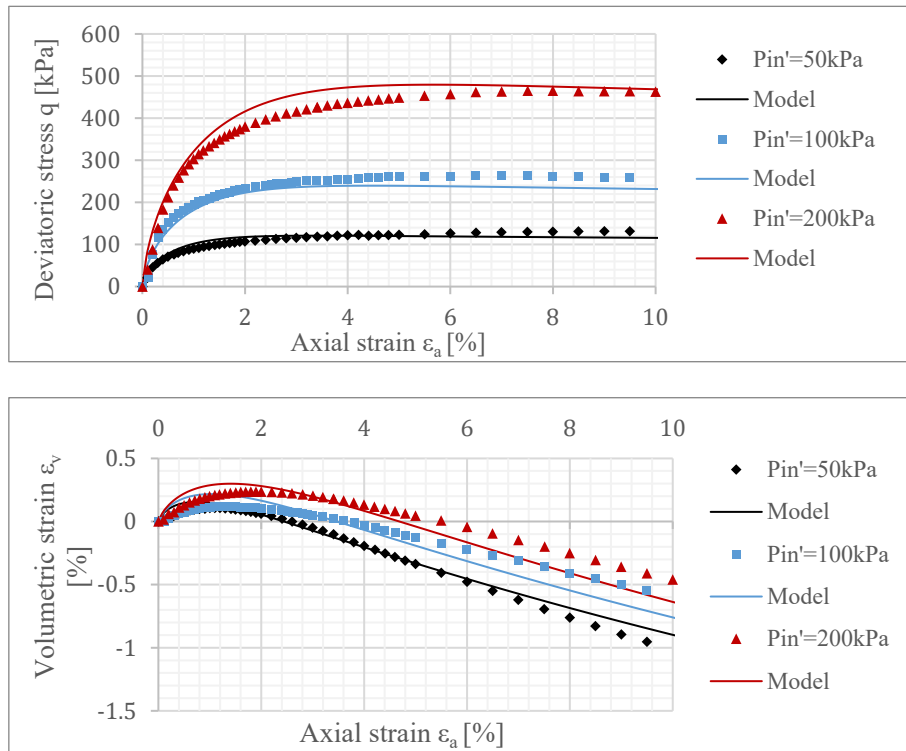


**Figure 3-5:** Calibration results of loose Fontainebleau sand against monotonic drained triaxial test, initial void ratio  $e_i = 0.702-0.718$ .

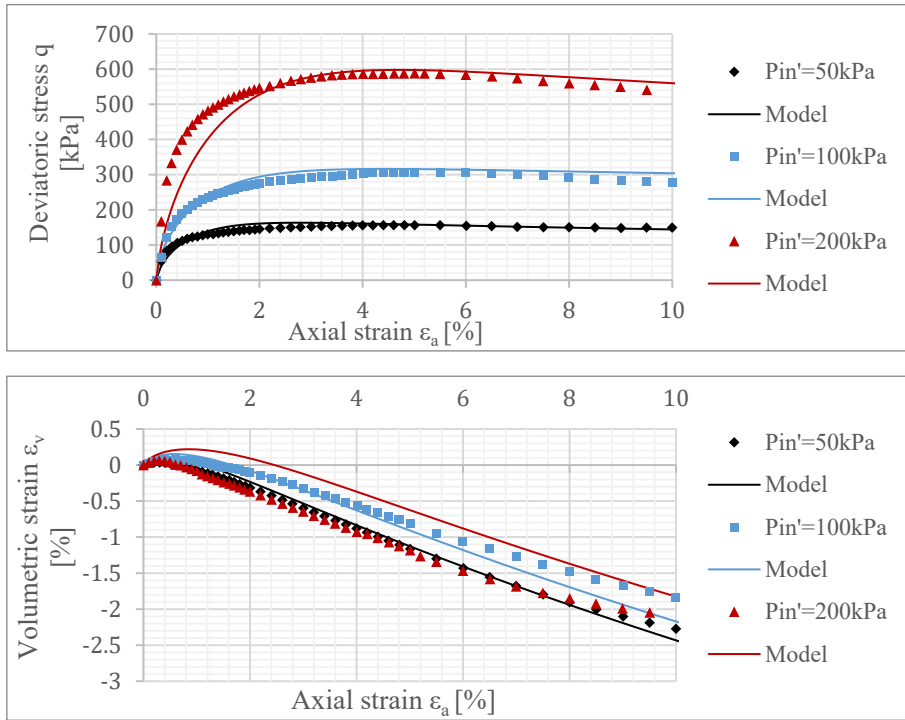


**Figure 3-6:** Calibration results of medium dense Fontainebleau sand against monotonic drained triaxial test, initial void ratio  $e_i=0.637-0.638$ .

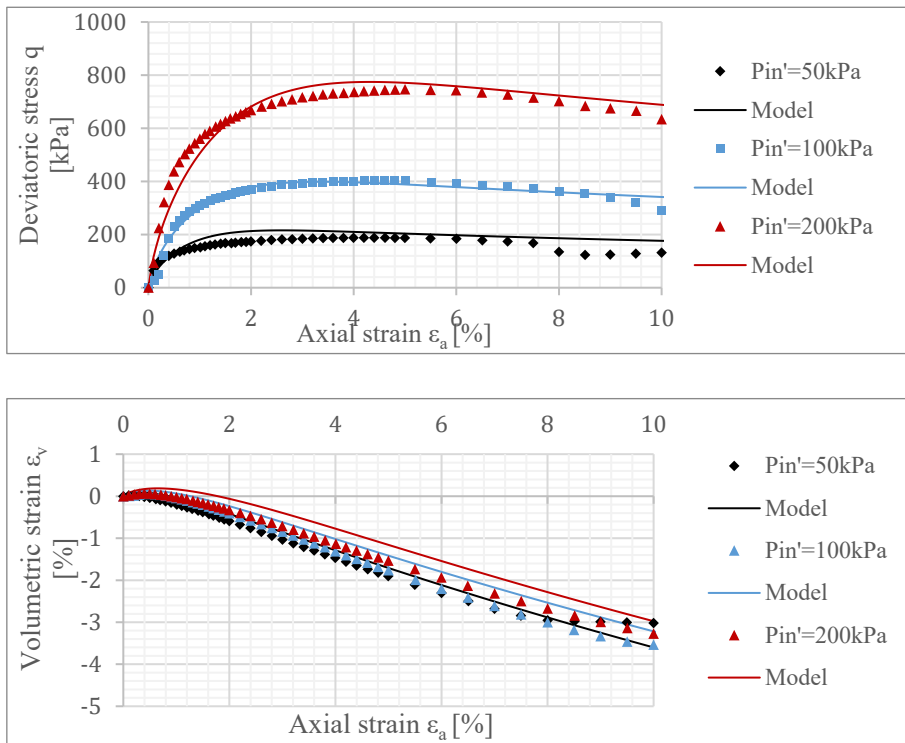


**Figure 3-7:** Calibration results of dense Fontainebleau sand against monotonic drained triaxial test, initial void ratio  $e_i=0.573-0.579$ .

### 3.2.1.1.3 Discussion of the calibration

It is preferred to calibrate model parameters from actual laboratory tests because the parameter set could reflect real physical characteristics of the material, such as the granular properties. However, based on the limited laboratory data, this is a trial-and-error calibration through fitting data to laboratory curves. Only one parameter, the critical state ratio  $M$  were calculated from the laboratory results, some of the parameters were made to be reasonable, and others were estimated through trials. Studies have observed that  $A_d$  should be larger to obtain a better performance in the drained conditions. This is also why the unrealistic value of Poisson's ratio ( $\nu=0.05$ ) was chosen, which the real value of Poisson's ratio of sand is around 0.2. Things to notice that those choices of  $A_d$  and  $\nu$  value will underpredict the volumetric strain in drained conditions.

Good agreement between the experimental data and the numerical simulations in terms of deviatoric stress vs. axial strain was achieved for all samples. The model underpredicts the volumetric strain of loose sand with the increasing initial confining pressures. The volumetric strain vs. axial strain relations matches well for dense sand under all three initial confining pressures, despite slight over predictions under high  $P_{in}$ . At the same time, discrepancies of strain-strain relations appear in medium dense sand and are more apparent with higher initial confining pressures.

## 3.2.2 Calibration of cyclic parameters

This report aims at calibrating the remaining three parameters related to the new memory surface:  $\mu_0$ ,  $\zeta$  and  $\beta$ . The calibration was based on the data from undrained triaxial compression tests performed on loose and medium dense Fontainebleau sand, both under symmetric and asymmetric loading.

To make it convenient for the later FEM modelling work, it is better to have one set of parameters that is more feasible to assign values to each finite element. In his report, the optimized cyclic parameters, together with the monotonic parameters, will be given in Table 3-5.

**Table 3-5:** *Cyclic model parameters*

Categories	Parameter	Physical meaning	Value
Memory surface	$\mu_0$	Ratcheting parameter	34
	$\zeta$	Memory surface shrinkage parameter	0.00001
	$\beta$	Dilatancy memory parameter	8

Calibration results and corresponding analysis were reported below.

### 3.2.2.1 Cyclic model performance of symmetric loading

#### 3.2.2.1.1 Sand states and testing conditions

**Table 3-6:** symmetric test scenarios

	Test code	$e_i$	$I_d$	$p_c'$ (kPa)	$q_c$ (kPa)	$q_{cyc}$ (kPa)
loose	TCS1	0.72	0.44	200	0	72
	TCS2	0.72	0.44	200	0	48
	TCS3	0.72	0.44	200	0	35
Medium dense	TCS4	0.64	0.65	200	0	100
	TCS5	0.64	0.65	200	0	55
	TCS6	0.64	0.65	200	0	40

#### 3.2.2.1.2 Calibration results

The model performances of symmetric loading are illustrated below in Figure 3-8 to Figure 3-13.

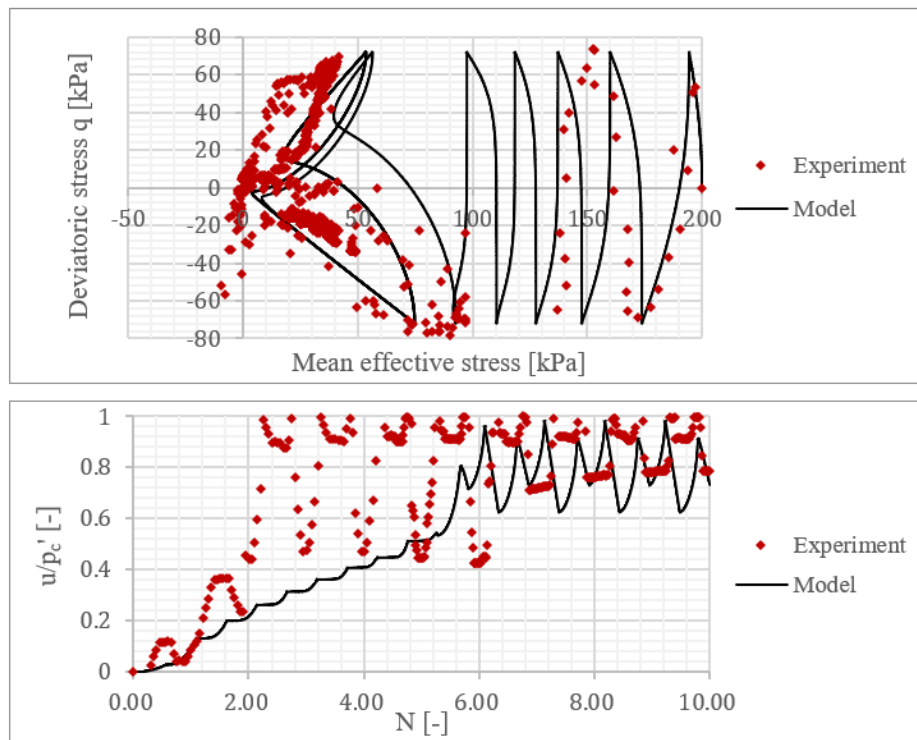


**Figure 3-8:** Model performances of loose Fontainebleau sand under symmetric undrained loading (TCS1),  $q_{cyc} = 72\text{kPa}$ .

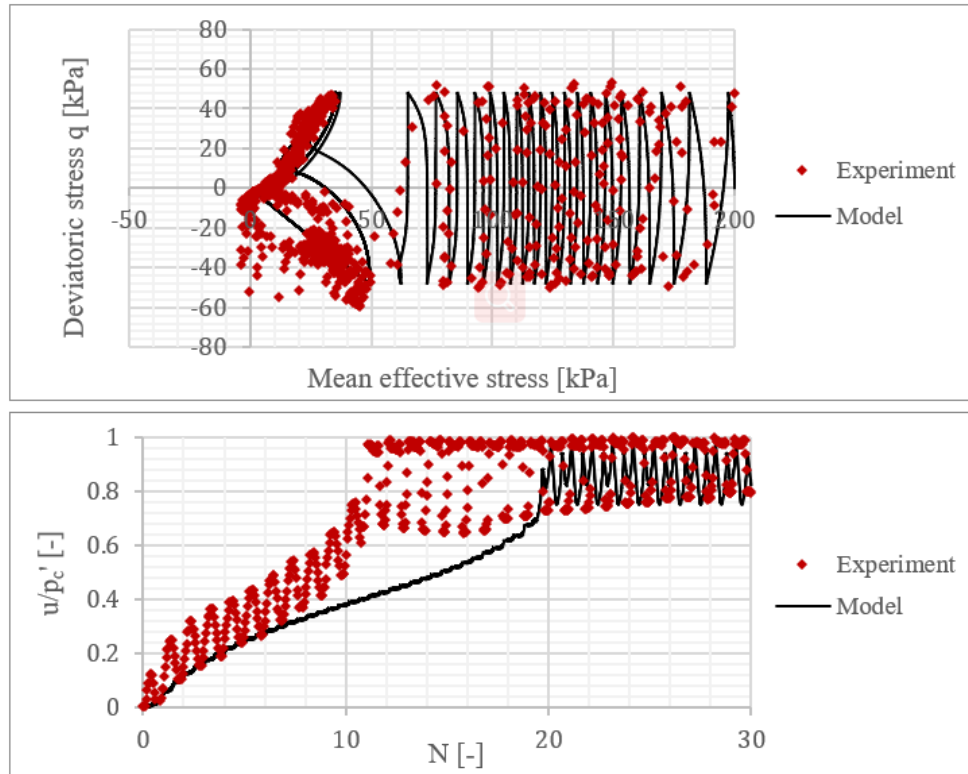


**Figure 3-9:** Model performances of loose Fontainebleau sand under symmetric undrained loading (TCS2),  $q_{cyc} = 48kPa$ .

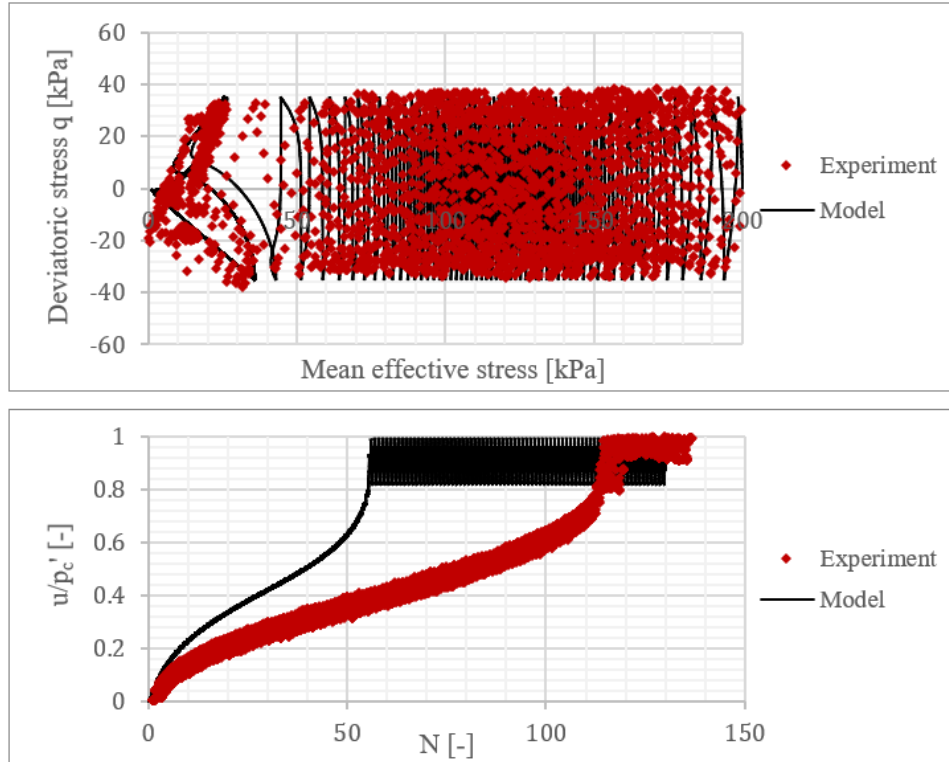


**Figure 3-10:** Model performances of loose Fontainebleau sand under symmetric undrained loading (TCS3),  $q_{cyc} = 35kPa$ .

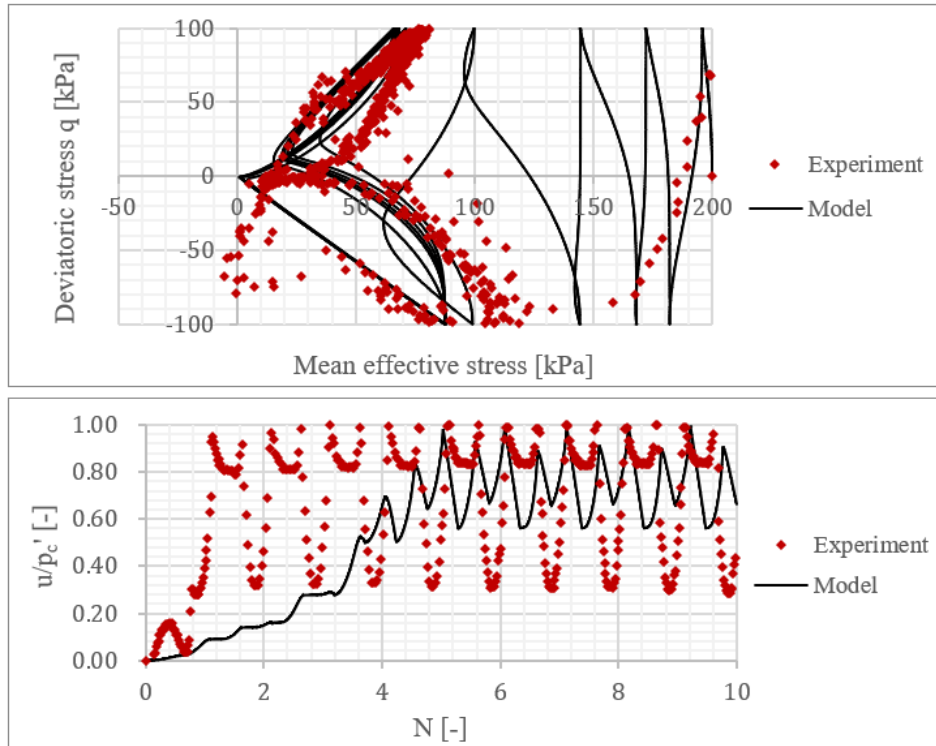


**Figure 3-11:** Model performances of medium dense Fontainebleau sand under symmetric undrained loading (TCS4),  $q_{cyc} = 100kPa$ .

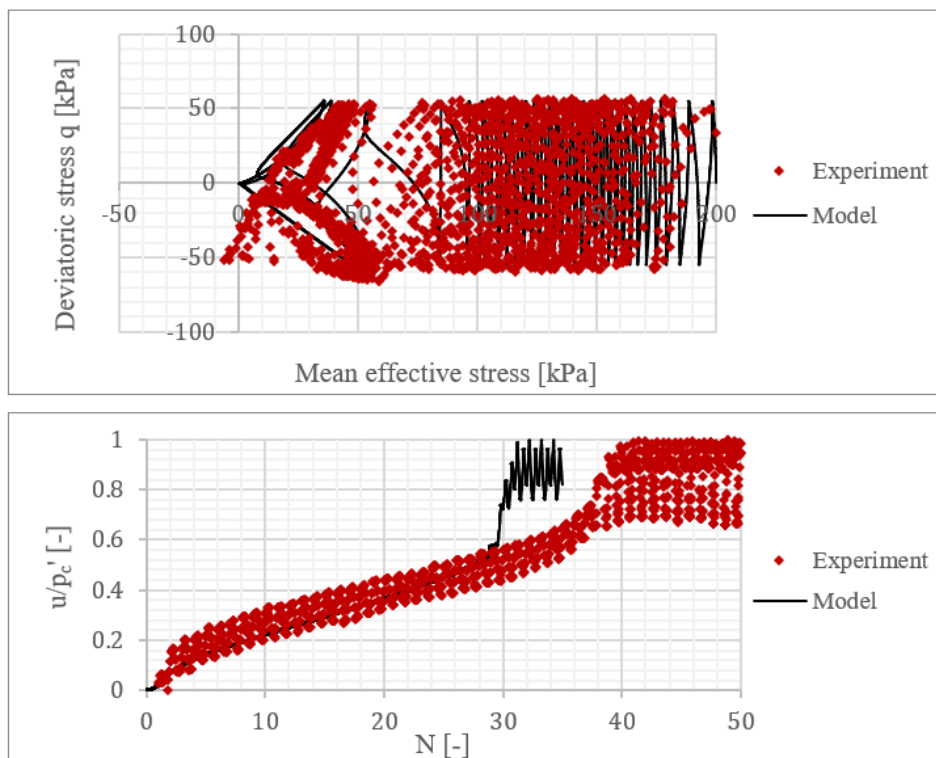


**Figure 3-12:** Model performances of medium dense Fontainebleau sand under symmetric undrained loading (TCS5),  $q_{cyc} = 50kPa$ .

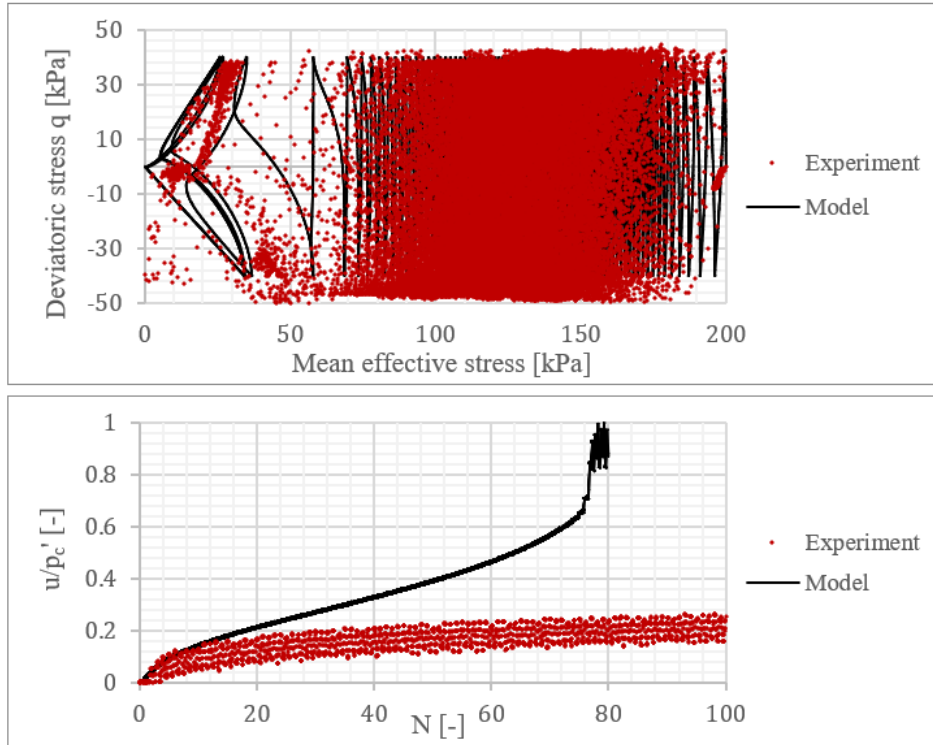


**Figure 3-13:** Model performances of medium dense Fontainebleau sand under symmetric undrained loading (TCS6),  $q_{cyc} = 40\text{kPa}$ .

### 3.2.2.1.3 Discussions

The model is able to capture a “butterfly-shaped” stress path for both loose and medium dense sand with the minimum simulated mean effective stress equals zero, i.e., the value of ratio  $u/p_c'$  can reach 1 after a certain number of loading cycles.

Loading conditions and the corresponding number of cycles to trigger liquefaction are re-summarized in Table 3-7, with cyclic stress ratio  $\eta^{amp} = q_{cyc} / p_c'$  and  $N_{Liq}$  refers to experimental results of number of cycles to liquefaction. It is obvious from experimental results that more cycles are required to trigger liquefaction (higher  $N_{Liq}$ ) at low  $\eta^{amp}$ . This tendency was also observed in the simulation results ( $N_{Liq\_Sim}$ ). Nevertheless, there are discrepancies regarding the number of cycles to liquefaction, and this tendency becomes more distinctive at lower  $\eta^{amp}$ . The influence of cyclic stress ratio on the evolutions of excess pore water pressure was depicted in Figure 3-14 and Figure 3-15.

**Table 3-7:** Summary of results from symmetric test

	Test code	$e_i$	$\eta^{amp}$	$N_{Liq}$	$N_{Liq\_Sim}$
loose	TCS1	0.72	0.36	3	6
	TCS2	0.72	0.24	12	20
	TCS3	0.72	0.175	112	55
Medium dense	TCS4	0.64	0.5	3	5
	TCS5	0.64	0.275	43	32
	TCS6	0.64	0.2	1165	79

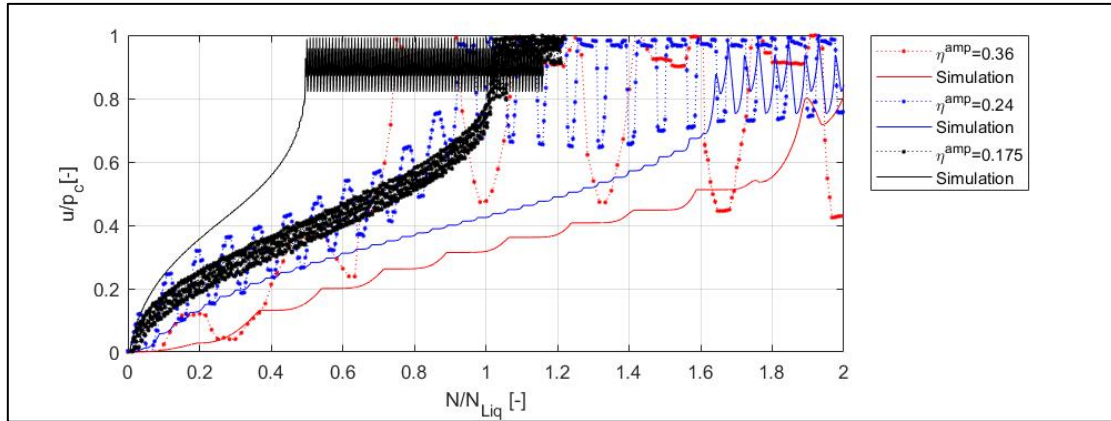


**Figure 3-14:** Model performances of loose Fontainebleau sand under various cyclic stress ratio  $\eta^{amp}$ . Test conditions:  $e_{in}=0.72$ ,  $p_c'=200kPa$ .

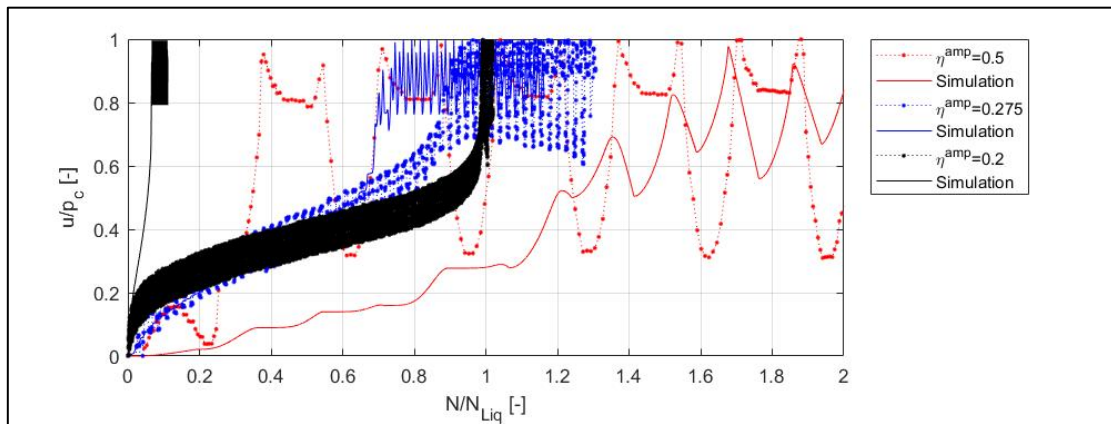


**Figure 3-15:** Model performances of medium dense Fontainebleau sand under various cyclic stress ratio  $\eta^{amp}$ . Test conditions:  $e_{in}=0.64$ ,  $p_c'=200kPa$ .

### 3.2.2.2 Cyclic model performance of asymmetric loading

#### 3.2.2.2.1 Sand states and testing conditions

The experimental data used here was shown in Table 2-8, with only one-way cyclic loading, i.e.,  $\eta^{amp} < \eta^{ave}$ .

**Table 3-8:** Asymmetric test scenarios

	Test code	$e_i$	$I_d$	$p_c'$ (kPa)	$q_c$ (kPa)	$q_{cyc}$ (kPa)	$\eta^{amp}$	$\eta^{ave}$
loose	TCA1	0.72	0.44	200	200	50	0.187	0.75
	TCA2	0.72	0.44	267	200	80	0.300	0.75
Medium dense	TCA3	0.64	0.65	267	200	80	0.300	0.75
	TCA4	0.64	0.65	267	200	100	0.375	0.75

#### 3.2.2.2.2 Calibration results

It is observed that this version of the program is not good at simulating the asymmetric loading conditions. Hence, the calibration work stops when the simulation result could produce a steady loop of stress-strain relationship. The results are shown below in Figure 3-16 and Figure 3-17.

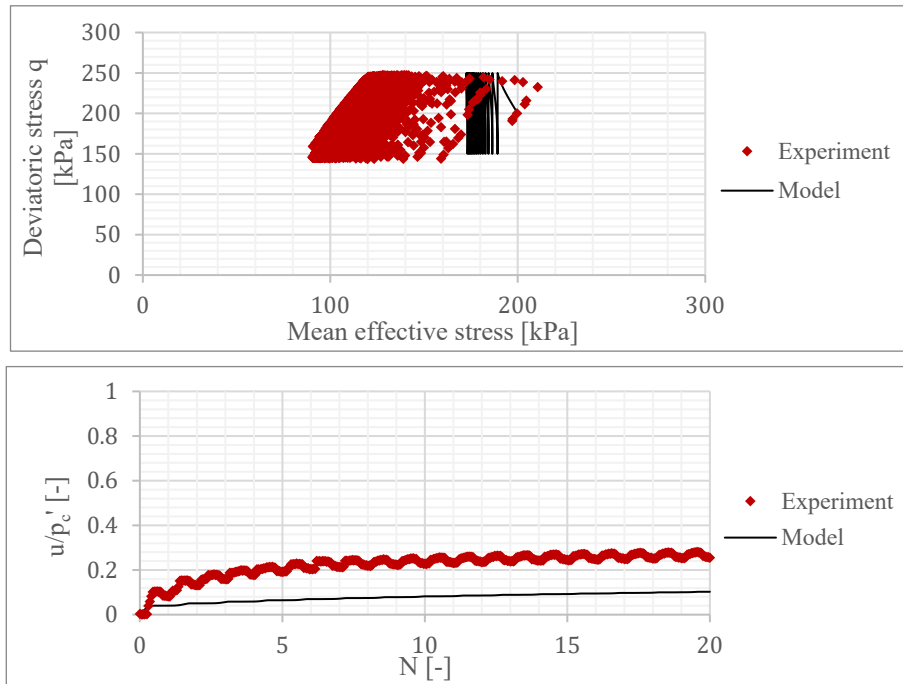


**Figure 3-16:** Model performances of loose Fontainebleau sand under asymmetric undrained loading (TCA1),  $q_c = 200\text{kPa}$ ,  $q_{cyc} = 50\text{kPa}$ .

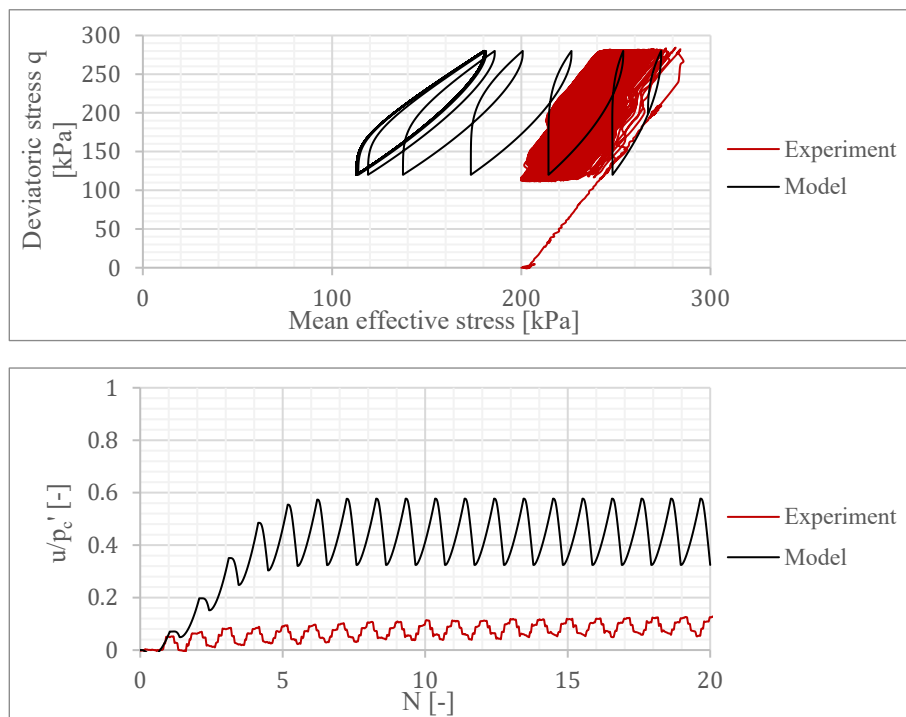


**Figure 3-17:** Model performances of medium dense Fontainebleau sand under asymmetric undrained loading (TCA3),  $q_c = 200\text{kPa}$ ,  $q_{cyc} = 80\text{kPa}$ .

### 3.2.2.2.3 Discussions

The version of the model does not include the pre-shearing effect, and it is not suitable for the simulation of asymmetric one-way conditions. The simulation stops at a larger number of loading cycles, and only 2 cycles could be reproduced for TCA2 & TCA4.



The Mini-ICP piles are closed-ended stainless steel piles with a 36mm outer diameter. The piles comprise Leading, Following, and Trailing instrument clusters with varying vertical locations and have a 60° conical tip, as shown in Figure 4-2. Each cluster contains a very stiff surface stress transducer (SST) which could measure the total radial stress ( $\sigma_r$ ) and the shear stress ( $\tau_{rz}$ ) at the pile surface. The Mini-ICP piles are installed through jacket cycles into a fresh prepared sand-filled chamber into an embedded length equals to 1 meter, see Figure 4-1. The chamber is 1.5m high and 1.2m in internal diameter with a rigid base and top. There is an upper membrane that applies vertical compressive stress around -150kPa to the sand surface.

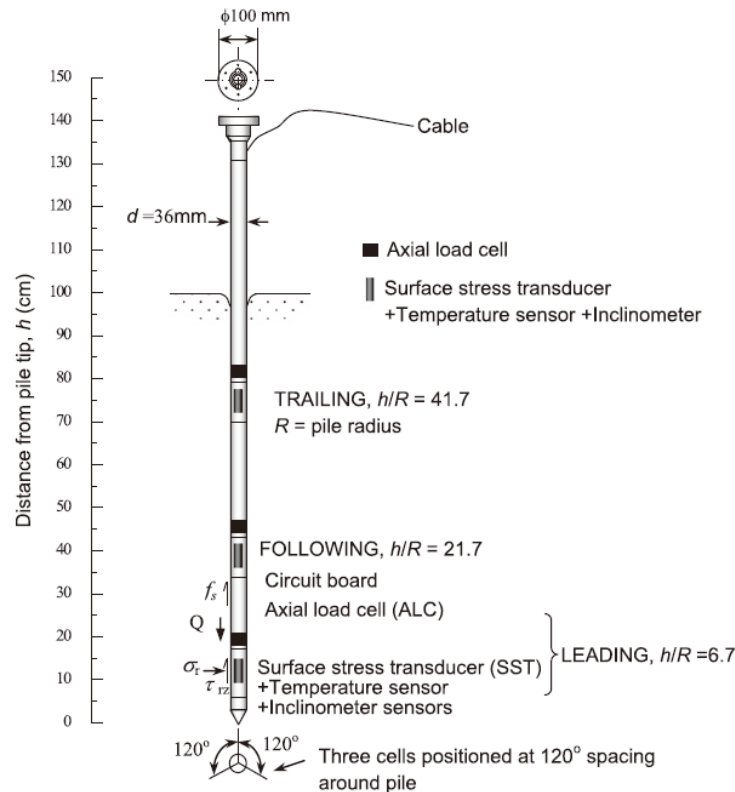


**Figure 4-2:** Typical Mini-ICP setting (Tsuha et al. 2012).

## 4.2 Finite Element Model Dimension

### 4.2.1 General model dimension

The model to be established here, based on information in Figure 4-2, is a  $1.2m \times 1.2m \times 1.5m$  reduced-scale domain filled with Fontainebleau NE34 sand. The bottom and the side boundaries of the sand domain are fixed, meaning no displacements at all boundaries. The close-ended stainless-steel pile is 1.4m long in total, of which 1m is embedded into the centre of the soil. The external diameter of the pile is 36mm. Worth mentioning that there is a uniform compressive vertical load  $\sigma_{v0}' = -150kPa$  at the surface of the soil domain, aiming at creating a stress condition under 10-15m deep soil. The model's geometrical setting is illustrated in Figure 4-3.

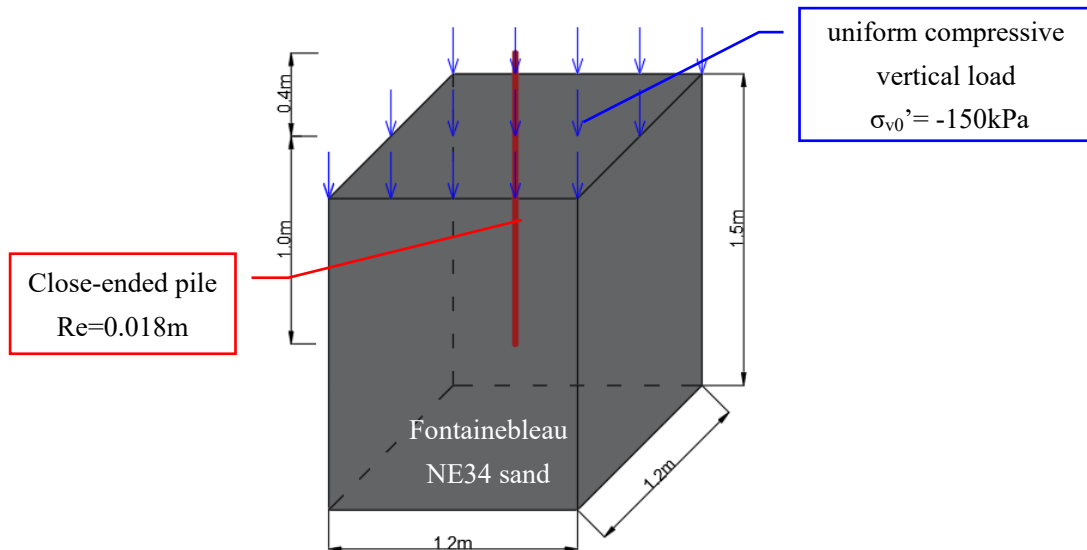


**Figure 4-3:** Geometrical settings of the Finite Element model.

For the sake of efficiency, only the quarter domain is modelled in this thesis. All the cyclic loads are divided by a quarter, correspondingly. There are two main materials in this model to be defined: Fontainebleau NE34 sand and the close-ended stainless-steel pile. However, another soil layer is added as an interface layer between pile and sand to model the sand-pile interfacing zone in real cases. The characteristic of the interface layer is that it is less stiff than normal Fontainebleau NE34 sand, which behaves like a bridge when the model is subjected to cyclic loadings. In the finite element model, this stiffness reduction is achieved by applying smaller stiffness parameters of the constitutive model to the interface layer. The thickness of the interface layer is selected to be 7 millimetres (0.007m) in this simulation. The initial sand state properties are given in Table 4-1, and the detailed pile information is shown in Table 4-2.

**Table 4-1:** Initial sand state properties

Sand	$\rho_s$ (g/cm <sup>3</sup> )	$e_{init}$ (-)	$e_{max}$ (-)	$e_{min}$ (-)	Dr (%)
Fontainebleau NE34	1.605	0.620	0.620	0.620	72

**Table 4-2:** Pile information

Pile type	Material	Pile mass density $\rho_{pile}$ (g/cm <sup>3</sup> )	External diameter $R_e$ (m)	Interface length $I_L$ (m)
Close-ended	Stainless-steel	7.85	0.018	0.007

The final FE model is depicted in the Figure 4-9 below.

## 4.2.2 Verification of the model size

This is a pile under axial loading, it is desirable to check whether the boundary is too close or not. For this purpose, the model was tested under one of the extreme loading conditions (see Table 5-1, ICP3-OW1) when the relative density  $D_r$ , strain, and displacement magnitudes at the end of cyclic loading over the whole soil domain were recorded. The obtained data was visualized in the software ParaView to see whether the top and bottom boundaries were affected by the cyclic loadings.

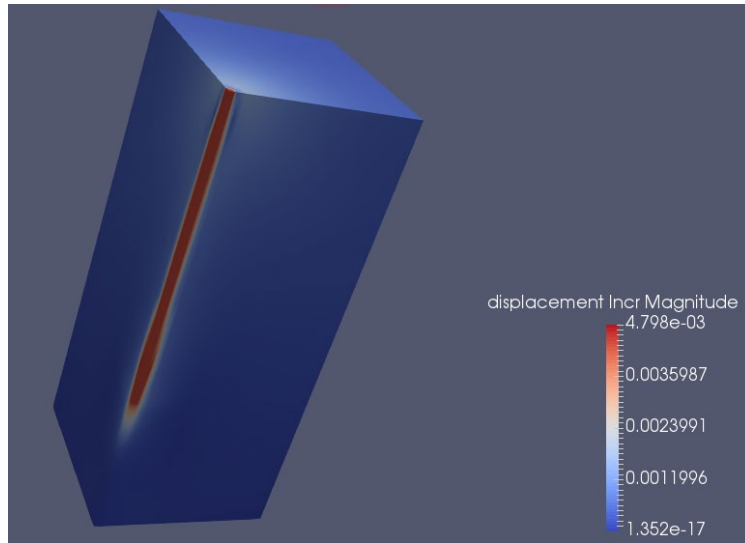


**Figure 4-4:** Displacement increments after unstable cyclic loading.

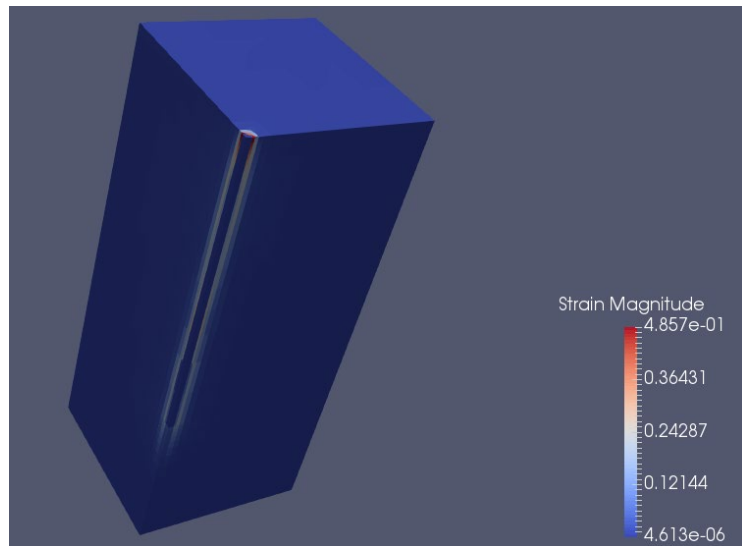


**Figure 4-5:** Strain magnitude after unstable cyclic loading.

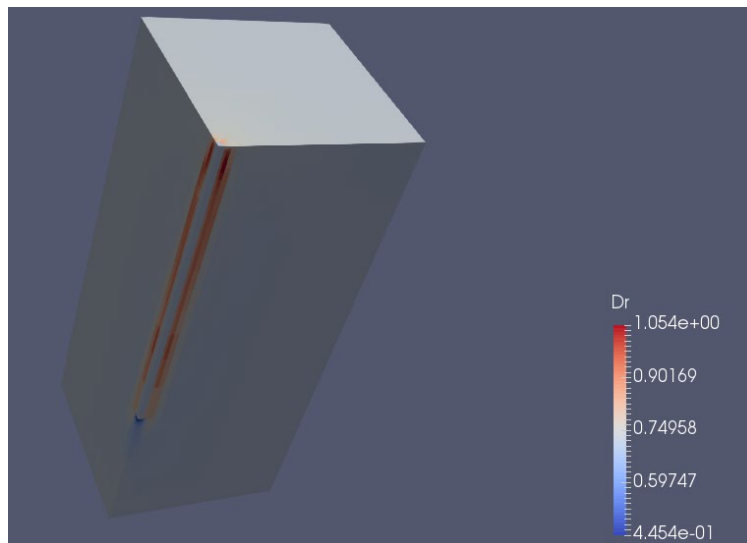


**Figure 4-6:** Relative density  $D_r$  after unstable cyclic loading.

From Figure 4-4 to Figure 4-6, the displacement increment, strain, and relative density  $D_r$  change only concentrate on a limit area close to pile shaft. The boundary soil far from the pile was not affected by the cyclic loading and stayed at original values. Hence, the model size pre-described in Figure 4-3 is wide and deep enough in this simulation.

### 4.3 Finite Element Mesh

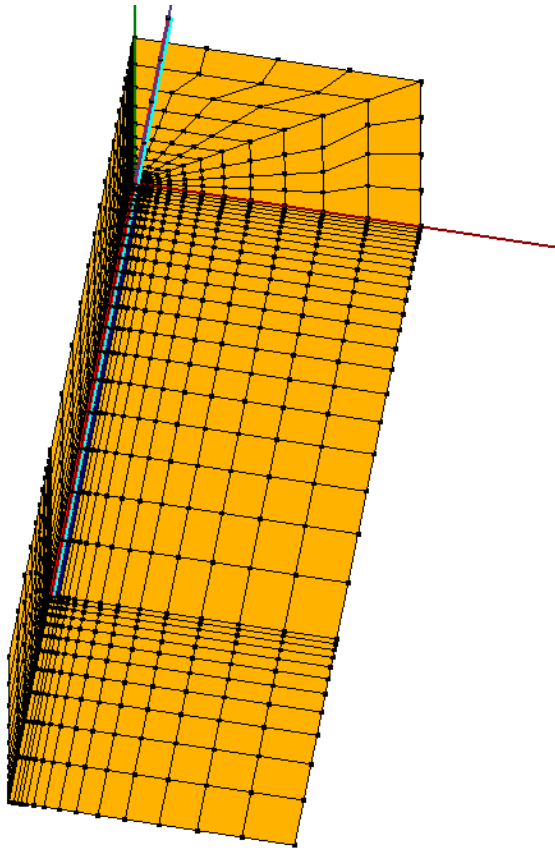
The pile is modelled as an elastic 3D volume pile. Both pile and soil elements are 8-node, one-phase SSP Brick elements. In this section, the sensitivity of the FE modelling results to the model space discretization is analyzed. The finite element result is sensitive to the meshing of the FE model; therefore, four types of mesh discretization method is proposed here. After the comparison of the accumulated displacement curves obtained from the four models, the optimal meshing scheme is selected as the final FE model that is going to be used in this report.

Figure 4-7, Figure 4-8, Figure 4-9, and Figure 4-10 give the 4 proposed meshing schemes, respectively. The detailed meshing information of the 4 models are summarized in Table 4-3.

**Table 4-3:** Details of different mesh discretization schemes

		<b>Dense1</b>	<b>Dense2</b>	<b>Medium</b>	<b>Loose</b>
<b>Total number of soil elements</b>		3564	3960	2673	1890
<b>Horizontal Meshing</b>		13	16	13	10
<b>Vertical Meshing</b>	<b>Above pile tip</b>	22	25	22	20
	<b>Below pile tip</b>	11	15	11	10
<b>Number of slices in circumferential direction</b>		32	24	24	24

Dense2, Medium, and Loose mesh schemes have the same number of slices in the circumferential direction, but the mesh densities decrease both in the horizontal and vertical direction from denser to looser. Dense1 meshing scheme is the same as the Medium meshing scheme in horizontal and vertical directions but with a denser discretization in the circumferential direction.



**Figure 4-7:** Dense1 Meshing scheme

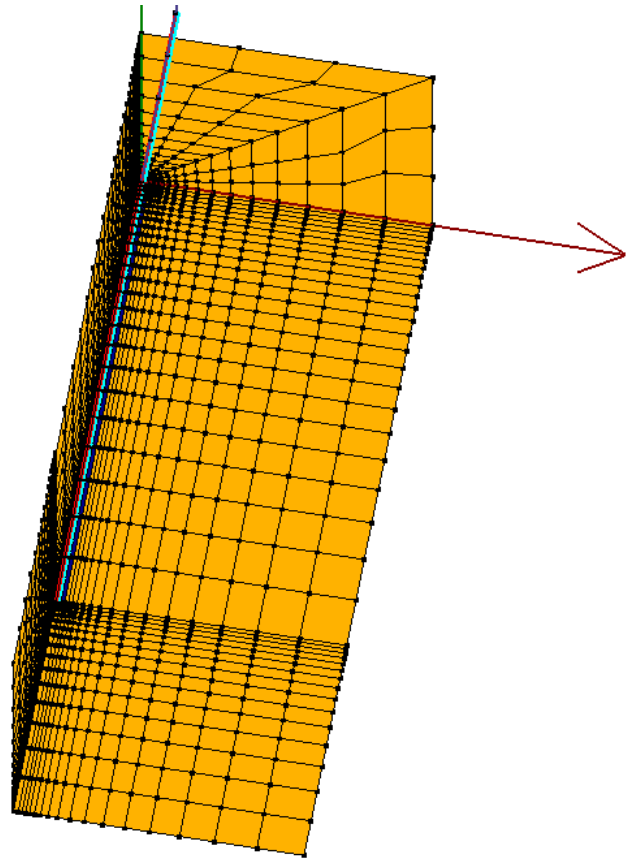


**Figure 4-8:** Dense2 Meshing scheme

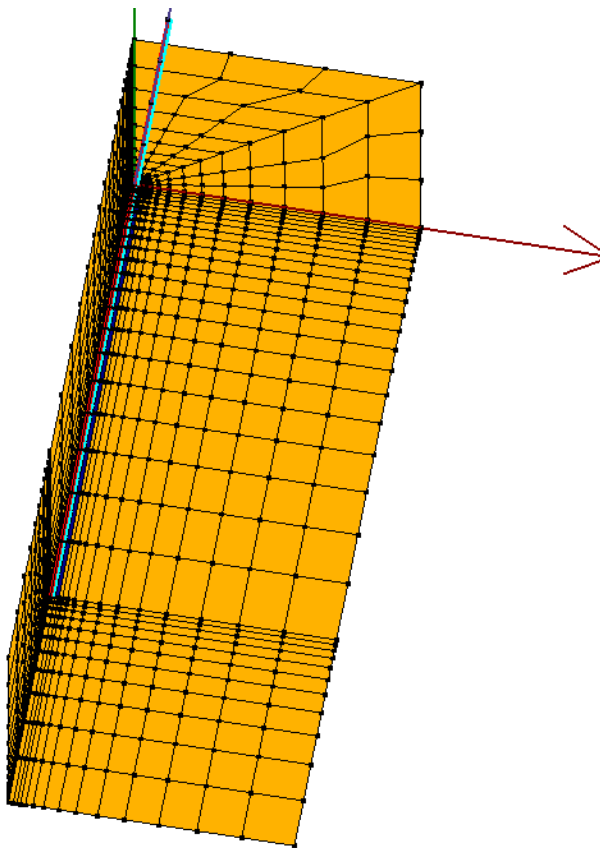


**Figure 4-9:** Medium Meshing scheme

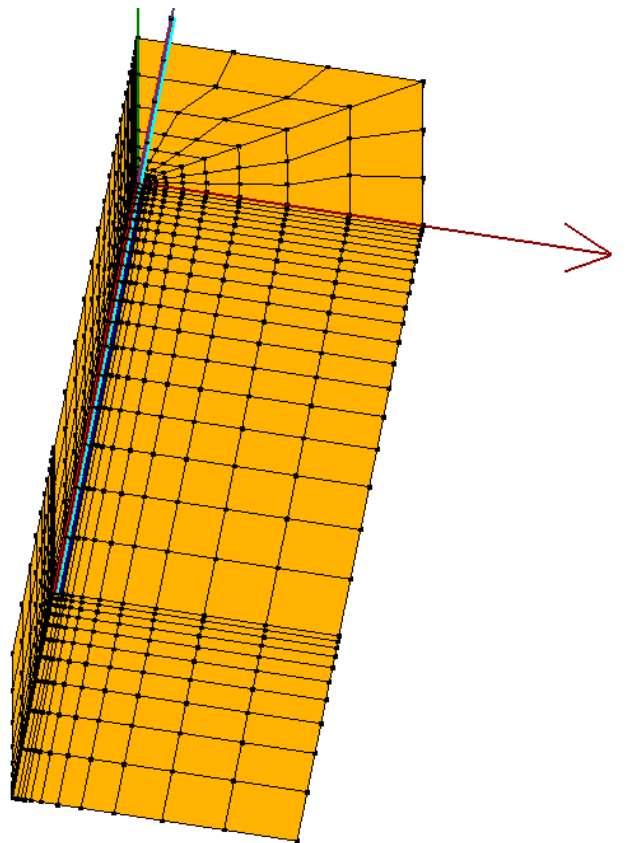


**Figure 4-10:** Loose Meshing scheme

Accumulated displacement curves of the four testing models are plotted in Figure 4-11. From the curves, with increasing mesh densities, larger total displacements would be found after 100 cyclic loading cycles. While the final displacements would decrease by increasing the number of slices (Dense1) in the circumferential direction. In order to improve the simulation efficiency, the medium meshing scheme with the less total number of model elements but with similar displacement outputs to denser meshes will be selected as the final model discretization.

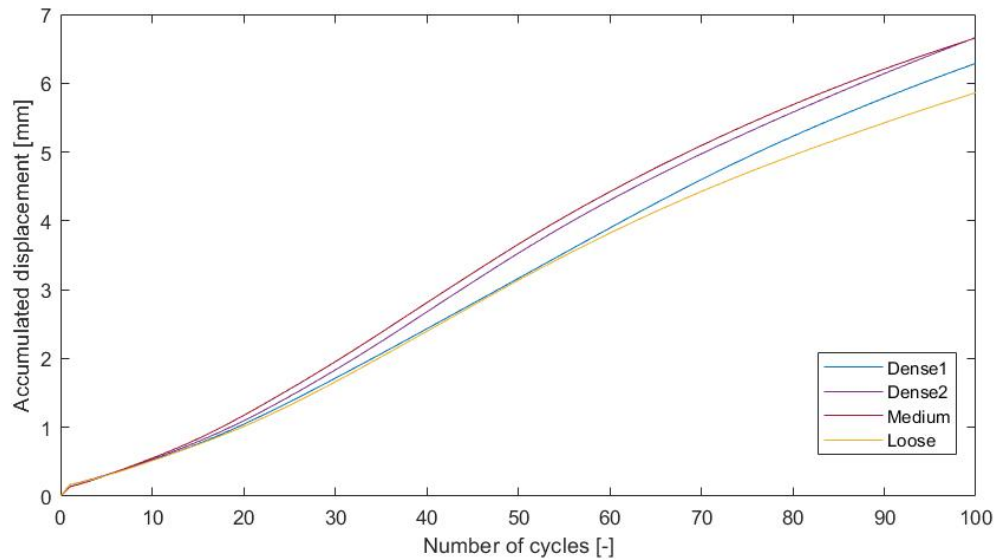


**Figure 4-11:** Accumulated displacement curves of 4 meshing schemes.

## Chapter 5

# Analysis and Results

There are 4 Mini-ICPs tested in the experiment by Tsuha et al. (2012). Except for Mini-ICP1, which has an embedded length of 0.92m, the other three piles were installed 1m beneath the sand surface. After the initial installation, multiple cyclic tests with different combinations of cyclic amplitude and average shaft load were performed on each Mini-ICPs. Monotonic tension tests were done before each cyclic test to track the degradation of the shaft capacity after the previous cyclic loading.

In this section, four models (Installation Mini-ICP1, Mini-ICP2, Mini-ICP3 and Mini-ICP4 in Table 5-1) were established with the same model dimension and mesh discretization, which corresponds to 4 Mini-ICPs in the experiment. Several cyclic loading scenarios were simulated one after another in each model. All ten cyclic loading scenarios in Table 5-1 were selected from the paper Tsuha et al. (2012) with the same load amplitudes as in the experiment.

**Table 5-1:** Cyclic loading scenarios

Installation	Cyclic Test	N	$Q_{cyclic} / Q_T$	$Q_{mean} / Q_T$	Result (Simulation)	Result (Experiment)
Mini-ICP1	ICP1-OW1	1000	0.22	0.22	Stable	Metastable
Mini-ICP2	ICP2-OW1	1000	0.12	0.12	Stable	Stable
Mini-ICP2	ICP2-OW2	1000	0.2	0.2	Stable	Stable
Mini-ICP2	ICP2-OW3	500	0.28	0.28	Metastable	Metastable
Mini-ICP3	ICP3-OW1	100	0.38	0.38	Unstable	Unstable
Mini-ICP3	ICP3-TW1	30	0.54	-0.08	Unstable	Unstable
Mini-ICP3	ICP3-TW2	200	0.4	0.06	Unstable	Unstable
Mini-ICP3	ICP3-TW3	50	0.44	0.02	Unstable	Unstable
Mini-ICP4	ICP4-OW1	2000	0.15	0.15	Stable	Stable
Mini-ICP4	ICP4-TW1	1000	0.23	0.06	Metastable	Metastable

Note: OW means one-way tension tests, TW means cyclic tests which involve both tension and compression loadings

The cyclic load was applied at the pile top with a certain number of loading cycles and was removed before the application of the next loading scenario. The output files of the models included stress and strain of each brick element and the pile head displacement at each time step. According to model results (processed in MATLAB), four *stable* responses, two *metastable* responses and four *unstable* responses were recognized among these cyclic loading scenarios. The results of those cyclic tests showed similar behaviours as the experimental results in the paper Tsuha *et al.* (2012).

The three different response types (*stable*, *metastable* or *unstable*) are defined as:

- For the *stable* response, only very small pile head displacements were detected even after 1000 loading cycles.
- For the *metastable* response, more obvious pile head displacements developed but still not exceed 10%D (3.6mm) after 500-1000 loading cycles.
- For the *unstable* response, the pile head undergoes severe displacements only after a very small number of loading cycles ( $N = 100-200$ ).

In the following parts, example response curves were plotted in terms of stress paths and the pile head displacements after numerous numbers of cyclic loading cycles. Corresponding plots in experimental results were included as comparisons. The entire results of all 10 loading scenarios obtained in the finite element model will be presented in the appendix, Figure A-1 to Figure A-10.

In stress path figures, two extra lines were added to explain relevant mechanisms behind each response type. The dashed line refers to the interface failure line, which in the paper Tsuha *et al.* (2012) the ring shear interface test gave an interface shear angle of  $\delta = 27^\circ$ . The second dot-dash line is the estimated initial Y2 surface, with a limit of  $\Delta\tau_{rz}/\sigma'_r \sim 0.28$  (Kuwano and Jardine's, 2007; Jardine *et al.* (under review)). The Y2 surface is a threshold condition for changes in soil dilatancy. Load cycling within the Y2 surface does not lead to significant strain accumulation, but stress paths that engage the Y2 surface and develop onward show increasingly plastic and irrecoverable behaviour.

Normal (Radial) and shear stresses were recorded at three different vertical locations in the pile-soil interface: a leading cell, a following cell, and a trailing cell. The depth of each recording cell is calculated from the corresponding instrumented cluster (Figure 4-1) in the experimental settings.

## 5.1 Stable response

Four tests are recognized as stable tests from the model results, in which ICP2-OW1 and ICP4-OW1 are small amplitude one-way tension tests. Test ICP1-OW1 and ICP2-OW2 have larger cyclic amplitudes, but the model results still showed a stable response and helped define the lower metastable boundary. The local stress developed at all pile instrument cluster locations is illustrated in Figure A-1 to Figure A-4. Results of test ICP2-OW1 and ICP4-OW1 will be discussed here in detail in comparison to the corresponding experimental results.

### Experiment results

In the experiment, less than 0.1mm pile head displacement developed after thousands number of cyclic loading cycles (Figure 5-2). Interface soil elements at the deeper part (Leading A) did not go across the estimated initial Y2 yield surfaces, but the upper region (Following B/ Trailing C) engaged the Y2 yielding. Minor top-down shaft degradation may develop due to the balance of capacity growth at the deeper part of the pile. The effective stress paths showed modest migration to the left without meeting the interface failure lines  $\delta = 27^\circ$ .

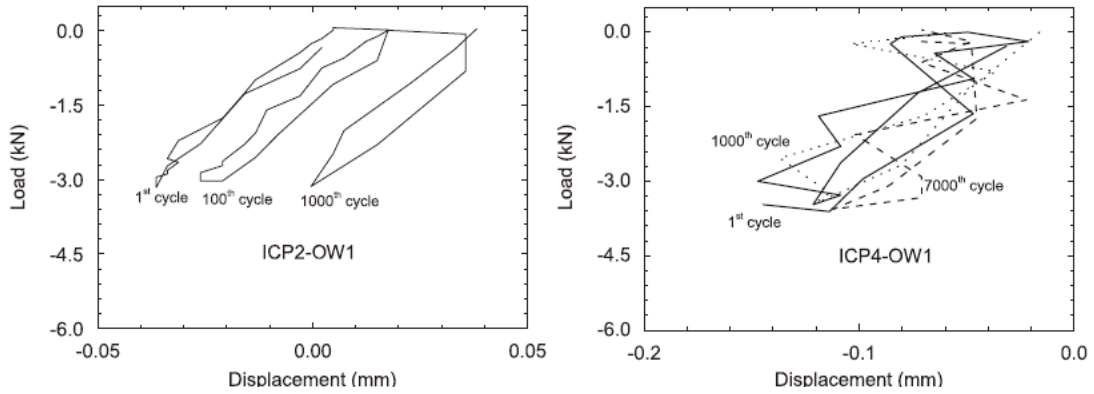


**Figure 5-1:** Load-displacement curves of exemplar stable tests in the experiment (Tsuha et al. 2012)

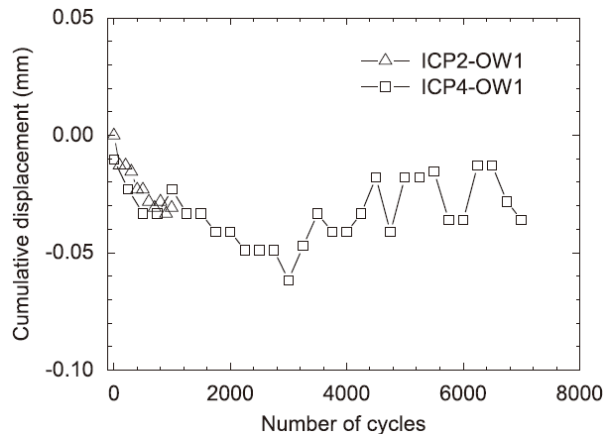


**Figure 5-2:** Cumulative displacement curves of exemplar stable tests in the experiment (Tsuha et al. 2012)

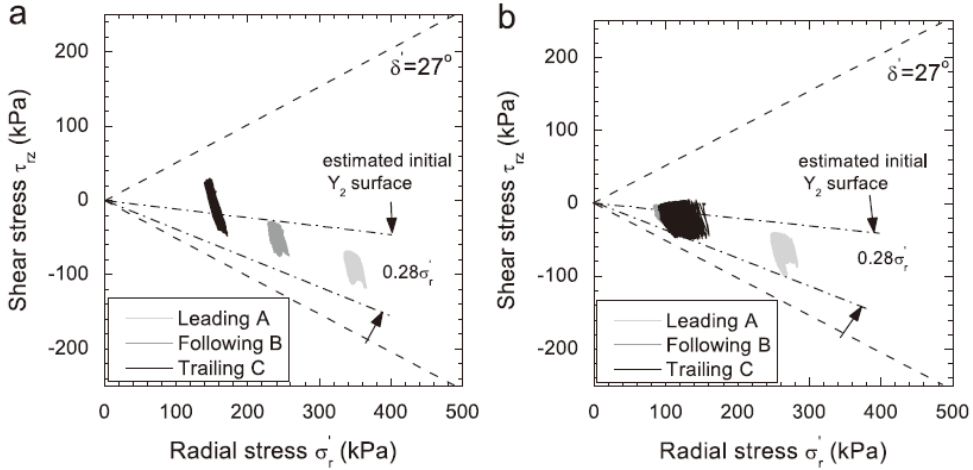


**Figure 5-3:** Stress paths of exemplar stable tests in the experiment: a) ICP2-OW1, b) ICP4-OW1. (Tsuha et al. 2012)

**FEM results**

Model results of test ICP2-OW1 and ICP4-OW1 were shown in Figure 5-4 and Figure 5-5, respectively. The three stress paths migrate ( $\sigma_r$  reducing) to the left but remain within the  $\delta = 27^\circ$  interface shear test envelop. The top-down failure mode is not obvious in the three stable tests from this simulation work. From the cumulative displacement curves in Figure 5-4 and Figure 5-5, small amplitude cyclic tests ICP2-OW1 and ICP4-OW1 only develop less than 1mm cumulative pile head displacements after 1000 loading cycles.

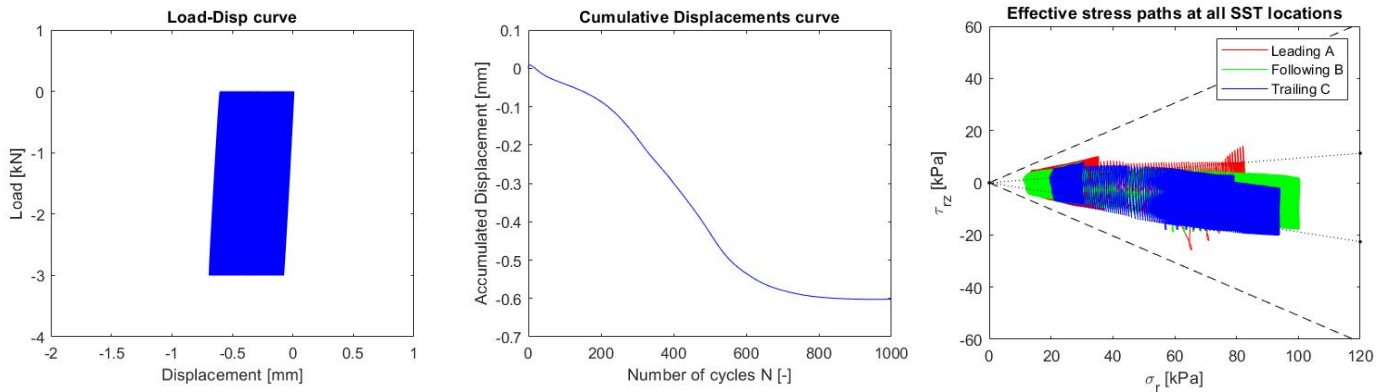


**Figure 5-4:** Model results for stable test ICP2-OW1.

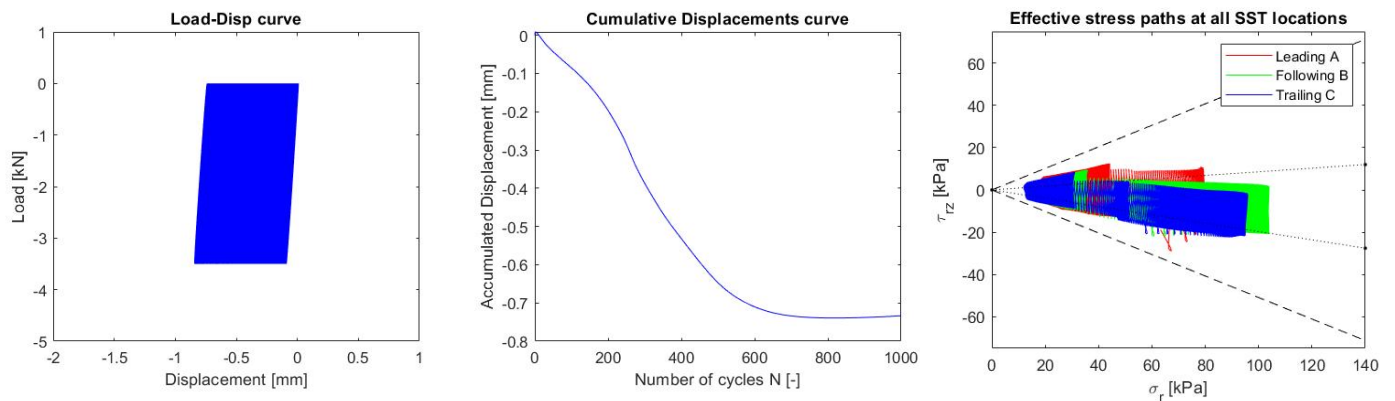


**Figure 5-5:** Model results for stable test ICP4-OW1.

## 5.2 Metastable Tests

Two tests are recognized as *metastable* tests from the model results, in which test ICP2-OW3 is a large amplitude one-way cyclic test, and test ICP4-TW1 is a small amplitude two-way cyclic test. Model results will be discussed below in comparison to the corresponding experimental results.

### Experiment results

From the experimental results, an intermediate behaviour will occur in metastable loading (Figure 5-6-Figure 5-8). Hysteretic stress paths, reduction of effective stresses and shaft capacities, and larger pile head displacements may all develop, depending on the cyclic loading levels applied. However, piles can sustain hundreds of cycles without reaching the failure criterion (pile head displacements equal to 3.6mm) in this type of loading conditions.

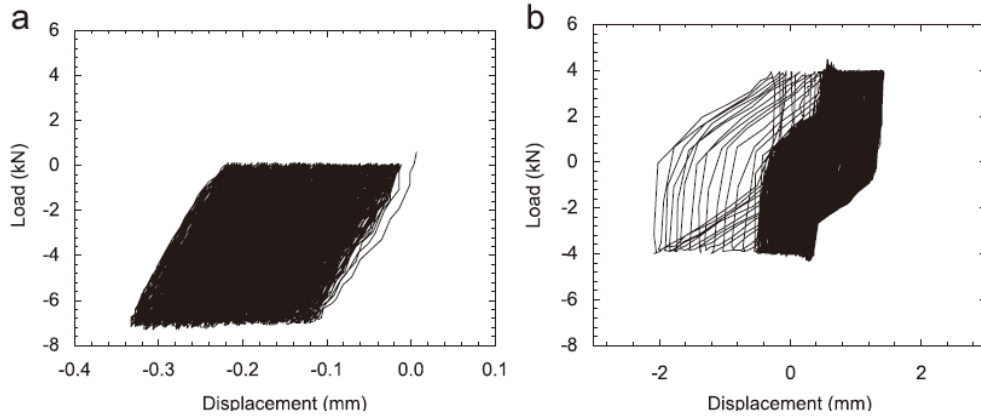


**Figure 5-6:** Load-displacement curves of exemplar metastable tests in the experiment: a) ICP2-OW3, b) ICP4-TW1 (Tsuha et al. 2012).

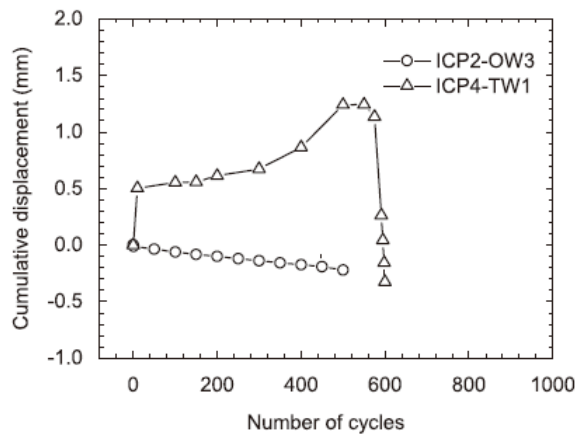


**Figure 5-7:** Cumulative displacement curves of exemplar metastable tests in the experiment (Tsuha et al. 2012).

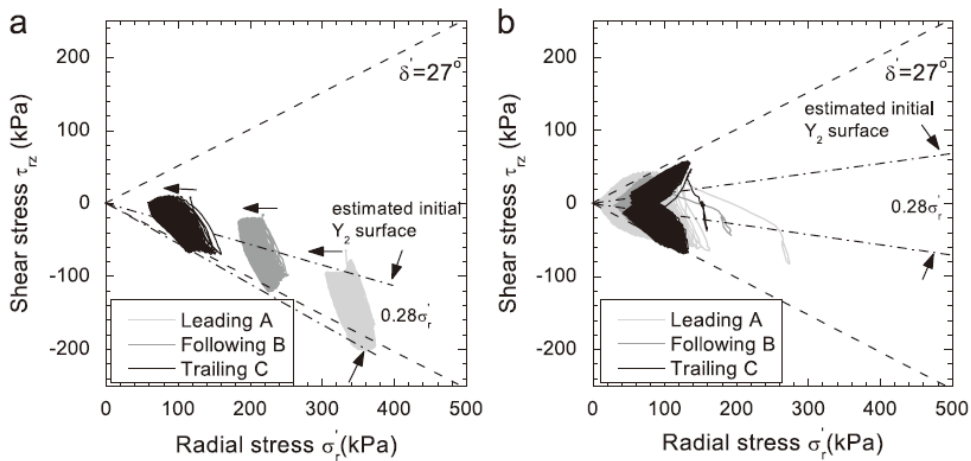


**Figure 5-8:** Stress paths of exemplar metastable tests in the experiment: a) ICP2-OW3, b) ICP4-TW1. (Tsuha et al. 2012).

**FEM results**

From model results in Figure 5-9 and Figure 5-10, the cumulative pile head displacements of the two metastable tests reach 3.6mm (10%D) within 1000 loading cycles. For pile ICP2, the cyclic

amplitude increases further in test OW3, which induces a metastable response. A broader area of three stress paths goes across the lower initial Y2 surface limit and gradually approaches the interface failure envelop. The stress paths of two-way test ICP4-TW1 engage the Y2 yielding in a more symmetric way with a wide range going across both the upper and lower Y2 surface boundary. “Butterfly-wing” stress path patterns are close to developing for two cyclic tests. Densifications in the interface zone contribute to the radial effective stress  $\sigma_r$  release. Only a few stress paths engaging the interface slip line are found in the two-way test ICP4-TW2.

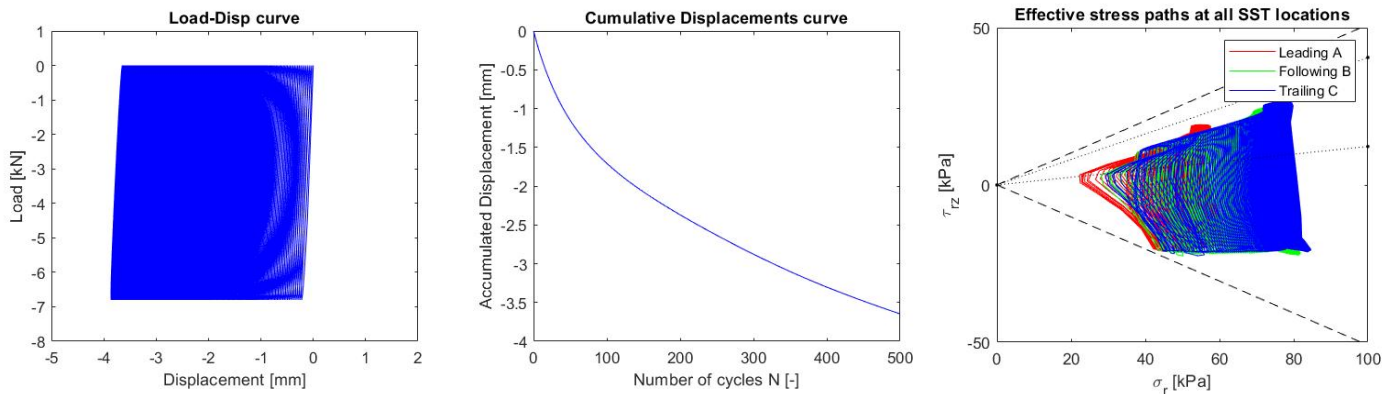


**Figure 5-9:** Model results for metastable tests ICP2-OW3.

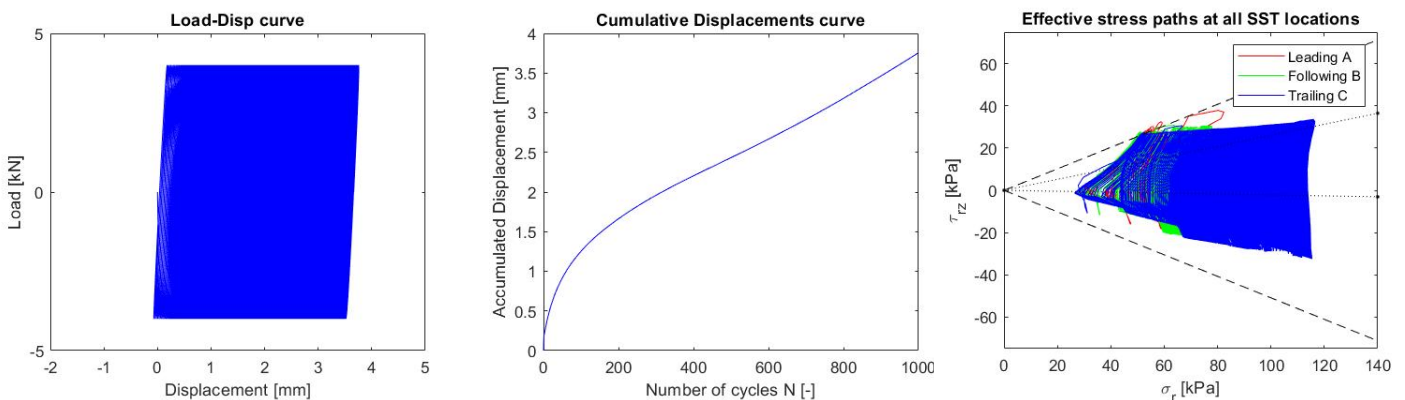


**Figure 5-10:** Model results for metastable tests ICP4-TW1.

## 5.3 Unstable Tests

Unstable responses were found in large amplitude one-way (ICP3-OW1) and two-way (ICP3-TW1, ICP3-TW2 and ICP3-TW3) cyclic tests. The stress paths and displacement curves were summarized in Figure A-7 to Figure A-10. Here in this part, Test ICP3-OW1 and test ICP3-OW2 will be compared to the corresponding results.

### Experiment results

In contrast to stable loading, unstable pile response will reach when: 1) shaft failure and large pile head displacements, to 10%D (3.6mm), observed only within 100 loading cycles; 2) marked radial effective stress  $\sigma_r$  reduction due to the interface shear zone compaction. Asymmetric stress paths

were found in large amplitude one-way cyclic tests. Hysteretic “butter-fly-wing” effective stress paths will develop at the pile-soil interface. The pile failure will progress from the top downwards. The example experiment results were given in Figure 5-11 and Figure 5-12.

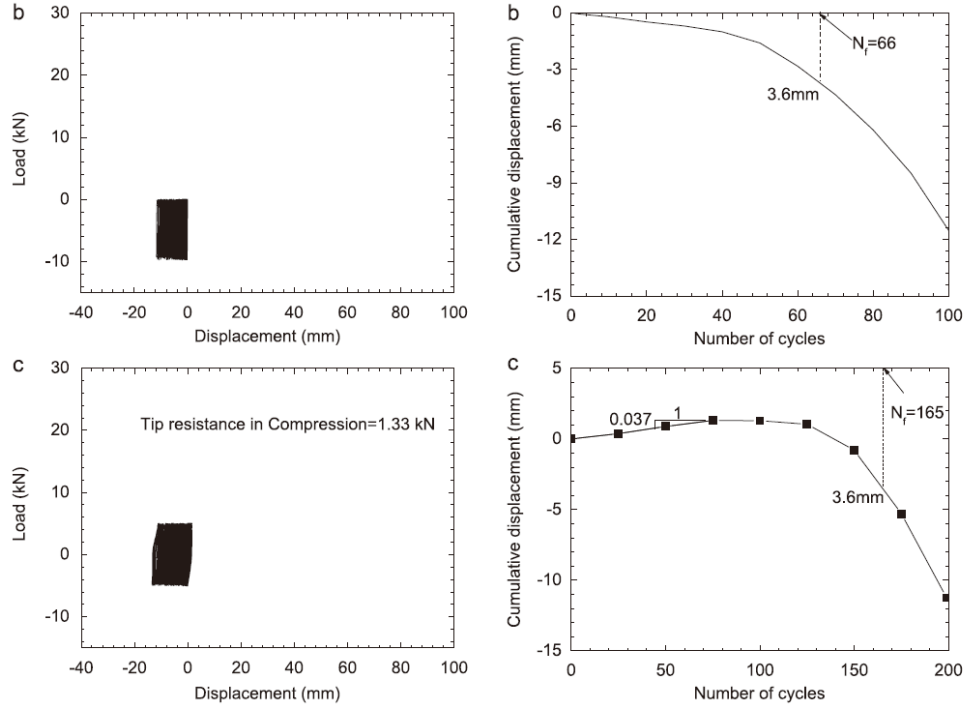


**Figure 5-11:** Load-displacement (left) and Cumulative displacement (right) curves of exemplar unstable tests in the experiment: b) ICP3-OW1, c) ICP3-TW2. (Tsuha et al. 2012)

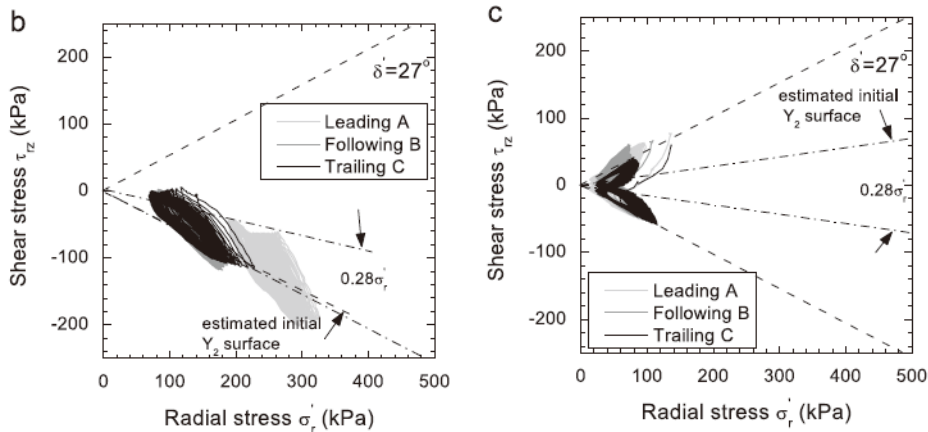


**Figure 5-12:** Stress paths of exemplar unstable tests in the experiment: b) ICP3-OW1, c) ICP3-TW2. (Tsuha et al. 2012).

### FEM results

Below 2 example unstable test results from the model that were plotted in Figure 5-13 and Figure 5-14. Large amplitude one-way test, extreme two-way tests were applied to the ICP3 pile. They all showed unstable responses after those cyclic load tests. The cumulative pile head displacements obtained in these tests all reach 3.6mm only in very few loading cycles ( $N=30-200$ ).

The local stress paths of unstable tests varied substantially, with radial effective stress reducing to zero after few cyclic loading cycles. All unstable tests went out of the initial Y2 surface at the first cycle and proceeded to contract markedly before undergoing phase transformation line. Clear “butterfly-wing” patterns in stress paths are observed only after few loading cycles.

Large amplitude one-way tension test ICP3-OW1 have asymmetric effective stress paths. Symmetric stress paths were observed for the less severe two-way test ICP3-TW2. Stress paths of all unstable tests undergo the ring shear interface slip line  $\delta = 27^\circ$ . The interface was climbed due to the interface shear zone compaction in these tests.

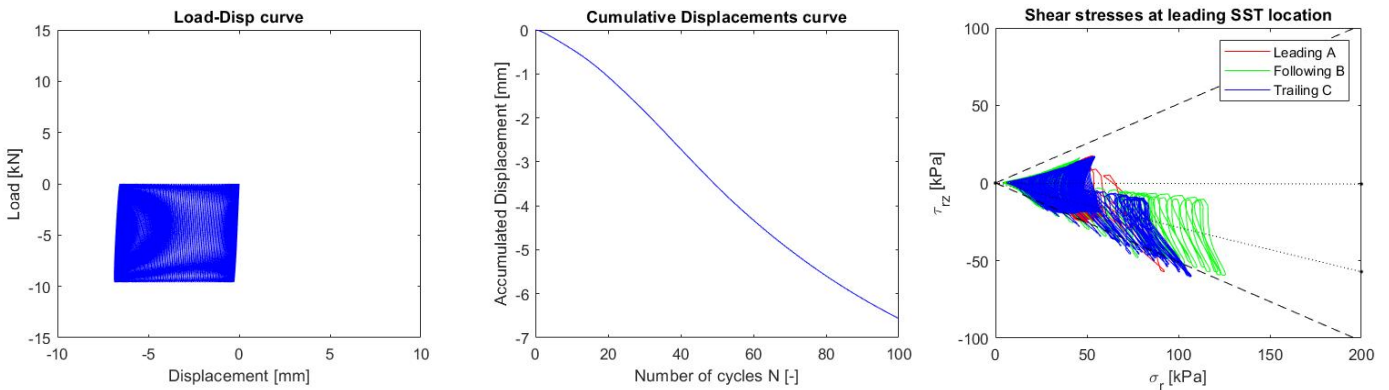


**Figure 5-13:** Model results for unstable tests ICP3-OW1.

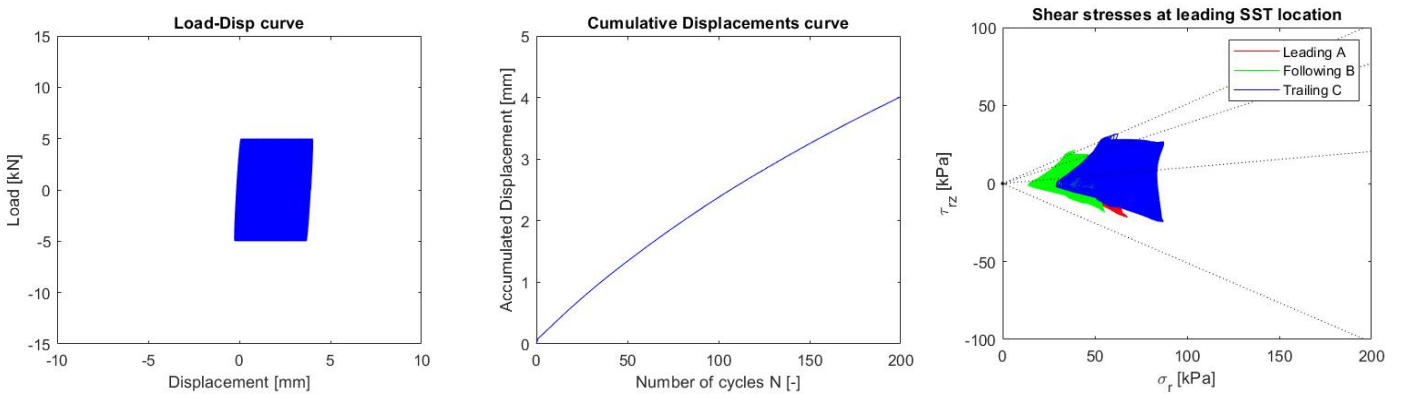


**Figure 5-14:** Model results for unstable tests ICP3-TW2.

## 5.4 Comparison result summary and Interaction diagram

From the above comparison results, the FE model can give clear stable, metastable and unstable responses as in the experiment. Nevertheless, the final displacements after the same number of loading cycles distinguish from the value obtained in the experiments. The cumulative pile head displacement after  $N = 1000$  was larger in stable model results than that in the experiment. But the total pile displacement in unstable tests was much smaller than experimental data.

There is an obvious difference observed in model and experiment results with respect to the initial stress state around the pile shaft. From the experiment results, the radial effective stress at the leading cell was initially larger than the following, and trailing cells and a clear top-down failure mode were found in the experiment. However, the magnitude of initial radial effective stresses was very close in the model results, and they were much smaller than the values detected from the experiment. These differences in the initial stress state were probably due to the absence of the pile installation process in the FE modelling.

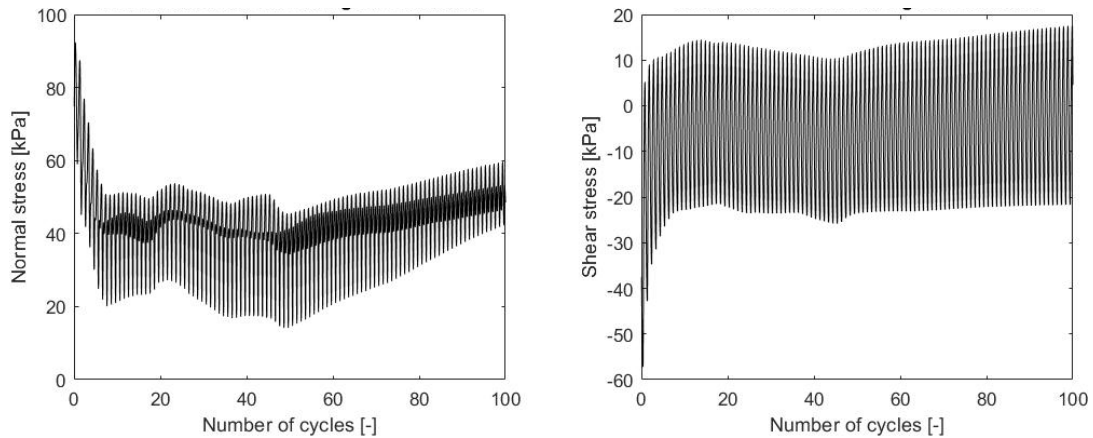


**Figure 5-15:** Stresses at the leading cell location from the FE model result.

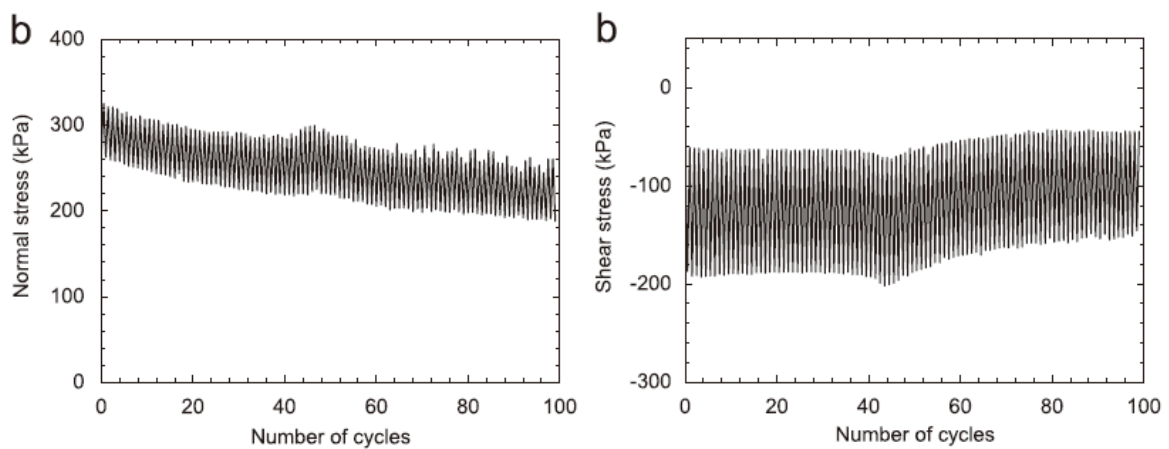


**Figure 5-16:** Stresses at the leading cell location from the experiment result (Tsuha et al. 2012).

Like experimental results, model results were also summarized in an interaction diagram (Figure 5-17), from where the three response types could be easily distinguished. Stable responses were found in small amplitude one-way tests. Unstable responses were found in two-way tests and large amplitude one-way tests. Metastable responses were found in small amplitude two-way tests and relatively larger amplitude one-way tests.

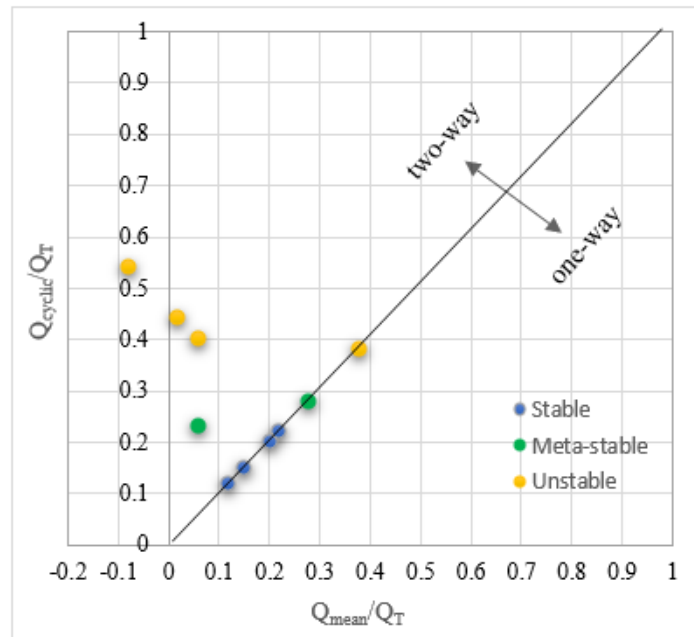


**Figure 5-17:** Summary of model results with failure criterion.

Things to mention: Pile ICP1 was installed with a 0.92m embedded length, which is shallower than other piles. While in this simulation, the embedded lengths of all piles are the same (1m). A larger tip depth contributes to a larger initial shaft capacity of piles. Therefore, from the model result, the test ICP1-OW1 is reasonable to have a stable response, while in the experiment, it is metastable.

## 5.5 Parameter study

There are 16 parameters (Table 3-1) in SANISAND-MS constitutive model, among which were calibrated in Chapter 3 based on purely sand behaviours. It is of great interest that how these parameters would influence the simulation results if pile-sand interaction is involved.

In the above analysis results of 4 Mini-ICP piles, it is obvious that the final pile head displacements obtained in stable tests are much larger than the displacements obtained in experimental work. This is possibly due to the shear modulus parameter  $G_0$  used in the previous analysis. Therefore, model responses with respect to different  $G_0$  values were plotted in the following Figure 5-18.

In drained conditions, cyclic loading will cause the strain accumulation of the surrounding soils. The predictive capability of the SANISAND-MS model under numerous cyclic loading cycles (“high-cyclic” loading) in drained condition is mainly because of the contribution of the newly added memory surface. As mentioned in above chapter 3, there are 3 parameters relevant to memory surface:  $\mu_0$ ,  $\zeta$ , and  $\beta$ . In “high-cyclic” loading, parameter  $\mu_0$  (Eq. 3-16) governs the sand ratcheting response and influences the transition from ratcheting to the shakedown of sand. Parameter  $\zeta$  is the memory surface shrinkage parameter. Dilative behaviour of sand will ‘damage’ the granular fabric and thus cause memory loss, which phenomenologically presents as a decreasing size of the memory surface. The remained parameter  $\beta$  is added in the newly defined dilatancy coefficient equation (Eq.

3-11). It is a parameter controlling the post-dilation process of the sand thus is more important in undrained conditions (Liu et al., 2019). Below, the model performances will be given as varying  $\mu_0$ ,  $\zeta$  and  $\beta$  values to see how it will affect the total pile head displacements.

### 5.4.1 Influence of $G_0$

Normally, a larger shear modulus means the soil is stiffer and will produce less ultimate shear strain. In this section, 4  $G_0$  values were selected to see the shear modulus influence on the ultimate pile head displacement after 1000 loading cycles performed on a stable test.

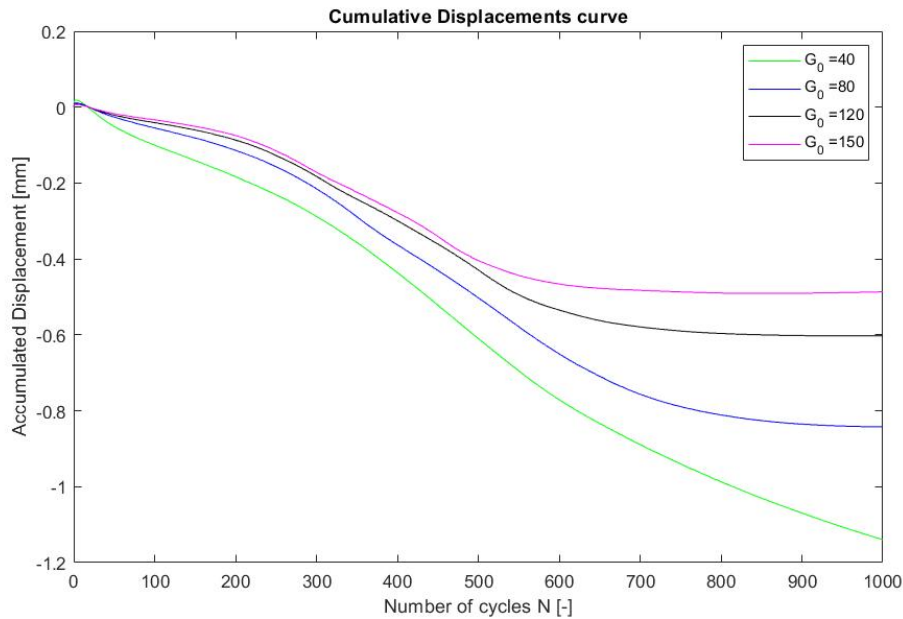


**Figure 5-18:** Displacement curves with varying  $G_0$  values.

It is clear from Figure 5-18 that the accumulated pile head displacement is increasing with decreasing  $G_0$  values (e.g.,  $G_0 = 40$ ). This probably means that a smaller  $G_0$  value in the SANISAND-MS model gives a softer initial sand state which could lead to a larger final displacement. This result can be explained mathematically in Eq. 3-1, and Eq.3-3 with larger  $G_0$  value give smaller elastic strains. Also, a smaller  $G_0$  will lead the displacement to stabilize later.

### 5.4.2 Influence of $\mu_0$

To study the effects of parameter  $\mu_0$  on model performance, models with different  $\mu_0$  values and with other 15 parameters be the same were simulated in this section. The model results were summarized in cumulative displacement curves, given 4 different  $\mu_0$  values, in the following Figure 5-19. It can be concluded that for a small number of loading cycles (around  $N < 200$ ), smaller pile head displacements were found with increasing  $\mu_0$  values. However, when a larger number of loading cycles were applied ( $N > 200$ ), the total pile head displacements increase with increasing  $\mu_0$  values (from 34 to 200). For very small value  $\mu_0 = 1$ , it gave the largest displacement initially and was slightly surpassed by larger  $\mu_0$  values (100 and 200) at around  $N = 400$  while the pile head displacement experienced a sharp reduction when  $N$  exceeds 900.

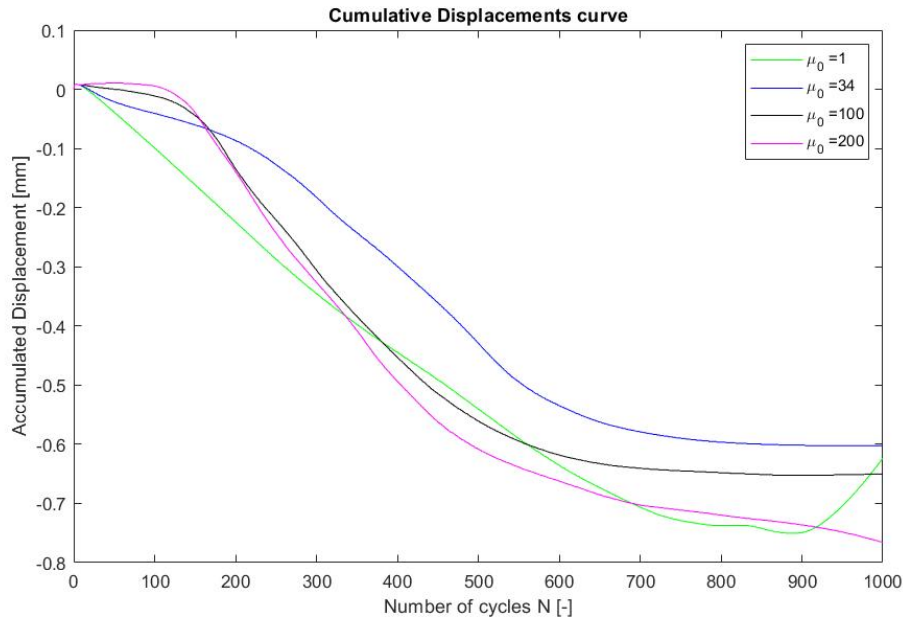


**Figure 5-19:** Displacement curves with varying  $\mu_0$  values.

The initial trend of increasing displacement with decreasing  $\mu_0$  values can be explained by Eq. 3-16, in which a larger  $\mu_0$  value will induce a larger hardening coefficient  $h$  and result in larger plastic modulus  $K_p$  in Eq. 3-18. This then will lead to a smaller plastic multiplier  $L$  which will linearly cause a smaller final accumulated plastic strain in Eq. 3-9 and Eq. 3-10. However, when more loading cycles were applied ( $N > 200$ ), the curves showed a reverse trend with increasing displacement with increasing  $\mu_0$  values (from 34 to 200). This is because that the plastic multiplier is not only influenced by the plastic modulus but also affected by the stress state developed in the sand. When cyclic effects take more considerable as the number of cycles increased, the sand experienced more severe fabric changes that cause the increasing displacement with increasing  $\mu_0$  values. For the value of  $\mu_0 = 1$ , the cyclic influence on sand ratcheting is shaded by the small parameter value. Hence, the influence of  $K_p$  value took the leading role and presented a displacement trend as described at the beginning of this paragraph.

### 5.4.3 Influence of $\zeta$

Similarly, 4 models with different  $\zeta$  values ( $\zeta = 0.00001$ ,  $\zeta = 0.001$ ,  $\zeta = 1$ , and  $\zeta = 100$ ) with other parameters stay the same were performed in this section. Model results are shown in Figure 5-20. From the results, it is obvious that the variation of  $\zeta$  value almost has no influence on the model results. The memory surface shrinkage function of  $\zeta$  then can be confirmed not obvious in drained loading conditions.

The parameter  $\zeta$  appears at the second term of the right-hand side of the memory surface size evolution equation (Eq. 3-20). Therefore, it only takes effects when dilative deformation is non-zero ( $d\varepsilon_{vol}^p < 0$ ). In this case, there is no dilation process during the cyclic loading in this modeling due to the non-distinction observed in displacement curves with different  $\zeta$  values.

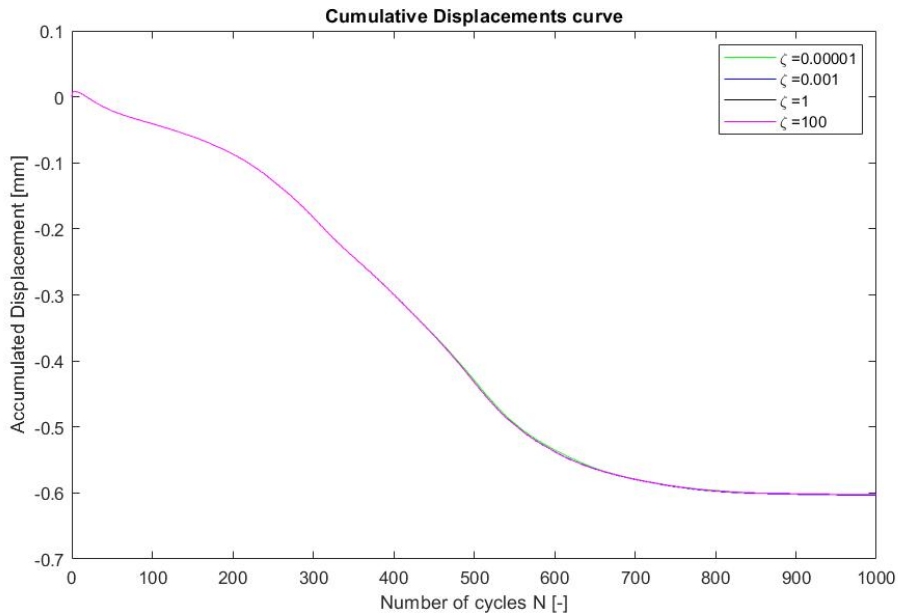


**Figure 5-20:** Displacement curves with varying  $\zeta$  values.

### 5.4.4 Influence of $\beta$

The model performance with varying  $\beta$  values was plotted in Figure 5-21. The model can run larger number of loading cycles with a smaller  $\beta$  values but will stop earlier with larger  $\beta$  value ( $N_{max} < 1000$  at  $\beta = 50$ ). We can conclude from the figure that larger  $\beta$  values will result in larger cumulative displacements.

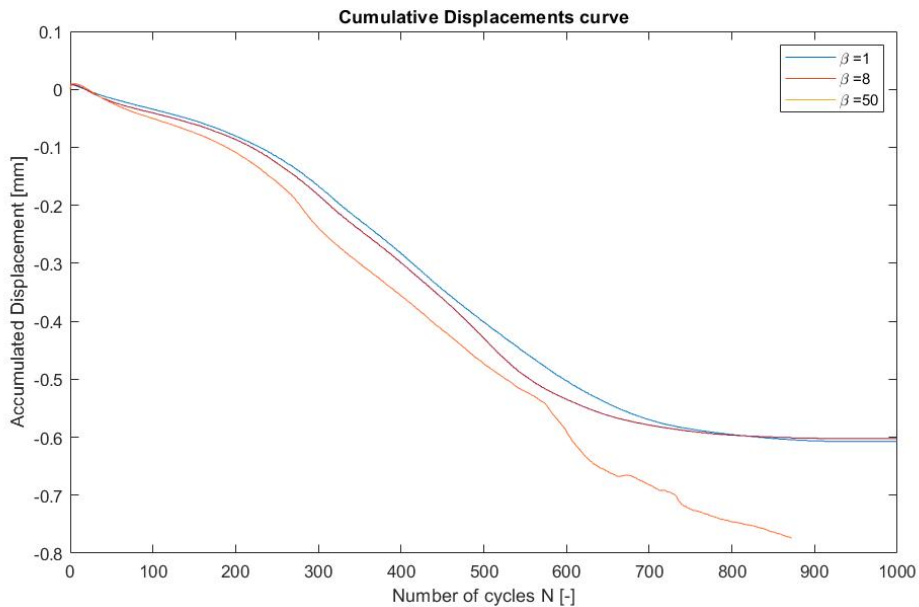


**Figure 5-21:** Displacement curves with varying  $\beta$  values.

The effect of parameter  $\beta$  on the model performance is through the dilatancy coefficient  $D$  defined in Eq. 3-11. A larger  $\beta$  value will give a larger dilatancy coefficient  $D$  which will lead to a higher plastic strain (Eq.3-9) developed in sand mass. This mechanism then can explain the increasing trend of displacement with  $\beta$  value.

## Chapter 6

# Conclusions and Recommendations

## 6.1 Conclusions

The conclusions of this thesis are summarized below:

1. The SANISAND-MS constitutive model can reproduce monotonic drained behaviour of fine silica sand Fontainebleau NE34. Good agreements were found between experimental and simulation results.
2. The calibration of cyclic model parameter is based on a set of symmetric and asymmetric undrained triaxial compression tests.
  - From symmetric loading results: The model could capture “butterfly-wing” stress path with the minimum simulated mean effective stress equals to zero. Nevertheless, the number of cycles to liquefaction is different and this tendency becomes more distinctive at lower cyclic stress ratio  $\eta^{amp}$ .
  - From asymmetric loading results: The constitutive model does not give good matches with the experimental data in one-way asymmetric undrained loading, the simulation stops only when steady loops of stress-strain curves reached.
3. The simulation results generally match the experimental results in three response types. The installation process, as well as time effect after the installation is not included in the analysis. This leads to the initial stress states in model results differ from that in the experimental results.
4. Pile embedded length can influence the final pile capacity in practical situations. Larger pile depth under the soil surface gives larger overall pile capacity under cyclic loading.
5. The FEM results showed clear stable, metastable, and unstable response styles when different combinations of cyclic-to-average ratio cyclic loads were applied to Mini-ICP piles.
  - Piles have a stable response when applied small amplitude one-way cyclic loads. When one-way cyclic amplitude increases to larger values, piles’ response turned to metastable style. Unstable response type can be observed when the cyclic amplitude reaches high value to  $Q_{cyclic} / Q_T$  or  $Q_{mean} / Q_T = 0.38$ .
  - Two-way cyclic tests are easier to trigger unstable responses of the Mini-ICP piles. Small cyclic amplitude two-way test (ICP4-TW1) gives a metastable pile response.
6. In stable tests, stress paths were all within the  $\delta = 27^\circ$  ring shear test interface failure line while wider stress path shifts can be observed in metastable tests with some of them undergoing the interface failure line. From the four unstable cyclic tests, stress paths went across substantially the initial Y2 surface lines and reaching the interface failure criterion, there are sharp reductions of radial effective stress that lead to failure.

7. The  $G_0$  value in the model parameter has a considerable impact on pile head displacement, with a tendency to decrease as the value increases. The influence mode of the cyclic parameter  $\mu_0$  is more complex that depends on the number of cycles applied. The final pile head displacement measured with four different  $\zeta$  values exhibited no difference. Increasing the value of parameter  $\beta$  will give a higher accumulated displacement.

## 6.2 Limitations

There are some limitations that confines the results and conclusions in this paper:

- Lab test results used in model parameter calibration lacks cyclic drained data to calibrate.
- The constitutive model used in this thesis does not perform good in one-way asymmetric undrained loading condition. It is due to the limitation of not including the pre-shearing effect in this version of SANISAND-MS constitutive model.
- The obtained finite element model results here in this thesis were without the consideration of the pile installation effect, pre-cycling effect, and time effect after installation.
- The Mini-ICP piles in the experiment were installed with three highly instrumented measuring equipment at different pile depths, this could influence the piles' total weight and the roughness at pile shafts.

## 6.3 Recommendations

As concluded above, the results from this thesis have many limitations. There are still much to do to have better model results matches the experimental results. Some recommendations are listed below:

- More lab tests on the properties of Fontainebleau NE34 sand are preferred to calibrate the cyclic parameters.
- The SANISAND-MS model should be upgraded in the field of asymmetric undrained cyclic loading conditions.
- Advanced finite element modelling techniques would be required to reproduce the pile installation process, for which influences greatly in the shaft capacity of jacked displacement piles. Material point method can involve large-strain soil deformation would be useful in modelling this kind of geotechnical problems.
- In practical conditions, much larger number of cyclic loads are applied to geotechnical structures. Further studies can be focused on saving the running time of FE models.

# Reference

- Abhinav, K.A. and Saha, N., 2015. Coupled hydrodynamic and geotechnical analysis of jacket offshore wind turbine. *Soil Dynamics and Earthquake Engineering*, 73, pp.66-79.
- Abhinav, K.A. and Saha, N., 2018. Nonlinear dynamical behaviour of jacket supported offshore wind turbines in loose sand. *Marine Structures*, 57, pp.133-151.
- Adhikari, S. & Bhattacharya, S., 2011. Vibrations of wind turbines considering soil-structure interaction. *Wind Struct*, 14(2), pp. 85-112.
- Andersen, K. H., 2009. Bearing capacity under cyclic loading - offshore, along the coast, and onland. *Can. Geotech. J.* 46 (5), 513–535.
- Andersen, K. H., Puech, A. A., Jardine, R. J., 2013. Cyclic resistant geotechnical design and parameter selection for offshore engineering and other applications. *Design for Cyclic Loading: Piles and Other Foundations*. Presse des Ponts, Paris,9–44.
- Atkins Consultants Ltd., 2000. Cyclic degradation of offshore piles. *HSE Offshore Technology Report OTO2000013*. Health and Safety Executive, London.
- B. M. Lehane, R. J. Jardine, A. J. Bond, and R. Frank (1993). Mechanisms of shaft friction in sand from instrumented pile tests. *J. Geotech. Engrg.* 1993.119:19-35.
- Beaty M., Byrne P.M. (1998). An effective stress model for predicting liquefaction behaviour of sand. *Geotechnical Earthquake Engineering and Soil Dynamics III*. P. Dakoulas, M. Yegian, & R Holtz (eds.), ASCE Geo-technical Special Publication 75 (1): 766-777.
- Been, K. and Jefferies, M. G. (1985) A state parameter for sands. *Géotechnique*, 35(1), pp. 99-112.
- Benz, T. 2006. Small-strain stiffness of soils and its numerical consequences. Ph.D. Thesis. Institut für Geotechnik, Universität Stuttgart.
- Bhattacharya S, Nikitas G, Arany L, Nikitas N. Soil-structure interactions (SSI) for offshore wind turbines. *IET Engineering and Technology Reference* 24 (16), The Institution of Engineering and Technology; 2017.
- Bhattacharya, S., Cox, J. A., Lombardi, D. & Muir Wood, D., 2011. Dynamics of offshore wind turbines supported on two foundations. *Geotechnical Engineering*, pp. 159-169.
- Boulanger RW, Ziotopoulou K (2012). “A sand plasticity model for earthquake engineering applications: Version 2.0.” Report No. UCD/CGM-12/01, Center for Geotechnical Modeling, Department of Civil and Environmental Engineering, University of California, Davis, CA, 100 pp.

- Boulanger RW, Ziotopoulou K (2015). PM4Sand (version 3): A sand plasticity model for earthquake engineering applications. Report No. UCD/CGM-15/01. Center for Geotechnical Modeling, University of California at Davis.
- Boulanger RW, Ziotopoulou K (2017). PM4Sand (version 3.1): A sand plasticity model for earthquake engineering applications. Report No. UCD/CGM-17/01. Center for Geotechnical Modeling, University of California at Davis.
- Carswell W, Arwade SR, Degroot DJ, Myers AT. Natural frequency degradation and permanent accumulated rotation for offshore wind turbine monopiles in clay. *Renew Energy* 2016; 97:319–30.
- Chen IW, Wong BL, Lin YH, Chau SW, Huang HH. Design and analysis of jacket substructures for offshore wind turbines. *Energies* 2016;9(4). 264.
- Cheng-Yu Ku and Lien-Kwei Chien, 2016. Modeling of Load Bearing Characteristics of Jacket Foundation Piles for Offshore Wind Turbines in Taiwan. *Energies* 2016, 9, 625; doi:10.3390/en9080625.
- Chow, F.C., 1997. Investigation into Displacement Pile Behaviour for Offshore Foundations (Ph.D. thesis). Imperial College London, London, UK.
- Coop, M. R. & Lee, I. K. (1993). The behaviour of granular soils at elevated stresses. *Proceedings of the C. P. Wroth Memorial Symposium: Predictive soil mechanics*, London, pp. 186–198.
- Coop, M. R. (1990). The mechanics of uncemented carbonate sands. *Geotechnique* 40, No. 4, 607–626, <http://dx.doi.org/10.1680/geot.1990.40.4.607>.
- Coop, M. R. (1999). The influence of particle breakage and state on the behaviour of sands. *Proc. 2nd Int. Workshop on Crushable Soils, Yamaguchi, Japan*, pp. 19–57.
- Dafalias, Y. and Taiebat, M. (2016). SANISANDZ: zero elastic range sand plasticity model. *Géotechnique*, 66(12):999–1013.
- Dafalias, Y. F., & Manzari, M. T. 2004. Simple plasticity sand model accounting for fabric change effects. *Journal of Engineering mechanics*, 130(6), 622-634.
- Dafalias, Y. F., & Popov, E. P. 1975. A model of nonlinearly hardening materials for complex loading. *Acta mechanica*, 21(3), 173-192.
- Damiani R, Dykes K, Scott G. A comparison study of offshore wind support structures with monopiles and jackets for U.S. waters. *J Phys Conf Ser* 2016;753(9):092003.
- Dong W, Moan T, Gao Z. Long-term fatigue analysis of multi-planar tubular joints for jacket-type offshore wind turbine in time domain. *Eng Struct* 2011;33(6): 2002–14.
- Engin, Harun Kürşat. "Modelling pile installation effects: a numerical approach." (2013).
- European Commission (2013) Green paper: A 2030 framework for climate and energy policies (*COM (2013) 169 final*), Brussels, Belgium: Author.

- Garrad Hassan GL. European offshore wind market: present and future. *Modern Power Systems* 2010;9:37–8.
- Gavin K, Igoe D and Doherty P (2011) Piles for offshore wind turbines: a state-of-the-art review. *Proceedings of the Institution of Civil Engineers – Geotechnical Engineering*, 164(4): 245–256.
- Global Wind Energy Council. Global Offshore Wind Report 2020. Available online: [https://gwec.net/wp-content/uploads/dlm\\_uploads/2020/08/GWEC-offshore-wind-2020-5.pdf](https://gwec.net/wp-content/uploads/dlm_uploads/2020/08/GWEC-offshore-wind-2020-5.pdf) (accessed on 11 August 2020).
- Global Wind Energy Council. GWEC Global wind report. 2021. Available online: <https://gwec.net/wp-content/uploads/2021/03/GWEC-Global-Wind-Report-2021.pdf>
- Guo Z, Yu LQ, Wang LZ, Bhattacharya S, Nikitas G, Xing Y. Model tests on the long-term dynamic performance of offshore wind turbines founded on monopiles in sand. *J Offshore Mech Arct Eng* 2015;137(4). 041902-041902-11.
- IEA (2020), *World Energy Outlook 2020*, OECD Publishing, Paris, <https://doi.org/10.1787/557a761b-en>.
- IRENA (2021), *Renewable capacity statistics 2021* International Renewable Energy Agency (IRENA), Abu Dhabi.
- Jalbi S. and Bhattacharya, S., 2018. Closed form solution for the first natural frequency of offshore wind turbine jackets supported on multiple foundations incorporating soil-structure interaction. *Soil Dynamics and Earthquake Engineering*, 113, pp.593-613.
- Jalbi, S. and Bhattacharya, S., 2020. Concept design of jacket foundations for offshore wind turbines in 10 steps. *Soil Dynamics and Earthquake Engineering*, 139, p.106357.
- Jalbi S., Nikitas G., Bhattacharya S., Alexander N., See fewer, Dynamic design considerations for offshore wind turbine jackets supported on multiple foundations. in *Marine Structures* (2019).
- Jardine, R. J., Zhu, B. T., Foray, P., & Yang, Z. X. (2013). Interpretation of stress measurements made around closed-ended displacement piles in sand. *Géotechnique*, 63(8), 613-627.
- Jardine, R.J., 1991. The cyclic behaviour of offshore piles. *The Cyclic Loading of Soils*. Blackie & Son, Glasgow.
- Jardine, R.J., 2013. Advanced laboratory testing in research and practice: the 2nd Bishop Lecture. In: *Proceedings of 18th I.C.S.M.G.E, vol. 1*. Presses des Ponts, Paris, pp. 35–35.
- Jardine, R.J., Andersen, K., Puech, A., 2012. Cyclic loading of offshore piles: potential effects and practical design. In: *Proceedings of the 7th International Conference on Offshore Site Investigations and Geotechnics*. SUT Publications, London, UK, pp. 59–100.
- Jardine, R.J., Standing, J.R., 2000. Pile Load Testing Performed for HSE Cyclic Loading Study at Dunkirk, France. Health and Safety Executive, London Offshore Technology Report No. OTO 2000 007.

- Jardine, R.J., Standing, J.R., 2012. Field axial cyclic loading experiments on piles driven in sand. *Soils Found.* 52 (4), 723–736.
- Jardine, Richard, et al. ICP design methods for driven piles in sands and clays. Vol. 112. London: Thomas Telford, 2005.
- K. Mahutka, F. Konig, and J. Grabe. Numerical modelling of pile jacking, driving and vibro driving. in International conference on Numerical Simulation of Construction Processes in Geotechnical Engineering for Urban Environment (Bochum, Rotterdam, 2006).
- Kaynia, A. M. (2018). Seismic considerations in design of offshore wind turbines. *Soil Dynamics and Earthquake Engineering*. DOI: [10.1016/j.soildyn.2018.04.038](https://doi.org/10.1016/j.soildyn.2018.04.038)
- Khan, Z., El Naggar, M. H., & Cascante, G. (2011). Frequency dependent dynamic properties from resonant column and cyclic triaxial tests. *Journal of the Franklin Institute*, 348(7), 1363-1376.
- Kuwano, R., Jardine, R.J., 2007. A triaxial investigation of kinematic yielding in sand. *Geotechnique* 57 (7), 563–579.
- Lee, K. L. & Seed, H. B. (1967). Drained strength characteristics of sands, *J. Soil Mech. Found. Div ASCE* 93, No. SM6, 117–141.
- Lehane, B.M., Jardine, R.J., Bond, A.J., Frank, R., 1993. Mechanisms of shaft friction in sand from instrumented pile tests. *J. Geotech. Eng.* 119 (1), 19–35.
- Liu, H. (2020). Constitutive modelling of cyclic sand behaviour for offshore foundations.
- Liu, H. Y., Abell, J. A., Diambra, A., & Pisanò, F. (2019). Modelling the cyclic ratcheting of sands through memory-enhanced bounding surface plasticity. *Géotechnique*, 69(9), 783-800.
- Manzari, M. T., & Dafalias, Y. F. (1997). A critical state two-surface plasticity model for sands. *Géotechnique*, 47(2), 255-272.
- Merritt, A.S., Schroeder, F.C., Jardine, R.J., Stuyts, B., Cathie, D., Cleverly, W., 2012. Development of pile design methodology for an offshore wind farm in the North Sea. In: *Proceedings of the 7th International Conference on Offshore Site Investigations and Geotechnics*. SUT Publications, London, UK, pp. 439–447.
- Muskulus M, Schafhirt S. Design optimization of wind turbine support structures-a review. *J Ocean Wind Energy* 2014;1(1):12–22.
- Nguyen Phuong, Frits van Tol, Alexander Rohe (2014). New developments in numerical modelling of pile installation. KIVI Geotechnical Lectures Evening, TU Delft.
- Oh KY, Nam W, Ryu MS, Kim JY, Epureanu BI. A review of foundations of offshore wind energy convertors: current status and future perspectives. *Renew Sustain Energy Rev* 2018; 88:16–36.
- Papadimitriou, A. G. and Bouckovalas, G. D. (2002). Plasticity model for sand under small and large cyclic strains: a multiaxial formulation. *Soil Dynamics and Earthquake Engineering*, 22(3):191–204.

- Papadimitriou, A. G., Bouckovalas, G. D., and Dafalias, Y. F. (2001). Plasticity model for sand under small and large cyclic strains. *Journal of Geotechnical and Geoenvironmental Engineering*, 127(11):973–983.
- Papadimitriou, A. G., Chaloulos, Y. K., and Dafalias, Y. F. (2019). A fabricbased sand plasticity model with reversal surfaces within anisotropic critical state theory. *Acta Geotechnica*, 14(2):253–277.
- Pisano, F. (2019). Input of advanced geotechnical modelling to the design of offshore wind turbine foundations. In H. Sigursteinsson, S. Erlingsson, & B. Bessason (Eds.), *Proceedings of the XVII ECSMGE-2019: Geotechnical Engineering foundation of the future* (pp. 1-26). [1099] Icelandic Geotechnical Society (IGS). <https://doi.org/10.32075/17ECSMGE-2019-1099>
- R. Salgado, J. Mitchell, and M. Jamiolkowski, Calibration chamber size effects on penetration resistance in sand, *Journal of Geotechnical and Geoenvironmental Engineering* 124, 878 (1998).
- Randolph MF. (1994). RAZ program manual: Load transfer analysis of axially loaded piles. Dept. of Civil and Resource Engineering, University of Western Australia.
- Randolph, M. and Gourvenec, S. (2011) *Offshore Geotechnical Engineering*. CRC Press.
- Rimoy S, Jardine RJ and Standing JR. (2013). Displacement response to axial cycling of piles driven in sand. To appear in *Geotechnical Engineering*, Themed Edition. September 2013.
- Rimoy SP, Jardine RJ, Silva M, Foray PY, Tsuha CHC and Yang Z. (2012). Local and global behaviour of cyclically loaded instrumented model displacement piles in sand. In: *Proc. 7th Offshore Site Investigation and Geotechnics: Integrated Geotechnologies – Present and Future*. London: SUT.
- Roscoe, K. H., Schofield, A. N. and Wroth, C. P. (1958) On the Yielding of Soils. *Géotechnique*, 8(1), pp. 22-53.
- S. Lindenberg, B. Smith, K. ODell, E. DeMeo, B. Ram. 20% wind energy by 2030, increasing wind energy's contribution to U.S. electricity supply. *US Department of Energy, Washington DC* (2008).
- Sawyer S. A fresh boost for offshore wind in the USA. *Renewable Energy Focus* 2010;11(4):52–4.
- Schanz T, Vermeer PA, Bonnier PG (1999) The hardening soil model: formulation and verification. In: *Beyond 2000 in computational geotechnics. Ten years of PLAXIS International. Proceedings of the international symposium*, pp 281–296.
- Schoeld, A. and Wroth, C. *Critical State Soil Mechanics*. McGraw-Hill, 1968.
- Seed, H. B. & Silver, M. L. (1972). Settlement of dry sands during earthquakes. *J. Soil Mech. Found. Div. ASCE* 98, No. 4, 381– 396.
- Seidel M. Wave induced fatigue loads: insights from frequency domain calculations. *Stahlbau* 2014;83(8):535–41.
- Shi W, Park HC, Chung CW, Shin HK, Kim SH, Lee SS, Kim CW. Soil-structure interaction on the

- response of jacket-type offshore wind turbine. *Int J Precision Eng Manufact Green Technol* 2015;2(2):139–48.
- Silver, M. & Seed, H. B. (1971). Volume changes in sand during cyclic loadings. *J. Soil Mech. Found. Div. ASCE* 97, No. SM9, 1171–1182.
- Sim, W.W., Aghakouchak, A., Jardine, R.J., 2013. Cyclic triaxial tests to aid offshore pile analysis and design. *Proc. Inst. Civ. Eng. – Geotech. Eng.* 166 (2), 111–121.
- Taiebat, M. and Dafalias, Y. F. (2008). Sanisand: Simple anisotropic sand plasticity model. *International Journal for Numerical and Analytical Methods in Geomechanics*, 32(8):915–948.
- Tsuha, C.H.C., Foray, P.Y., Jardine, R.J., Yang, Z.X., Silva, M., Rimoy, S., 2012. Behaviour of displacement piles in sand under cyclic axial loading. *Soils Found.* 52 (3), 393–410.
- Van der Tempel J, Diepeveen NF, Salzmann DJ, de Vries WE. Design of support structures for offshore wind turbines. In: *Wind power Generation and wind turbine design*. s.l. WIT Press; 2010.
- Wei, K., Myers, A.T. and Arwade, S.R., 2017. Dynamic effects in the response of offshore wind turbines supported by jackets under wave loading. *Engineering Structures*, 142, pp.36-45.
- Wichtmann, T. & Triantafyllidis, Th. (2004a). Influence of a cyclic and dynamic loading history on dynamic properties of dry sand, part I: Cyclic and dynamic torsional prestraining. *Soil Dynam. Earthquake Engng* 24, No. 2, 127–147.
- Wichtmann, T. & Triantafyllidis, Th. (2004b). Influence of a cyclic and dynamic loading history on dynamic properties of dry sand, part II: Cyclic axial preloading. *Soil Dynam. Earthquake Engng* 24, No. 11, 789–803.
- Wichtmann, T., & Triantafyllidis, T. (2015). An experimental database for the development, calibration and verification of constitutive models for sand with focus to cyclic loading: part II—tests with strain cycles and combined loading. *Acta Geotechnica*, 11(4), 739-761.
- Wichtmann, T., & Triantafyllidis, T. (2016). An experimental database for the development, calibration and verification of constitutive models for sand with focus to cyclic loading: part I—tests with monotonic loading and stress cycles. *Acta Geotechnica*, 11(4), 739-761.
- Wichtmann, T., Niemunis, A. & Triantafyllidis, Th. (2005). Strain accumulation in sand due to cyclic loading: drained triaxial tests. *Soil Dynamics. Earthquake Engineering* 25, No. 12, 967–979.
- Yang, Z.X., Jardine, R.J., Zhu, B.T., Foray, P., Tsuha, C.H.C., 2010. Sand grain crushing and interface shearing during displacement pile installation in sand. *Géotechnique* 60 (6), 469–482.
- Youd, T. L. (1972). Compaction of sands by repeated shear straining. *J. Soil Mech. Found. Div. ASCE* 98, No. SM7, 709–725.

# Appendix

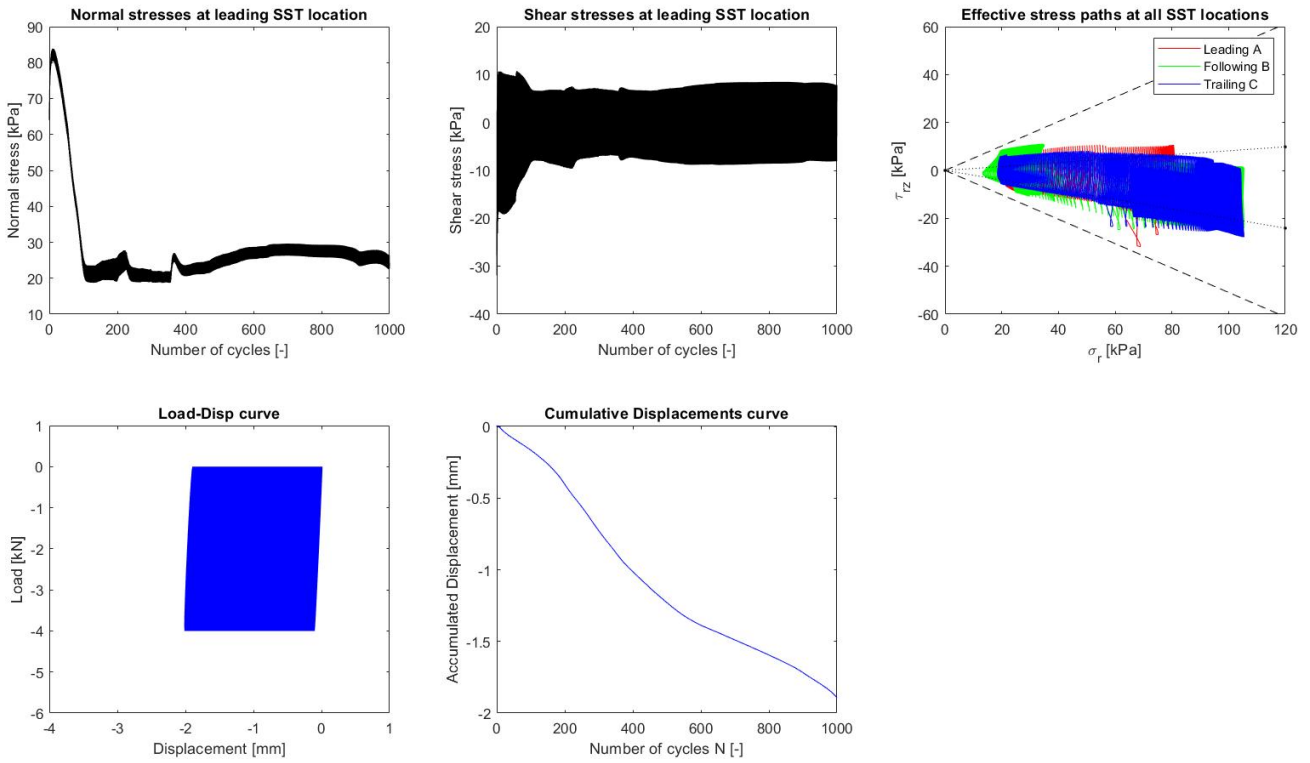


**Figure A-1:** Model results for stable tests ICP1-OW1.

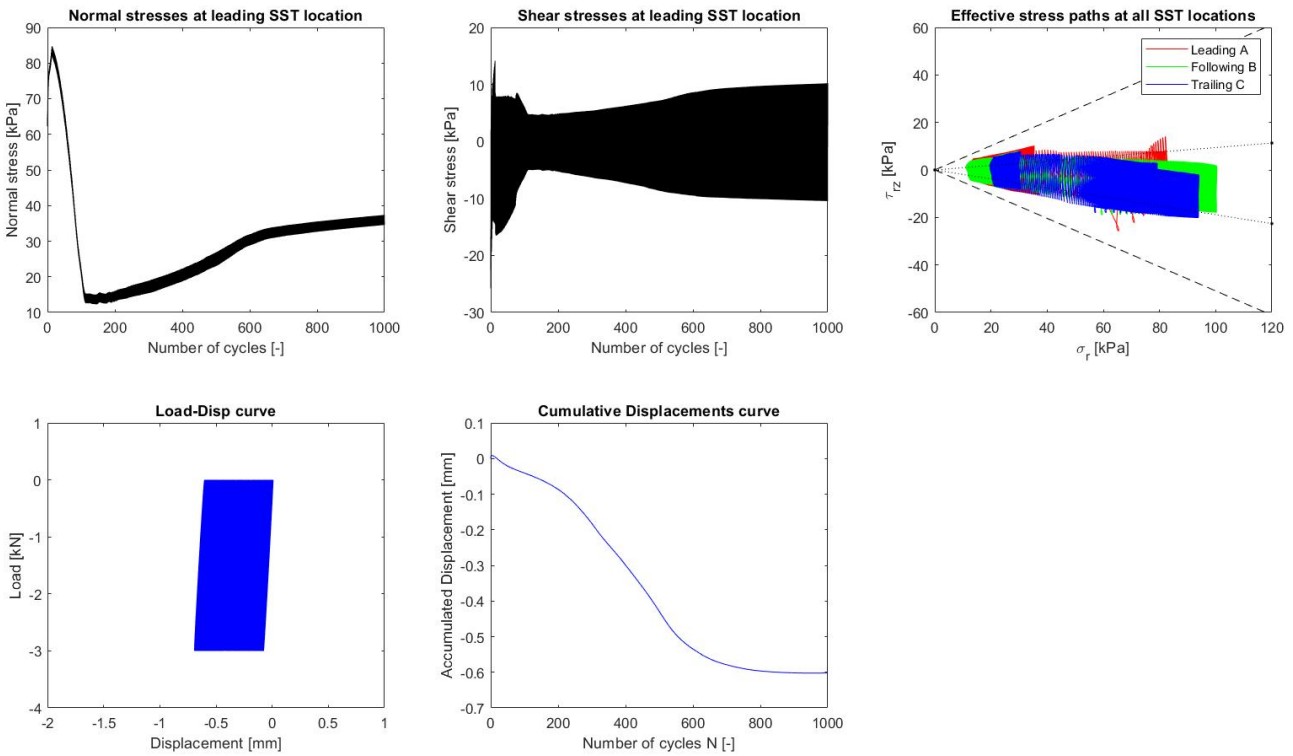


**Figure A-2:** Model results for stable test ICP2-OW1.

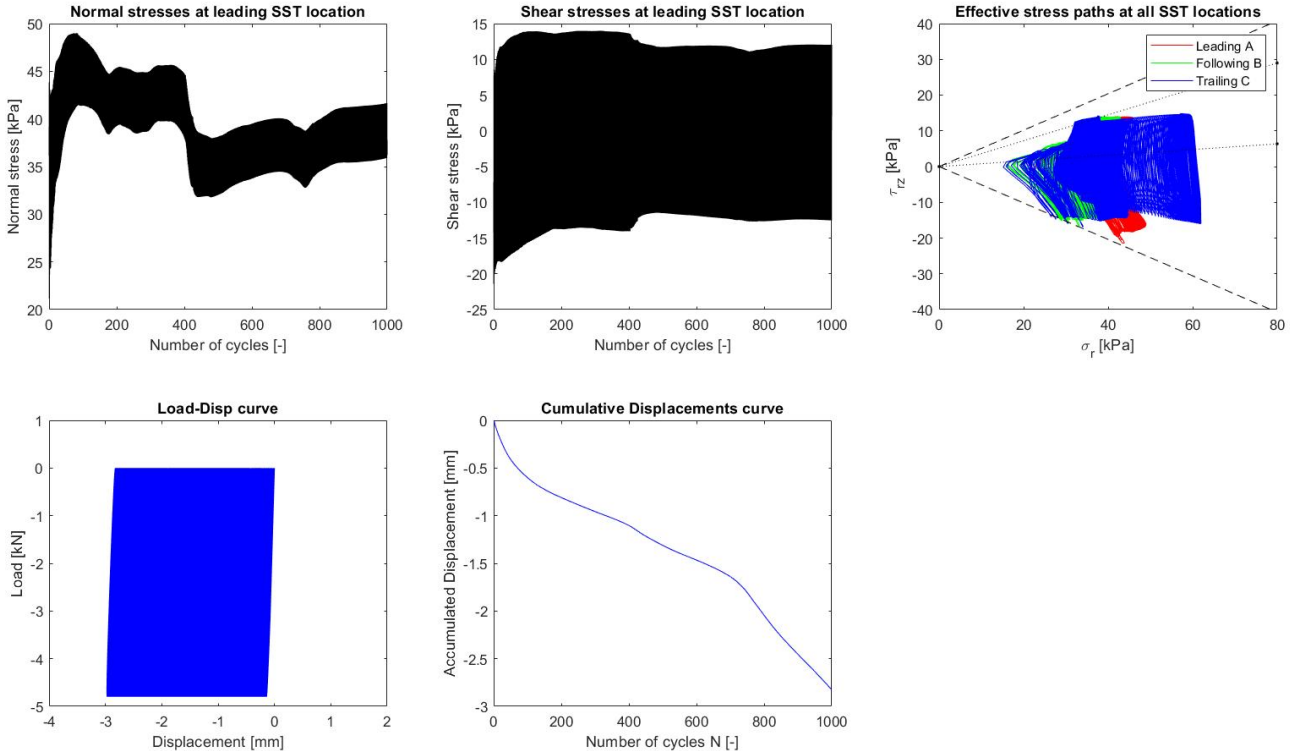


**Figure A-3:** Model results for stable test ICP2-OW2.

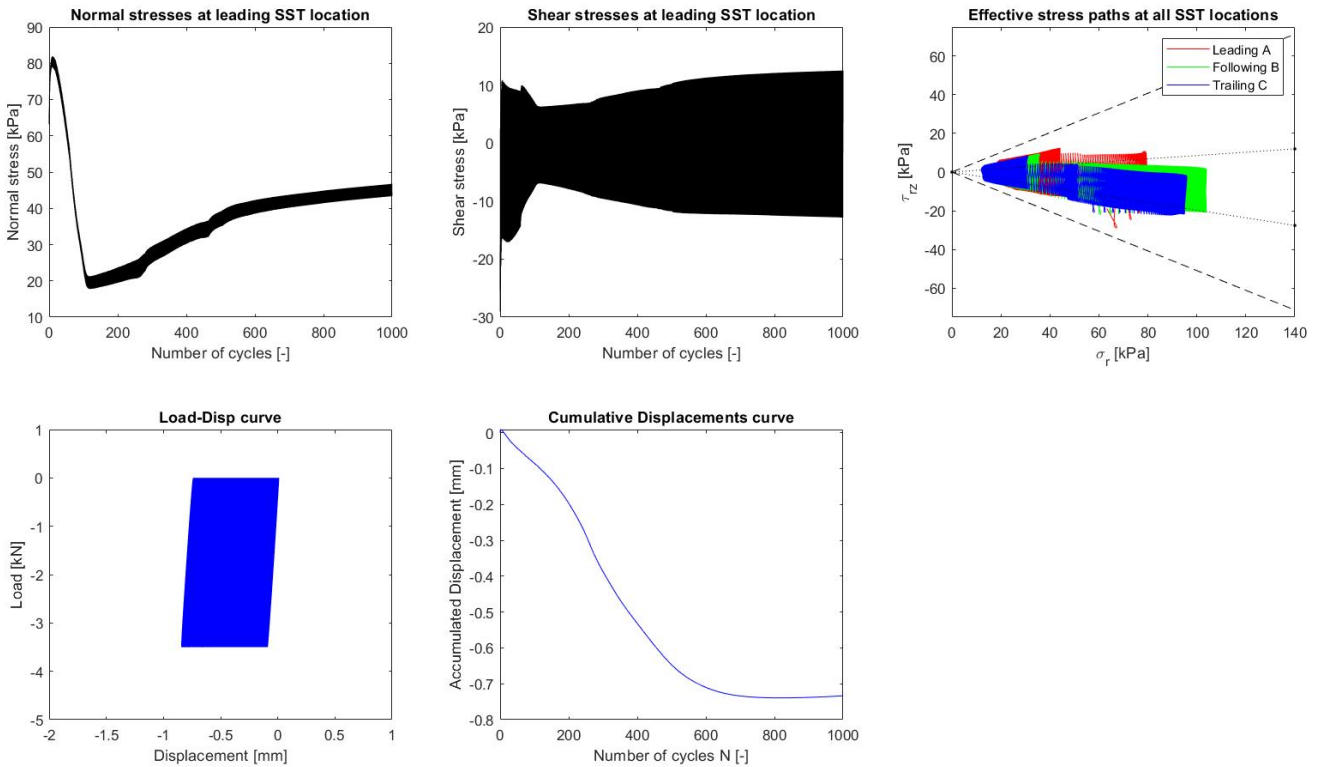


**Figure A-4:** Model results for stable test ICP4-OW1.

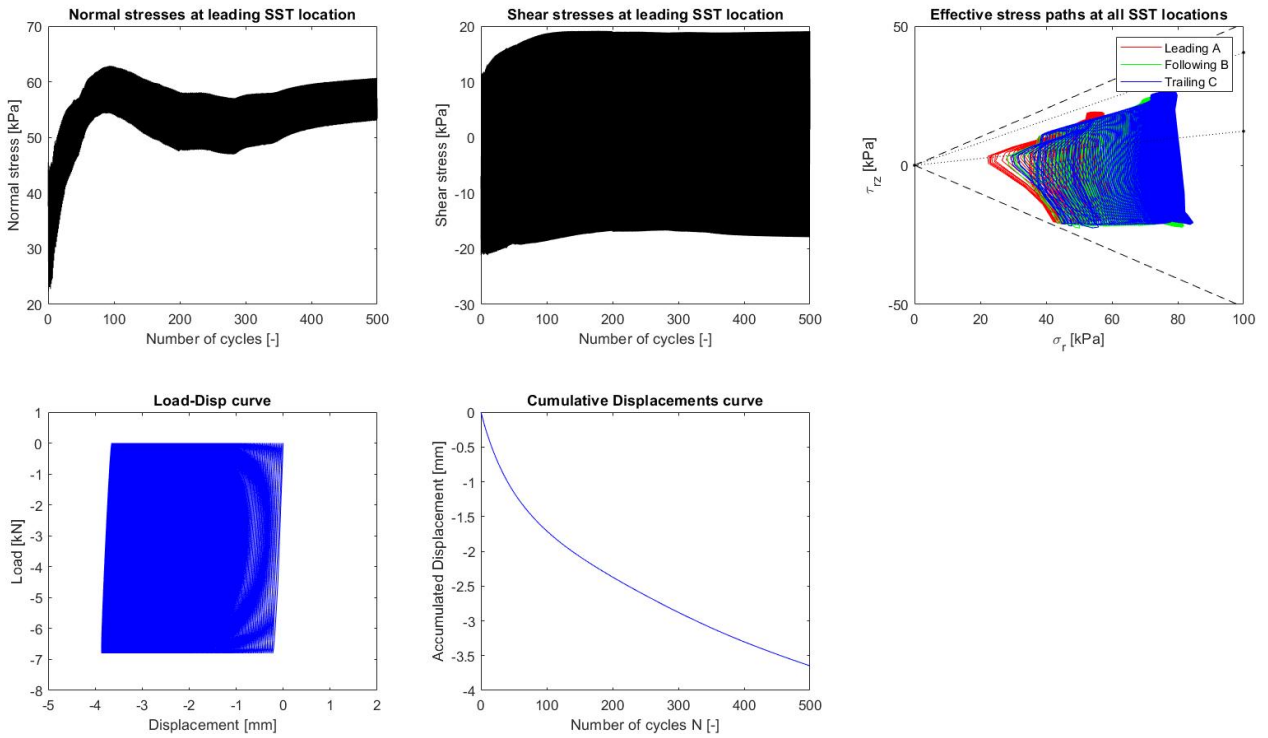


**Figure A-5:** Model results for metastable tests ICP2-OW3.

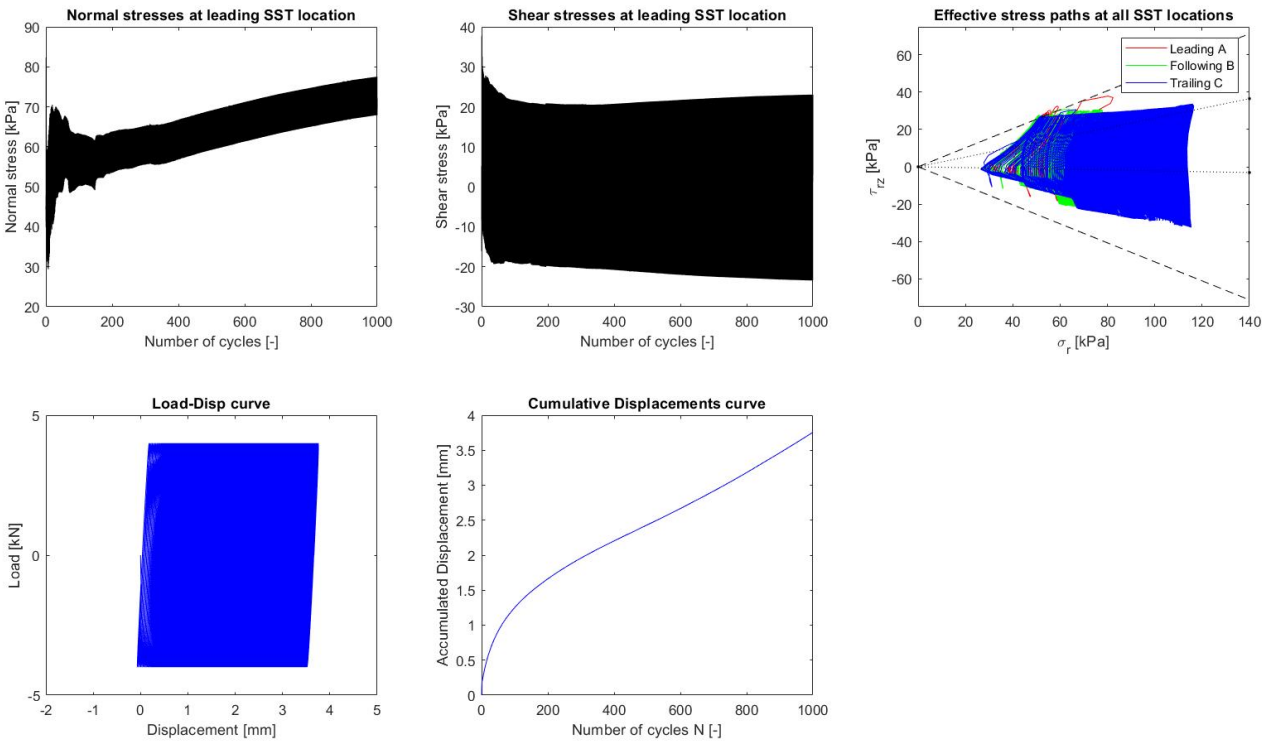


**Figure A-6:** Model results for metastable tests ICP4-TW1.

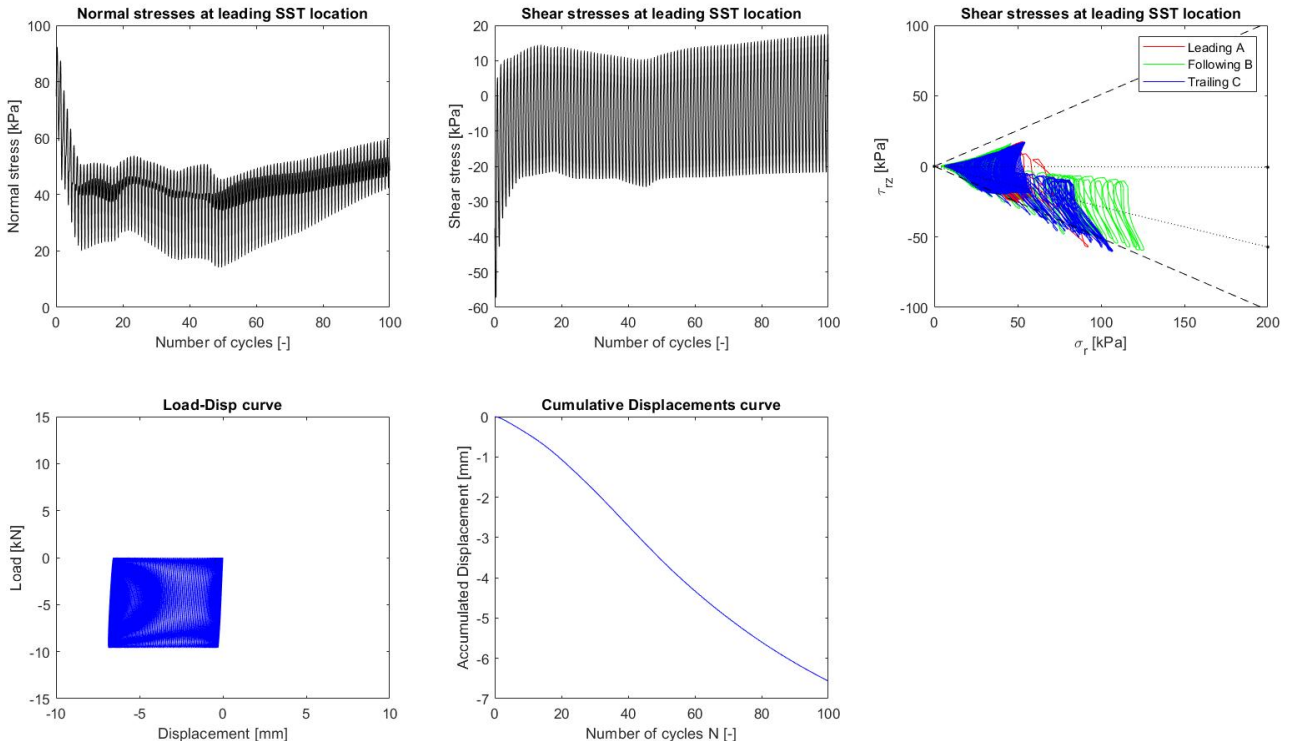


**Figure A-7:** Model results for unstable tests ICP3-OW1.

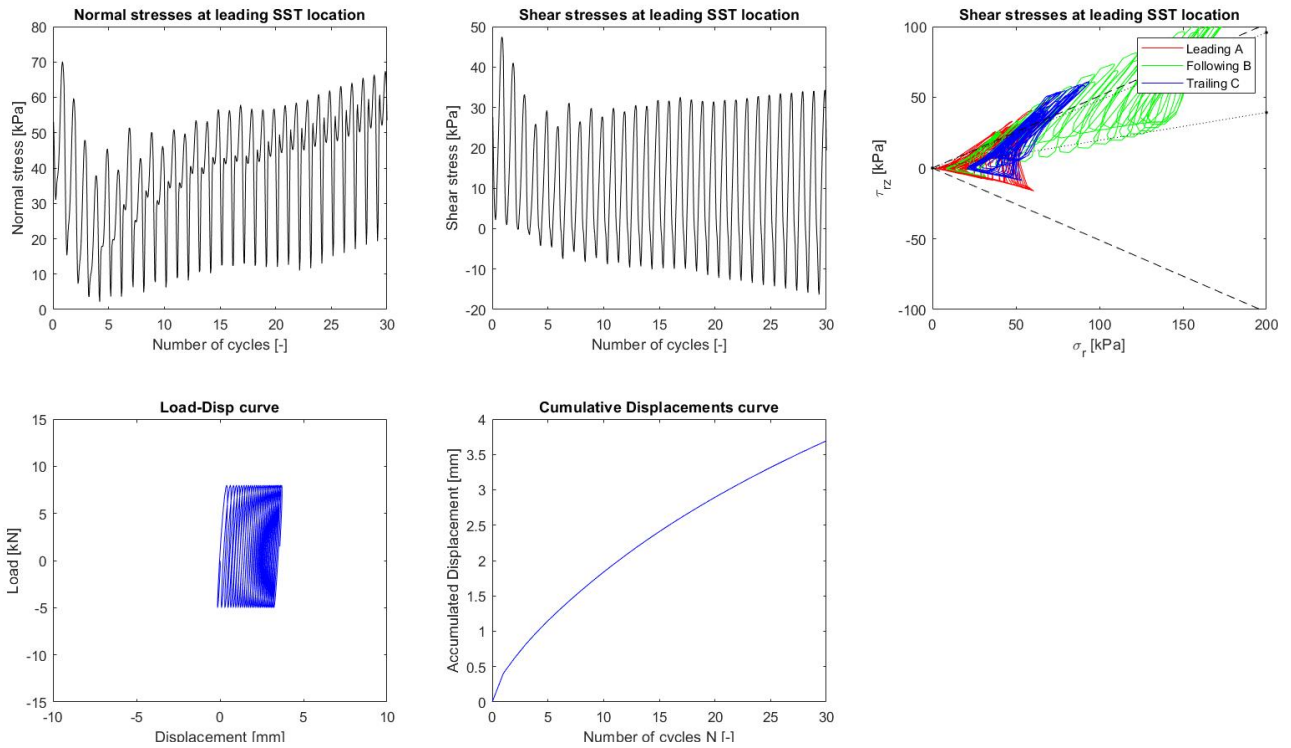


**Figure A-8:** Model results for unstable tests ICP3-TW1.

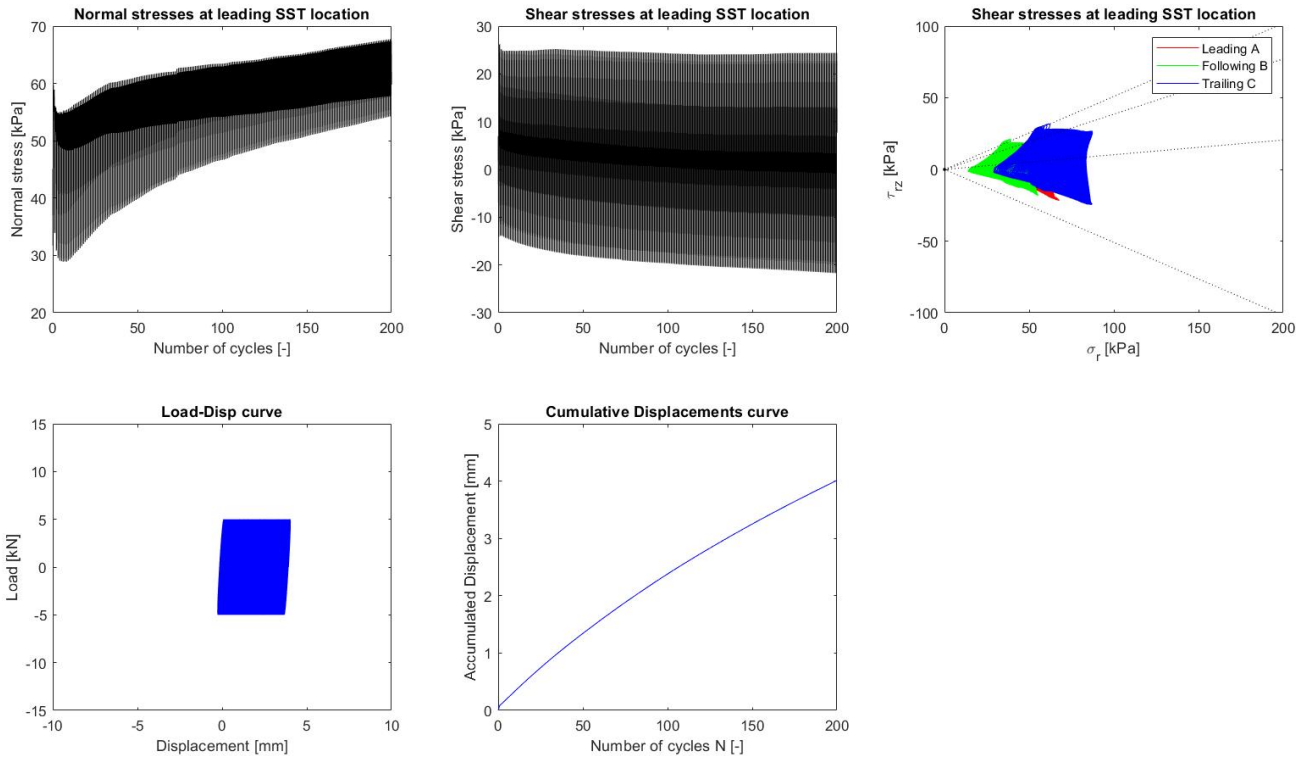


**Figure A-9:** Model results for unstable tests ICP3-TW2.

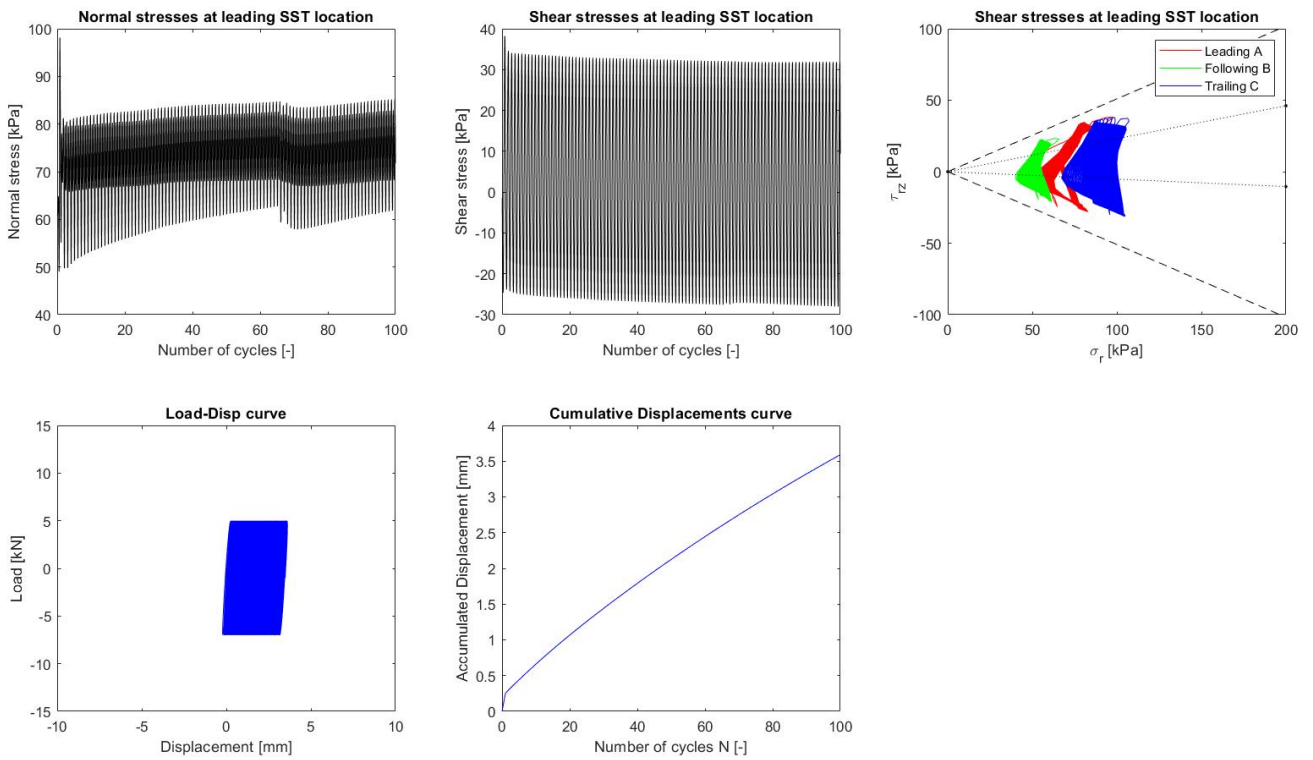


**Figure A-10:** Model results for unstable tests ICP3-TW3.